ZINC OXIDE NANOPARTICLES-BASED REDUCED GRAPHENE OXIDE COMPOSITES FOR PHOTOCATALYTIC AND PHOTOVOLTAIC APPLICATIONS

MAJID AZARANG

FACULTY OF SCIENCE
UNIVERSITY OF MALAYA
KUALA LUMPUR

2017

ZINC OXIDE NANOPARTICLES-BASED REDUCED GRAPHENE OXIDE COMPOSITES FOR PHOTOCATALYTIC AND PHOTOVOLTAIC APPLICATIONS

MAJID AZARANG

THESIS SUBMITTED IN FULFILMENT OF THE REQUIREMENTS FOR THE DEGREE OF DOCTOR OF PHILOSOPHY

FACULTY OF SCIENCE
UNIVERSITY OF MALAYA
KUALA LUMPUR

2017

UNIVERSITY OF MALAYA

ORIGINAL LITERARY WORK DECLARATION

Name of Candidate: **MAJID AZARANG** (I.C/Passport) [redacted]

Registration/Matric No: **SHC110064**

Name of Degree: **DOCTOR OF PHILOSOPHY**

Title of Thesis: ("**Zinc Oxide Nanoparticles Based-Reduced Graphene Oxide Composites for Photocatalytic and Photovoltaic Applications**"):

Field of Study: **EXPERIMENTAL PHYSICS**

I do solemnly and sincerely declare that:

(1) I am the sole author/writer of this Work;
(2) This Work is original;
(3) Any use of any work in which copyright exists was done by way of fair dealing and for permitted purposes and any excerpt or extract from, or reference to or reproduction of any copyright work has been disclosed expressly and sufficiently and the title of the Work and its authorship have been acknowledged in this Work;
(4) I do not have any actual knowledge nor do I ought reasonably to know that the making of this work constitutes an infringement of any copyright work;
(5) I hereby assign all and every rights in the copyright to this Work to the University of Malaya ("UM"), who henceforth shall be owner of the copyright in this Work and that any reproduction or use in any form or by any means whatsoever is prohibited without the written consent of UM having been first had and obtained;
(6) I am fully aware that if in the course of making this Work I have infringed any copyright whether intentionally or otherwise, I may be subject to legal action or any other action as may be determined by UM.

Candidate's Signature Date:

Subscribed and solemnly declared before,

Witness's Signature Date:

Name:

Designation:

ABSTRACT

Zinc oxide nanoparticles and reduced graphen oxide (rGO) composites were synthesized using the sol-gel method in a starch environment. Different concentrations effects of graphene oxide (GO) on the structure and optical properties of ZnO nanoparticles (NPs) were investigated. X-ray diffraction patterns (XRD) and Fourier transform infrared spectroscopy (FTIR) indicated that the GO sheets were reduced and changed to reduced graphene oxide (rGO) during the calcination of the composites at 350 °C. In addition, the XRD patterns of the NPs indicated a hexagonal (wurtzite) structure for all the products. Field emission scanning electron and transmission electron microscope (FESEM and TEM) images showed that the NPs were decorated and dispersed on the rGO sheets very well. In addition, high resolution TEM, HRTEM images revealed that the rGO concentration had an effect on the crystal growth process for the ZnO NPs. Furthermore, these studies showed that the NPs could be grown with a single crystal quality in an optimum rGO concentration. According to the XRD results that were obtained from pure ZnO NPs, the calcinations temperature was decreased by the rGO. Optical studies showed that the optical properties of the ZnO+rGO composite were affected by the rGO concentration. Finally, the obtained ZnONPs+rGO composite was used as photocatalyst to remove methylene blue (MB). Observations showed that the efficiency of the photocatalyst activity of the ZnONPs was significantly increased by GO. In addition, the ZnO+rGO composite was used to generate a photocurrent device. Observations showed that the photocurrent intensity of the composite was dramatically increased by increasing the rGO concentration, with an optimum rGO concentration.

ABSTRAK

Komposit nanopartikel oksida zink dan oksida graphene yang rendah (rGO) telah disintesis menggunakan kaedah sol-gel dalam persekitaran kanji. Kesan kepekatan yang berbeza oksida graphene (GO) pada struktur dan sifat-sifat optik nanopartikel ZnO (NP_S) telah disiasat. Spektroskopi penguraian sinar x (XRD) dan jelmaan Fourier spektroskopi inframerah (FTIR) menunjukkan bahawa helaian GO telah direndahkan dan ditukar kepada graphene oksida yang rendah (rGO) semasa proses mengapur bagi komposit tersebut pada 350 °C. Di samping itu, pola XRD daripada NPs menunjukkan strucktur heksagon (wurtzite) untuk semua produk. Imej-imej dari mikroskopi bidang pelepasan imbasan elektron dan mikroskopi penghantaran elektron (FESEM dan TEM) menunjukkan bahawa NPs telah dibentuk dan tersebar dalam helaian rGO dengan baik. Selain resolusi tinggi TEM, imej HRTEM mendedahkan bahawa kepekatan rGO itu mempunyai kesan ke atas proses pertumbuhan kristal untuk NPs ZnO. Tambahan pula, kajian ini menunjukkan bahawa NPs boleh ditumbuhkan dengan kualiti kristal tunggal dalam rGO kepekatan optimum. Menurut keputusan XRD yang telah diperolehi dari ZnO NPs yang tulen, suhu pengkalsinan telah diturunkan oleh rGO. Kajian optik menunjukkan bahawa sifat-sifat optik komposit ZnO + rGO terjejas oleh kepekatan rGO itu. Akhir sekali, ZnONPs + rGO komposit yang diperolehi telah digunakan sebagai fotokatalis untuk membuang metilena biru (MB). Pemerhatian menunjukkan bahawa kecekapan aktiviti fotokatalis daripada ZnONPs telah meningkat dengan ketara oleh GO. Di samping itu, komposit ZnO + rGO telah digunakan untuk menghasilkan peranti arusfoto. Pemerhatian menunjukkan bahawa keamatan arusfoto bagi komposit tersebut telah meningkat secara mendadak dengan peningkatan kepekatan rGO itu, dengan rGO kepekatan optimum.

ACKNOWLEDGEMENTS

This thesis would not have been possible without the opportunity given to me by the University of Malaya and the inspiration and constant support bestowed to me by the following people:

First of all, I would like to express my gratitude to my supervisor Dr. Ahmad Shuhaimi for their supervision, advice and guidance. I appreciate all their contributions of time, ideas, and funding to make my Ph.D. program productive and exciting. I would also like to thank Department of Physics for providing me support and facilities, University of Malaya for PPP Grant (PG058-2012B), and Ministry of Higher Education of Malaysia for High Impact Research Grant (UM.C/625/1/HIR/MOHE/SC/06).

I want to thank Prof. Wan Jeffrey Basirun and Dr. Mehran Sookhakian for allowing me to use their lab in Department of Chemistry and for their valuable discussions.

I would like to thank my best friend (Dr. Ramin Yousefi), who had suggested and helped me to enroll my study in University of Malaya, and also my good friends Dr. Amir Mordi Golsheikh, Dr. Siamak Pilban, Dr. Ahmad Kamalianfar, for their kind supports.

Finally, I would like to thank all of my family for their support, especially my parents. Words fail me to express my appreciation to my wife, whose love and encouragement allowed me to finish this journey.

TABLE OF CONTENTS

LIST OF FIGURES

LIST OF TABLES

LIST OF SYMBOLS AND ABBREVIATIONS

AFM	:	Atomic force microscopy
CVD	:	Chemical vapor deposition
CPE	:	Constance phase element
CE	:	Counter electrode
CV	:	Cyclic voltammetery
DSSCs	:	Dye-sensitized solar cells
DLE		Deep Level Emission
EDLCs	:	Electrochemical double-layer capacitors
EIS	:	Electrochemical impedance spectroscopy
FESEM	:	Field emission scanning electron microscope
FTIR	:	Fourier transform infrared spectroscopy
GCE	:	Glassy carbon electrode
GO	:	Graphene oxide
HOPG	:	Highly oriented pyrolytic graphite
ITO	:	Indium tin oxide
MB	:	Methylene blue
NBE		Near band edge
NPs	:	Nanoparticles
HOU		Hydroxyuracil
PECVD		plasma-enhanced chemical vapour deposition
PBS	:	Phosphate buffer solution
QDSSCs	:	Quantum dot-sensitized solar cells
rGO	:	Reduced graphene oxide
SCE	:	Saturated calomel electrode

SiC	:	Silicon carbide
SWNTs	:	Single-wall carbon nanotubes
STM	:	Scanning tunneling microscopy
SERS	:	Surface-enhanced Raman scattering
TAA	:	Thioacetamide
TEM	:	Transmission electron microscope
UV	:	Ultraviolet
WE	:	Working electrode
XRD	:	X-ray diffraction

CHAPTER 1: INTRODUCTION

1.1 Background of study

Graphene is a one-atom-thick planar sheet of *sp2*-bonded carbon atoms in form of a honeycomb lattice. Graphene exhibits unique electrical (Usachov et al., 2011), thermal (Shahil & Balandin, 2012), mechanical (Chang, Kim, Lee, & Song, 2010), and optical properties (Zhou, Bao, Tang, Zhong, & Loh, 2009). These unique properties hold great promise for potential applications in many advanced technologies such as nanoelectronics (Freitag, 2008; Zhou et al., 2009), sensors (Cheng, Li, Li, Zhou, & Fang, 2010; Fowler et al., 2009; Robinson, Perkins, Snow, Wei, & Sheehan, 2008), capacitors (Wang et al., 2009; Yu et al., 2011; Zhu et al., 2011) and composites (Chang & Chen, 2011; Ding et al., 2010). So, according to the published papers in web of science, graphene has been extensively studied (Figure 1. 1).

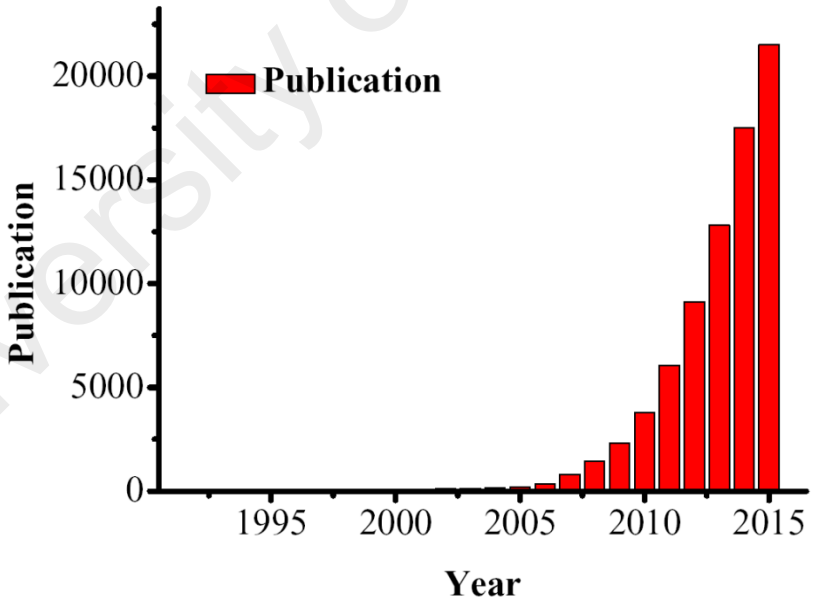

Figure 1.1: Number of publications per year on graphene. The data was extracted on December 29, 2015 through the Institute of Scientific Information (ISI) database using graphene as a keyword that appeared in topic

Recently, carbon allotrope-based semiconductor composites have received great attention in the field of solar cells, which is one of the prospective methods for

converting solar energy to electrical energy (Kongkanand, Dominguez, & Kamat, 2007). Reduced graphene oxide (rGO) is a new class of the carbon family, is tightly packed into a two-dimensional honeycomb lattice, and possesses superior mobility of charge carriers at room temperature (200,000 cm^2 V^{-1} S^{-1}), excellent transparency (~97.7%) and a large surface area (~2600 m^2/g) (Geim, 2009; Gómez-Navarro et al., 2007). Although rGO possesses poor photoelectric properties, the formation of semiconductor nanostructures can largely expand, improve, or alter the properties and applications of the pristine rGO. However, rGO could prevent semiconductor nanostructures from undergoing photo corrosion. A fast charge recombination rate in semiconductor nanostructures and a fast charge transport rate between the semiconductor and the conducting electrode are the major challenges in the photoelectric devices, which could be solved by the incorporation of rGO (Bai & Shen, 2012). Modifying the conducting electrode by rGO leads to the improvement of the conversion efficiency of solar cell devices because the high conductivity of rGO makes it a great material to accept photoinduced charge carriers and to promote the electron transfer rate of the semiconductor nanostructure conduction band to the conducting electrode by trapping the photogenerated electrons. To date, a large number of inorganic semiconductors, such as TiO_2, ZnS, CdS, MnO_2 and PbO, have been successfully attached onto rGO surfaces to form unique hybrid materials for photoelectric devices (Azarang, Shuhaimi, Yousefi, Moradi Golsheikh, & Sookhakian, 2014; Cao et al., 2012; Cheng, Akhtar, Yang, & Stadler, 2013; Ji, Sun, & Han, 2014; Liu et al., 2011; Qu et al., 2014).

ZnO is an important wide-band gap semiconductor that has a direct band gap (3.37 eV) with a high exciton binding energy (~60 meV), which is greater than the thermal energy at room temperature. It is a promising material for ultraviolet Nano-

optoelectronic devices and lasers operating at room temperature (Park, Ma, & Kim, 1997; Yang et al., 2002). ZnO has also drawn great attention as a good electron acceptor and conducting layer (Beek, Wienk, Kemerink, Yang, & Janssen, 2005). The graphene and ZnO in a hybrid material can act in a cooperative way by increasing the migration efficiency of photoinduced electrons and effectively reducing recombination (Li & Cao, 2011; Safa, Sarraf-Mamoory, & Azimirad, 2014). Therefore, various routes have been used to synthesize ZnO@graphene composites such as plasma-enhanced chemical vapour deposition (PECVD) (Zheng et al., 2009), metal–organic chemical vapour deposition (MOCVD) (Lee, Pyun, Yi, Choung, & Park, 2009), solvothermal synthesis (Wu, Shen, Jiang, Wang, & Chen, 2010), a sonication method (Vinodgopal et al., 2010), and a microwave-assisted reaction method (Lv et al., 2011). In addition, several studies have been reported about ZnO@graphene composites that have been used for photovoltaic applications (Huang, Qi, Boey, & Zhang, 2012; Huang et al., 2011; Kamat, 2009). Most of these techniques are complex, expensive, and time consuming. Among these different methods, the sol–gel method is simple, fast, and inexpensive. In addition, it is very important to obtain a narrow size distribution for the final product and to be able to control the morphology of the NPs. These objectives can be achieved by using a suitable polymerization agent in the sol–gel process. Furthermore, zinc oxide is a favourable candidate as a working electrode to substitute for other semiconductors in solar cell devices due to the rapid generation of electron–hole pairs, highly negative reduction potentials of the excited electrons and high electron mobility compared with TiO_2 and ZnS (Zhang, Yu, Jaroniec, & Gong, 2012). Modifying the chemical composition of ZnO by loading organic conductive materials, particularly rGO, could promote the advantages of ZnO in ZnONPs+rGO composites. However, the major challenge is to synthesize ZnO nanostructures with high crystallinity and good dispersity on the surface of rGO nanosheets. ZnO nanoparticles tend to aggregate onto

the surface of rGO during the formation process due to their high surface-to-volume ratio, which results in a higher recombination rate of photoinduced charge carriers. To overcome this challenge, many efforts have been focused on the utilization of surfactants during the synthesis process. In most cases, high molecular weight polymers, such as poly(acrylic acid) (PAA) or polyvinyl pyrrolidone (PVP), were added to avoid ZnO agglomeration on the surface of the rGO (Li et al., 2010). However, these surfactants induce the formation of toxic organic sulphur-containing compounds. To date, various methods have been utilized for the synthesis of ZnONPs+rGO composites, such as one-step and multi-step synthesis. The three main steps are the preparation of ZnO nanostructures, the reduction process of graphene oxide (GO) to reduced graphene oxide (rGO) and the decoration of the semiconductor nanostructure on to the rGO surface with a narrower size distribution and good homogeneity and stability, which can be described as ‘‘one-pot synthesis’’.

Building from these ideas, we report a facile synthesis method of a ZnONPs+rGO composite via a sol-gel approach using zinc nitrate hexahydrate and GO as the starting materials. In our strategy, using a suitable polymer agent, such as starch, can improve the quality of the final product. Therefore, in this study, a simple sol–gel method was used to synthesize ZnO nanoparticles with a narrow size distribution, which were decorated on a reduced graphene oxide (rGO) sheet in a starch environment. Starch was used as a polymerization agent and served as the terminator for the growth of the ZnONPs because it expanded during the calcination process, which prevented the particles from coming together easily. In addition, one of the merits of this method is that the starch and the ZnO nanoparticle products are environmentally friendly. The other merit is that starch reduces GO under mild conditions and simultaneously plays an important role as a capping agent in stabilizing the as-prepared graphene. Most importantly, starch alone can transform graphene oxide into the reduced graphene oxide

(Feng, Feng, & Du, 2013). Then, the photocurrent properties of the as-synthesized ZnONPs+rGO composites under visible light irradiation were investigated to gain insight into the effect of the concentration of rGO on the photocurrent properties of the ZnO nanoparticles (ZnONPs). To the best of our knowledge, there have been no reports on the one-pot sol-gel syntheses of reduced graphene oxide uniformly decorated with zinc oxide nanoparticles in a starch environment, and this is the first demonstration of the functionalization of a ZnONPs+rGO-modified indium tin oxide (ITO) electrode surface with ZnO nanoparticles fabricated by starch, which is a suitable natural polymer agent for solar cells. Here, we report for the first time a fast, one-step, cost-effective, and environmentally friendly synthesis of rGO uniformly decorated with hierarchical ZnONPs using a one-pot sol–gel method in gelatin and starch environment.

1.2 Aim and objectives

As mentioned, superior properties of graphene make it an attractive matrix for composites. It is found that decoration of graphene sheets with nanoparticles not only enhances the performance of graphene and nanoparticles, but also displays additional novel properties resulting from the interaction between nanoparticles and graphene sheets. Developing the method that is fast, low-cost, environmentally friendly and nontoxic for preparing graphene-based composites is very important and challenging. The morphology, size and distribution of nanoparticles on the surface of graphene affect the performance of the composite, which are difficult to control. Compared to metal oxides, few literatures have reported on the synthesis of metal oxide-graphene nanocomposites such as ZnO and even there is no report on the synthesis in environment gelatin and starch.

In order to achieve the mentioned objectives, we designed and carried out the following researches:

1) To design and modify sol-gel techniques for preparing ZnO/rGO composite those are suitable for industrial applications.

2) To identify suitable polymerization agent to control morphology and size of the nanoparticles, this also can be used as industrial techniques to prepare these nanostructures.

3) Optimization of the sol-gel conditions such as reaction temperature, reaction time, of the solution and the amount of gelatin and starch for preparing ZnO nanoparticles.

4) Subsequently utilizing the optimum sol-gel conditions for preparation of ZnO/graphene nanocomposites with different loading amount of graphene.

5) The resultant composites can be evaluated for potential application in energy conversion by photocurrent measurement.

6) The resultant composite can be used for photocatalytic degradation of methylene blue (MB) under ultraviolet (UV) light irradiation.

1.3 Thesis structure

The thesis was written in five chapters. Chapter one presents the history of study, aim and objectives. Chapter Two includes a literature review on synthesis methods and applications. Chapter Three deals with the experimental details of the four main projects:

1. Synthesis and characterization of ZnO NPs/reduced graphene oxide nanocomposite prepared in gelatin medium as highly efficient photo-degradation of MB
2. Effects of graphene oxide concentration on optical properties of ZnO/RGO nanocomposites and their application to photocurrent generation

3. One-pot sol–gel synthesis of reduced graphene oxide uniformly decorated zinc oxide nanoparticles in starch environment for highly efficient photodegradation of Methylene Blue

4. Crystalline quality assessment, photocurrent response and optical properties of reduced graphene oxide uniformly decorated zinc oxide nanoparticles based on graphene oxide concentration

The techniques, which used in this thesis, were explained in the end of this chapter. Chapter Four presents the results and discussion of each project. Chapter Five provides the conclusion of the thesis.

CHAPTER 2: REVIEW OF RELATED LITERATURE

2.1 Introduction

In a past few years, more focus is given to graphene especially for its facile synthesis, novel hybrids materials and applications. Recently, researchers' attention also focused on graphene oxide (GO) and reduce graphene oxide (rGO) nanocomposites, which lead to the development of various applications. Their superb and impressive characteristic makes it a suitable candidate to be hybridized with polymer, metal oxide, and biomaterials. In this brief review, we will run through the accomplishment of effective approach for synthesizing graphene oxide–based material nanocomposite together with their recently developed applications

Graphene oxide (GO) contains a grasp of reactive oxygen functional groups, which make it a strong nominee for use in lots of applications through chemical functionalization. GO is construct from graphite oxide and it has been a favorable passage to produce a large-scale production of graphene (Bai & Shen, 2012; Dreyer, Park, Bielawski, & Ruoff, 2010; Lübke et al., 2015; Safavi, Tohidi, Mahyari, & Shahbaazi, 2012). Graphene, however, has a major drawback which is low dispersibility in water, causing its surface area to decrease and therefore limits its application. This is due to aggregation that causes by the strong van der Waals interactions and π–π stacking of the graphene sheets (Xiao Huang et al., 2011).

Therefore, interest has been concentrate on assimilating GO with other materials by hybridizing it with good water-dispersibility materials (Liu, Liu, & Liu, 2014). By introducing functional groups on the graphene sheets via chemical oxidation, aggregation can be cut down or eradicated which leads to fabrication of graphene oxide (Chauke, Maity, & Chetty, 2015; Muhammad Ekramul Mahmud, Huq, & Yahya, 2016). The dispersibility of GO is only increase in polar solvent due to the hydrophilic

functional groups (Romero Aburto et al., 2015; Zhu, Guo, Fang, & Dong, 2010). In addition, controlled oxidation provides tunability of the electronic and mechanical properties including the possibility of accessing zero-band gap graphene via complete removal of the C-O bonds (Mkhoyan et al., 2009). Various functionalities on the surface of GO make it an ideal platform for chemical modification, which may generate materials with amazing properties.

Aside from the advance properties, the detail chemical structure of GO has been the focus of fascinating debate over the years and yet still no confirmed model is proposed. The only common information is the structural characteristics of GO which is the present of many oxygen functional groups on GO's surface such as epoxy, hydroxyl, and carboxylic acid group (Zhang, Tong, Xia, & Xue, 2014). Due to the deficiency of precise analytical technique for characterizing, the amorphous property of GO, and nonstoichiometric berthollide character of GO, the searching for real model of GO becomes problematic (Dreyer et al., 2010).

Structural model has already been proposed by many researchers such as Hofmann and Holst, Ruess, Scholz-Boehm, and Nakajima-Matsuo model (Dreyer et al., 2010). Based on all of these models, GO is generally constructed by regular lattice consisting of discrete repeated unit. Meanwhile, the atomic and electronic structure of GO is elucidated by Mkhoyan et al. (Mkhoyan et al., 2009) by measuring the structure of C and O K-edges. It is reported that GO sheet showing surface roughness about 0.6 nm and the structure is mainly amorphous due to distortion from sp^3 C-O bonds. The result also reported that a ratio of 1:5 oxygen to carbon atoms is sufficient to transform the measured 40% of the carbon bonds into sp^3 bonds (Mkhoyan et al., 2009). Erickson et al (Erickson et al., 2010) also shared almost the same opinion and adding up a few more outlook of the structure of GO. They found that the graphitic region is up to eight

nm^2 and a hole about five nm is present on the GO sheet. Besides that, the unstrained sp^2 bonds present between carbon which forms a continuous network across the GO sheet and the oxidized region exhibit no order (Erickson et al., 2010).

Synthesizing method of graphene oxide has already been develop in 1859 (Dreyer et al., 2010). At that time, B.C. Brodie performed a reaction between graphite and $KClO_3$ in fuming HNO_3 which resulting a material with an increase in the mass of flake graphite. Later, in year 1898 L. Staudenmaier further the previous method by raising the acidity of the mixture using concentrated H_2SO_4 and adding the chlorate in several aliquots over the course of reaction (Dreyer et al., 2010). After that, Hummer and Offeman improve the method using alternate oxidation. The reaction is involving the oxidation of graphite by using $NaNO_3$, $KMnO_4$ and concentrated H_2SO_4 (Chauke et al., 2015; Dreyer et al., 2010; Erickson et al., 2010; Xiao Huang et al., 2011; J. Liu et al., 2014; Mkhoyan et al., 2009; Muhammad Ekramul Mahmud et al., 2016; Romero Aburto et al., 2015; Safavi et al., 2012; Zhang et al., 2014). This method is mostly used until now with some modification and improvement.

Marcano et al. (Marcano et al., 2010) has developed synthesizing method that improves the efficiency of the oxidation process by excluding the present of $NaNO_3$, raise the usage of $KMnO_4$, and using the ratio 9:1 mixture of H_2SO_4/H_3PO_4. This method was confirmed generate a larger amount of hydrophilic GO material compared to conventional Hummer's method besides it does not release toxic gas and easily controlled temperature (Marcano et al., 2010). Yang, Li, Zhai, Sun, and Yu (Yang, Li, Zhai, Sun, & Yu, 2014) also took some modification on Hummer's method to develop a facile synthesis method of GO by using expanded graphite oxide as a starting material. This method intensely promote to the decrease for acid, extremely time saving, minimum energy consuming, and high efficiency without releasing toxic gas (Yang et

al., 2014). Until now, a continuous rapid research is evolved to develop a simple and environment of friendly methods to prepare GO.

2.2 Synthesis of Graphene Oxide-based Material Nanocomposite

There is a great attention in the preparation method of GO-based material nanocomposite. GO-based material nanocomposite can be synthesized by different methods and approaches which include hydrothermal method (Li, Wang, Li, & He, 2015; Xu, Shen, Li, & Ye, 2014), electrochemical code position (Yiming Li et al., 2015), in situ polymerization (Gui, Liu, Chen, & Liu, 2014; Hualan Wang, Hao, Yang, Lu, & Wang, 2009), microwave-assisted method (She et al., 2015; Xu, Jiang, Ren, & Yang, 2015), vacuum impregnation (Mehrali, Latibari, Mehrali, Metselaar, & Silakhori, 2013), and sol gel technique (He, 2015). In GO-based nanocomposite, GO present either as a functional component or as a substrate for immobilizing the other components (Luo et al., 2015; Song, Qu, Zhao, Ren, & Qu, 2010). Therefore, this section will mainly focus on effective synthesis method that has been practiced by some researchers.

2.2.1 Hydrothermal Method

Hydrothermal is an effective method and frequently favored method to synthesis GO-based nanomaterial, which perform in high temperature and vapor pressure. This method is a very low cost method with facile, environmental friendly, and applicable route to synthesize soluble reduce graphene oxide (rGO) sheets in excessive amount (Lorestani, Shahnavaz, Mn, Alias, & Manan, 2015). This method has been used by (Xu et al., 2014) in one-pot approach to synthesize rGO/$CoWO_4$ and resulting an enhanced electrochemical performance for supercapacitor. Similarly, Dong et al. (Dong et al., 2014) also use the same method to synthesize rGO/TiO_2 nanocomposite as anode material for lithium ion batteries. Hydrothermal or also known as solvothermal method

is usually carried out in Teflon-line autoclave and the temperature used is between 160-180℃ (Sun, Wang, Hao, Han, & Cao, 2015; Xu et al., 2014).

Later, this method has been modified and microwave-assisted hydrothermal method is developed. Gui, Zhao, Tian, and Zhao (Gui, Zhao, Wang, Tian, & Zhao, 2015) was successfully use microwave-assisted hydrothermal method to synthesize graphene/WO_3 by employing GO as a starting material. This method was upheld a greener approach that involve lower temperature and minimize the duration of the reaction compared to conventional hydrothermal method (Gui et al., 2015). This method as well manipulate by Tang, Nguyen, Lee, Kim, and Shim (Tang, Nguyen, Lee, Kim, & Shim, 2015) to prepare rGO/SnO_2 nanocomposite which assisted by ionic liquid that act as a reaction medium in order to enhance the microwave-assisted hydrothermal method. The ionic liquid, 1-butyl-3-methylimidazolium tetra fluoroborate ([bmim]BF4) that use in this reaction is a greener solvent compared to the established organic solvent besides support by the excellent solvent power, lower vapor pressure, non-flammable, good thermal stability, ionic conductivity, and high electrochemical stability (Tang et al., 2015) .

Another option of hydrothermal method is by using continuous hydrothermal flow synthesis (CHFS) reactor. It can manipulate over reaction variables like pressure and temperature and also particle properties which involving mixing a flow of supercritical water with a flow of aqueous metal salt, thus resulting a rapid precipitation and controlled growth of nanoparticle (Saada, Kellici, Heil, Morgan, & Saha, 2015). This method is simply conclude as one of the most economical approaches which can controlled the size of product by enhancing the heating rate as well as saving time (Tang et al., 2015).

2.2.2 Electrochemical Deposition

Electrochemical deposition is a process by which a material is deposited from a solution of ion onto the surface of electrical conductor or electrode. Mostly, this method is employed to fabricate the electrochemical sensor by deposited nanocomposite material onto an electrode (Du et al., 2015; Song et al., 2010). Du et al (Reza, Ali, Srivastava, Agrawal, & Biradar, 2015). (Du et al., 2015) has employed one-step electrodeposition method to synthesis a novel glucose sensor based on rGO-based nanocomposite. In this study, dendritic gold nanostructure is hybridized with rGO functionalize with a globular protein, β-lactoglobulin and was electrodeposited on glassy carbon electrode (GCE) by chronoamperometry technique (Du et al., 2015). Similarly, Wu, Han, Gua, and Cheng (Wu, Han, Guo, & Cheng, 2015) modified Au electrode by direct electrodeposition on rGO and followed by chronoamperometry technique, then electrochemical polymerization takes place to modified the electrode with poly (3-aminophenylboronic acid) film.

Reza et al. (Reza et al., 2015) also use this method to deposit rGO/Cn nanocomposite on indium tin oxide (ITO) glass substrate. The preparation of electrodeposited electrode involving two electrodes that immerse in colloidal rGO/Cn nanocomposite suspension where platinum foil act as a cathode and ITO glass substrate act as an anode (Reza et al., 2015). A part from electrochemical electrode and sensor, this method also can assist the preparation of coated film. This study has been done by Li et al. (Yiming Li et al., 2015) which has synthesize GO/ZnO nanocomposite films on Fluorine doped Tin Oxide (FTO) coated glass and resulting an improve photoelectric conversion properties as a photo absorber.

2.2.3 In Situ Polymerization

In situ polymerization is a prevalent route for the preparation GO-based polymer nanocomposite in a larger scale and avoid the chain destruction (Yan et al., 2014). It has been used to in situ prepare polyaniline, polypyrrole, and polymethyl-methacrylate on GO and rGO layer (Gui et al., 2014; Qi, Sun, Duan, & Guo, 2015; Sun et al., 2015; H. Wang et al., 2009; Yan et al., 2014; Yang et al., 2015). Taking polyaniline as an instance, the distinctive precursor used is aniline, which is then immersed in HCl solution with addition of ammonium persulfate that act as an oxidant (Gui et al., 2014;Sun et al., 2015;Yang et al., 2015).

Similarly, Yan et al. (Yan et al., 2014) prepared polypyrrole/SDBS (sodium dodecyl benzenesulfonate) intercalated reduced graphene oxide (rGO) nanocomposites by using pyrrole as a monomer. In first step, SDBS was intercalated with GO and it is then reduced by hydrazine at 95 ℃ and ammonium persulfate is added to initiate the polymerization of pyrrole monomer. There are intermolecular forces which involving $\pi - \pi$ stacking, hydrogen bond and van der Waals forces that promote the adsorption of pyrrole monomer onto rGO surface. These intermolecular forces between aromatic rings of polypyrrole chains and sp^2-bonded carbon atoms of graphene basal planes also make polypyrrole coat perfectly onto the sheets of graphene (Yan et al., 2014). The benefit of in situ polymerization method lies in the fact that the whole procedure is facile, controllable, and scalable which promotes the intercalation of monomer between the GO and rGO sheets.

2.2.4 Sol-gel Technique

Recently, sol-gel technique has been used to synthesis GO-based material nanocomposite especially in fabrication of self-cleaning film and glass coating. Being the fact that sol–gel derived inorganic composites require low synthesis temperature, the

physical properties of doping component could be retained by controlled the mixture between the guest molecule and the host matrices (Chan Zheng, Zheng, Chen, & Wei, 2015).

The sol-gel approach offers a distinctive means to prepare a three-dimensional network capability for the encapsulation of numerous biomolecules. Peng, Huang, and Zheng, (Li, Yin, Han, & Chang, 2016) has synthesis ferrocene-branched organically modified silica material ormosil/chitosan/GO nanocomposite for glucose sensor. Ormosil is contributed in modification of surface property of the matrices, enhance the film flexibility and prevent leakage when the reagent is attached to the silica (Li et al., 2016). Furthermore, sol–gel derived silica glasses also show an outstanding optical, thermal, transparency in the UV region, and high thresholds for laser damage (Chan Zheng et al., 2015).

2.3 Application of Graphene Oxide-based Material Nanocomposite

2.3.1 Wastewater Treatment

Rapid industrialization has led to an increase discharge wastewater containing heavy metals (Hou Wang et al., 2015) and organic dyes (Xiao Huang et al., 2011). In recent studies, there have been reported for the treatment of wastewater including photocatalysis (Gupta et al., 2015) and adsorption (Boruah et al., 2015). Various GO-based material nanocomposites have been studied that it could give a large contribution in the wastewater treatment especially in heavy metal removal. In fact, GO and rGO are well known as a conqueror in photocatalyst and adsorption application. The large specific surface area and abundant functional groups make GO a strong candidate for adsorption and photocatalyst application in wastewater treatment.

2.3.2 Photocatalysis

There is great interest in the synthesis of graphene oxide nanocomposite for photocatalytic degradation of insecticides, organic dyes, heavy metals and other carcinogenic chemicals. Photocatalyst such as TiO_2, ZnO, ZnS, and WO_3 are commonly employed because of the reusable and self-regenerated properties (Gupta et al., 2015; Li et al., 2016; Hou Wang et al., 2015). However, the practical purpose are narrow due to the rapid recombination of photogenerated electrons and holes within photocatalyst (Hu, Lu, Chen, & Zhang, 2013). Beingthe excellent mechanical strength, low density, high catalytic activity, high surface area and the superior electron-transporting properties, graphene oxide can be exploiting as a competent electron acceptor to boost the photo induce charge transfer for amended photocatalytic activity (Gupta et al., 2015; Hu et al., 2013).

Recently, there are a few researchers assessed the performance for photodegradation of organic dye like Rhodamine B and methylene blue by using graphene oxide-based material nanocomposite. Sun et al. (Sun et al., 2015) evaluated the addition of GO in the semiconductor with low loading of GO (0-0.5 %) to enhance their photocatalytic activity under visible light irradiation. The photocatalytic activity of rGO/Cu_2O ($k = 7.85\times10^{-3}$) was reported exceeding that of pure Cu_2O and Degussa P25 by a factor of 2.9 and 7.9 respectively (Sun et al., 2015). However, further increase of graphene oxide content resulted in a gradual decrease in the photocatalytic activity due to prevention of light from reaching the surface of the Cu_2O by the excessive GO, which would also shield the Cu_2O from absorbing visible light. Besides that, the loading of GO would inhibit the crystallization of Cu_2O that resulted in low photocatalytic activity.

Similar with previous work by Li and Hai (Li & Hai, 2014) rGO/Ag nanocomposite showed superior photocatalytic activity which analyses by Rhodamine B

as model contaminant. However, as the microwave cyclic increase the photodegradation performance becomes weaker, which is attributed to serious oxidation of partially reduced GO. The result supported by Choi et al. (Choi et al., 2015) which also observed a dwindle of the activity of rGO/CuI nanocomposite that perhaps appointed to the slight solubility of catalyst in aqueous solution. Hence, the microwave cyclic time has clearly substantial to the outcome on photodegradation of GO-based nanocomposite for Rhodamine B. The present of graphene oxide, also give benefit to a non-visible light photocatalyst, CuI into a visible light photocatalyst. CuI has a high band gap that is not allowed it to exhibit photocatalytic activity in the visible region. After the hybridization excited electron from stimulated sunlight was injected from rGO nanosheets to the conduction band of CuI, hence it will generate hydroxyl and superoxide radicals that sustained and enhanced by the more stable carbon free radical derived from rGO nanosheets, resulting a visible light activity (Choi et al., 2015).

In an attempt to optimize the parameter of photocatalyst for Rhodamine B degradation, Maruthamani et al. (Maruthamani, Divakar, & Kumaravel, 2015) has synthesized rGO/TiO_2 nanocomposite and studied the influence of rGO content, initial dye concentration, pH, and catalytic dose on decolourization. The result confirms that, as rGO content in the composite was raised, more TiO_2 particles were able to be attached onto the rGO sheet therefore extra charge carriers form exceedingly reactive species and boost the degradation of Rhodamine B. The percentage decolourization of RhB dye increased with the adding of catalyst (up to 1.5 g L^{-1}) due to the upsurge number of active sites that promotes hydroxyl radicals and enhances the dye adsorption on the catalyst surface. Then again, percentage decolouration fall with further increase in catalyst (1.5 to 2 g L^{-1}) that may be ascribe to the agglomeration of the catalyst particles together with increase in the turbidity of the suspension which triggers light

scattering and results in decreased UV light penetration during the reaction (Maruthamani et al., 2015).

Graphene oxide anchored to TiO_2 is one of the most common nanocomposites to be employed as photocatalyst as TiO_2 is a paramount candidate for photocatalytic decontamination. TiO_2 is well known to its high photocatalytic efficiency, chemical stability, antibacterial property, low toxicity, cost effectiveness, abundant and strong oxidizing material (Gao, Li, Sun, & Ng, 2014; Gao, Hu, & Mi, 2014; Raghavan, Thangavel, & Venugopal, 2015). Yet, its high band gap energy (3.2 eV) which contributes to low photo response toward sunlight and recombination effect becomes a drawback to its photocatalytic performance (Gao et al., 2014; Raghavan et al., 2015). Thus, the remarkable electron capture-storage-transport properties of GO could enhance the charge separation efficiency of TiO_2 (Ghavami, Mohammadi, Koohi, & Kassaee, 2014).

Gao et al. (Gao et al., 2014) was modified surface of water filtration polysulfone base membranes with GO/TiO_2 nanocomposite in order to enable photoactivity under both UV and sunlight. Four kinds of TiO_2 nanostructures were prepared including 1D TiO_2 nanotube, 1D TiO_2 nanowire, 3D TiO_2 sphere assembled by nanoparticles (TiO_2 sphere-P) and 3D TiO_2 sphere constructed by nanosheets (TiO_2 sphere-S). The outcomes point out that GO-TiO_2 sphere-S composites expressed superior photodegradation and disinfection activity than TiO_2 sphere-S under solar light irradiation. For this reason, optimizing the nanostructures of photocatalyst and coupled with carbon materials are two favourable attempts to improvise the photocatalyst (Gao et al., 2014).

Some researcher also employed ternary photocatalyst system such as rGO/TiO_2/ZnO (Raghavan et al., 2015), rGO/$CoFe_2O_4$/TiO_2 (Gupta et al., 2015),

rGO/Ag/TiO_2/γ-Fe_2O_3 (Ghavami et al., 2014), rGO/CdS/ZnO (Wang, Yin, & Liu, 2014), and rGO/W/$BiVO_4$ (Wang et al., 2014). The competency of the ternary system was appraised and compared using binary system (coupled with GO) and single photocatalyst material. The degradation competency of ternary system was the excellent photocatalyst as confirmed by (Gao et al., 2014; Ghavami et al., 2014; Raghavan et al., 2015). The surface area of ternary system nanocomposite also enhanced which resulted in an increases absorptivity as reported by (Ghavami et al., 2014; Gupta et al., 2015).

In a photocatalytic system, a reaction takes place at the surface of the catalyst. The generation of an electron–hole pair plays a significant role in a mechanism of a photocatalytic reaction. When a photocatalyst is exposed by a light stronger than its band gap energy, electron–hole pairs diffuse out to the surface of the photocatalyst and participate in a chemical reaction with the electron donor and acceptor (Yousefi et al., 2015). Here, the valance band (VB) electrons (e^-) of photocatalyst are excited to the conduction band (CB), creating holes (h^+) in the VB (Sun et al., 2015). Those free electrons and holes transform the surrounding oxygen or water molecules into hydroxyuracil (HOU) free radicals with super strong oxidation (Yousefi et al., 2015). These free radicals are then used to decomposed organic pollutant into carbon dioxide and water (Gao et al., 2014). A highly efficient visible light photocatalysis should have high quantum efficiency resulting from low recombination of the photogenerated electron-hole pair and a wide light response range because of the narrow band gap (Sun et al., 2015). With the present of excellent electron-mobility of GO anchored to photocatalyst, the charge transport rate could be increased therefore, inhibiting the charge recombination and promoting the photocatalytic activity consequently through quick electron–hole transfer (Li & Hai, 2014). The present of GO also confirmed that it could reduce the band gap that promotes to an excellent photocatalytic activity

(Maruthamani et al., 2015). The list of photocatalyst with the material detection is summarized in (Table 2. 1).

Table 2.1: The list of photocatalyst and material detection in previous study

Photocatalyst	Material detection	Researcher
rGO/Cu_2O	Rhodamine B	(Sun et al., 2015)
rGO/Ag	Rhodamine B	(Li & Hai, 2014)
rGO/CuI	Rhodamine B	(Choi et al., 2015)
rGO/TiO_2	Rhodamine B	(Maruthamani et al., 2015)
rGO/TiO_2	Bisphenol A	(Luo et al., 2015)
rGO/Ag/TiO_2	Methylene blue	(Vasilaki, Georgaki, Vernardou, Vamvakaki, & Katsarakis, 2015)
rGO/Ag/TiO_2/γ-Fe_2O_3	Crystal violet	(Ghavami et al., 2014)
rGO/$CoFe_2O_4$/TiO_2	chlorpyriphos	(Gupta et al., 2015)
GO/TiO_2	*Escherichia coli (E. coli)*	(Gao et al., 2014)
GO/TiO_2	Methylene blue	(Gao et al., 2014)
rGO/TiO_2/ZnO	Methylene blue	(Raghavan et al., 2015)
rGO/CdS/ZnO	Methylene blue	(Wang et al., 2014)
rGO/W/$BiVO_4$	Methylene blue	(Wang et al., 2014)
rGO/Pd/Ni	4-chlorophenol	(Liu, Liu, Shan, & Zhang, 2015)

2.3.3 Adsorption

Many GO-based composite for adsorption of contaminant from wastewater have recently been developed. The magnetic composite like Fe_3O_4 is one of the promising materials for the wastewater remediation. Boruah et al. (Boruah et al., 2015) systematically synthesizes Fe_3O_4 with rGO for methylene blue adsorption with an adsorption capacity of 75.15 mmol/g which is higher than Fe_3O_4. The result supported by Hao, Wang, Gou, and Dong, (Hao, Wang, Gou, & Dong) which fabricate GO/Fe_3O_4as an adsorbent for removal of Chrysoidine Y. GO is exfoliated by strong oxidants, and it consists of a hexagonal network of covalently linked carbon atoms attached with oxygen-containing functional groups, such as epoxy, carboxyl and hydroxyl groups at various sites (Dreyer et al., 2010). Anchoring Fe_3O_4 nanoparticles onto GO might conjoin the relatively high adsorption capacity of graphene oxide and the separation convenience of magnetic materials which it can bind with cationic dyes through the π-π stacking interaction and van der Waals forces. In similar work, Wang et al. evaluated the adsorption performance of ternary magnetic composite consisting of rGO, polypyrrole and Fe_3O_4 nanoparticle for the Cr(VI) removal with adsorption of 293.3 mg/g which is much higher compared to rGO/Fe_3O_4 nanocomposite. Magnetic graphene based adsorbent that assist separation by magnetic field have set out to be used since it is hard to separate small particle size of GO from aqueous solution through conventional centrifugation and filtration method (Hao et al.).

Polypyrrole assist with GO is widely used as Cr(VI) removal as polypyrrole has high chemical stability, ion exchange ability, ease of preparation, and low cost (Chauke et al., 2015; Setshedi, Bhaumik, Onyango, & Maity, 2015). The existence of polypyrrole enhances the adsorption ability due to positively charge nitrogen atoms that easily bind heavy metal (Hou Wang et al., 2015). The hybridization between polypyrrole, GO andα-cyclodextrin make a perfect adsorbent with a strong acid

resistance and superior mechanical properties because it come up with a remarkably larger surface area, the abundant hydroxyl groups and cavities (Chauke et al., 2015).

The Cr(VI) removal is mostly via electrostatic attraction besides some might be involve ion exchange and chemical reduction process (Hou Wang et al., 2015). Previous study done by Setshedi et al. (Setshedi et al., 2015) affirmed that a drop in Cr(VI) removal efficiency is influenced by increasing the solution PH. At lower pH values, greater Cr(VI) removal efficiency could be achieve as the surface of nanocomposite is positively charged due to the detachment of doped Cl^- ions with simultaneous protonation of the nitrogen atom in the presence of sufficient H^+ ions. This result was strongly support by Wang et al. (Hou Wang et al., 2015) and Dong et al. (Dong, Dou, Mohan, Pittman Jr, & Luo, 2015) which stressing on decreasing the adsorption capacity was due to higher PH. Their result also supported by zeta potential values which was decrease with increasing solution pH, receiving from nitrogen groups deprotonated (Dong et al., 2015; Sheshmani, Akhundi Nematzadeh, Shokrollahzadeh, & Ashori, 2015; Hou Wang et al., 2015). However, Liu et al. (Liu et al., 2014) conveyed an opposite opinion, which proved that as the solution pH increase, the adsorption capacity would also increase. This is because the contaminant is in cationic form and lower PH will provide insufficient electrostatic attraction between the cationic contaminant and the nanocomposite (Liu et al., 2014). So, at lower pH, positively charged becomes totally dominant at adsorbent surface that resulting an excellent electrostatic attraction between anionic contaminant and vice versa.

Then again, Sheshmani et al. (Sheshmani et al., 2015) which also use cationic contaminant (Pb(II) ion), yet the adsorption becomes weaker as the pH increase. The interactions take place between the metal ion and the amino groups of the nanocomposite. At low pH, H^+ and Pb^{2+} being competitively adsorbed on the surface of

adsorbent because the amino group of GO/chitosan/FeOOH nanocomposite can be simply protonated to be $-NH_3$ which reduce the adsorption capacity as the increase of electrostatic repulsion between $-NH_3$ and Pb^{2+}. At higher pH, the protonated $-NH_3$ decreases which increase the recovery of $-NH_2$ resulted an increase of the amount of adsorbed Pb^{2+}. However, with further increase in pH, OH^- can be adsorbed onto the surface of $-NH_2$ competing with Pb^{2+}, leading to a reduction in the amount of adsorbed Pb^{2+} (Sheshmani et al., 2015).

Surface area is also one of significant factor in adsorption. Setshedi et al. (Setshedi et al., 2015) affirm that the increased Cr(VI) sorption efficiency of the GO/polypyrrole may be due to the increased surface area. Conversely, Wang et al, (Hou Wang et al., 2015) evaluate that surface area is not a key factor for rGO/polypyrrole/Fe_3O_4 nanocomposite to be a good adsorbent. Therefore, there are three possibility opinion; first, after the hybridization, graphene oxide might help increase the surface area of the adsorbent material and leading to an increase in adsorption capacity (Dong et al., 2015; Setshedi et al., 2015) second, the adsorbent material itself help increase the surface area of graphene oxide as GO poorly dispersed in water and leading to decrease it is surface area (Liu et al., 2014) and lastly, the hybridization of GO with adsorbent material did not influence the surface area at all but the adsorbent still has an excellent adsorption performance (Hou Wang et al., 2015).

GO-based nanocomposite could be a first-class preference as an adsorbent for adsorbing assorted organic molecules owing to its large specific surface and reactivity. What's more, GO capable to form strong π-stacking interaction with a benzene ring due to its greater delocalized π-electron system fabricates it for adsorption of aromatic compounds. For comparison, the material detection, maximum adsorption capacity, and pH of these GO-based nanocomposites are summarized in (Table 2. 2).

Table 2.2: List of adsorbent, material detection, and maximum adsorption capacity from previous study

Adsorbent	Material detection	Maximum adsorption capacity, mg/g	pH	Researcher
GO/Fe_3O_4	Chrysoidine Y	344.83	7	(Hao et al.)
GO/porphyrin/Fe_3O_4	sulfonamides	13.9-sulfanilamide 10.9sulfadimidine 44.2-sulfadimethoxine 28.3-sulfadiazine 10.5-sulfaguanidine 36.3-sulfamethoxazole 26.6-sulfapyridine	4	(Shi & Ye, 2015)
rGO/Fe_3O_4/polypyrrole	Cr(VI)	293.3	3	(Hou Wang et al., 2015)
GO/polypyrrole	Cr(VI)	625	2	(Setshedi et al., 2015)
GO/α-cyclodextrin/polypyrrole	Cr(VI)	606.06-666.67	2	(Chauke et al., 2015)
GO/β-cyclodextrin/poly(acrylic acid)	Methylene blue (MB) & safranine T (ST)	247.99-MB 175.49-ST	9 8	(Liu et al., 2014)
GO/schwertmannite	Sb(V)	158.6	7	(Dong et al., 2015)
GO/chitosan/FeOOH	Pb(II)	111.11	5	(Sheshmani et al., 2015)

2.3.4 Electronic

There are quite many electronic devices have been invented using GO as a starting material such as supercapacitor and lithium ion battery. Supercapacitor and lithium ion battery, is presume to be an excellent nominee for energy storage (Dong et al., 2014; Gui et al., 2014; Ji, Shen, Zhou, & Chen, 2015; She et al., 2015; Xu et al., 2015). Various metal oxides have been employed to develop those devices. However, these metal oxides have certain drawbacks that interferes the chemical and technical process. Therefore, GO and rGO are hybridized with these metal oxides in order to increase the performance of the device.

2.3.5 Supercapacitor

Supercapacitor also known as electrochemical capacitor is an energy storing device which attracted much attention in recent years. Due to its advantages such as high power density, long cycle life and fast charging/discharging rates, supercapacitor also use as an intermediate system between dielectric capacitors and batteries (Wang et al., 2009) as well as conversion of electric devices (Gao et al., 2015). The main challenges of the existence supercapacitor are the lower energy density and poor overall performance (Xu et al., 2014). Therefore, GO-based nanocomposite is introducing as a new supercapacitor with enhanced physicochemical properties, for instance as outstanding electronic conductivity, superior mechanical strength, and greater surface area.

The present of GO and rGO can increase the surface area of the nanocomposite. Work done by Ji, Shen, Zhou, et al. (Ji, Shen, Zhou, et al., 2015) affirms that rGO can inhibit agglomerate and manipulate the ceria's structure. It is commonly admitted that the smaller particles have a better propensity to aggregate and reduce the surface area, specifically in nanoscale. That theory was support by surface morphology studies that

cascading structure of supercapacitor material and GO morphology, which would assist an increase in the specific surface area of the composites and boost electrical conductivity (Gui et al., 2014). The list of various nanocomposites, which is fabricated as supercapacitor material, is shown in (Table 2. 3).

Table 2.3: The specific capacitance and capacitance retention of different types of nanocomposite in supercapacitor application

Nanocomposite	Specific capacitance, F/g	Capacitance retention	Researcher
GO/polyaniline	531.0	-	(Wang et al., 2009)
GO/manganese dioxide	216.0	84.1 % after 1000 cycles	(Chen, Zhu, Wu, Han, & Wang, 2010)
GO/polyaniline	355.2	80.46 % after 1000 cycles	(Gui et al., 2014)
GO/cobalt tungstate	159.9	94.7 % after 1000 cycles	(Xu et al., 2014)
rGO/polypyrrole/sodium dodecyl benzenesulfonate	277.0	50 % after 500 cycles	[(Yan et al., 2014)
rGO/boron nitride	140.0	105.5 % after 1000 cycles	(Gao et al., 2015)
rGO/polyaniline	701.0	92 % after 1000 cycles	(Yan et al., 2014)
rGO/cerium(IV)oxide	265.0	96.2 % after 1000 cycles	(Ji, Shen, Zhou, et al., 2015)
rGO/manganese(II,III)oxide	160.0	91.5 % after 800 cycles	(She et al., 2015)

2.3.6 Lithium ion battery

Lithium ion battery has become one of the most widely used secondary battery for portable electronics, hybrid electric vehicles and renewable energy storage (Peng et al., 2015). Electrochemically active metals and metal oxides such as CuO (Hu & Liu, 2015), $TiOF_2$ (Myung, Kikuchi, Yoon, Yashiro, & Sun, 2015), Fe_3O_4,CoF_2 (Tan et al.,

2015), $CdWO_4$ (Zhang et al., 2014), SnO_2 (Liu et al., 2013), TiO_2 (Rai et al., 2013), and Mn_2O_3 (Hu, Sun, Zhang, & Chen, 2013) have long been considered as anode materials for lithium ion batteries because of their remarkable high theoretical capacities. All of these materials become attractive candidate for electrode material of lithium ion batteries due to their environmental friendly, structural stability and minimum cost production (Wang, Wang, Dong, Zhang, & Jin, 2013; Xu et al., 2015; Chuchun Zheng, He, Zhang, Wang, & Lei, 2015).

Despise of these transcendence properties, there are a few drawbacks that a researcher had to face. Taking TiO_2 as an instance, it bears a low Li-ion diffusivity, theoretic capacity, and low electronic conductivity in reversible Li insertion/extraction process (Qiu et al., 2012; Chuchun Zheng et al., 2015). Similar with TiO_2, one of the most recognized semiconductors, could also have its own downsides. The electrical conductivity CuO in the charge state is relatively poor and it is having a large volumetric change of the electrode that can damage its crystal structure and affect its capacity (Xu et al., 2015). So, GO and rGO is assigned to support the mechanical and electrical properties of the existing material.

Peng et al. (Peng et al., 2015) has hybridized rGO with selenium nanoparticle in order to maximize the capacity and energy density of the lithium-selenium battery cathode. Furthermore, the rGO framework also helps to reduce the selenium loss and prevent the polyselenides from leaving during cycling (Peng et al., 2015). The present of these carbon-based materials also has been confirmed to contribute to the long-term cycle stability, excellent energy capacity, enhanced electrochemical performance, and large reversible capacity compared to the pristine materials (Dong et al., 2014; Wang et al., 2013; Xu et al., 2015; Xu et al., 2015). The list of nanocomposite that already has been fabricated as a supercapacitor material is as shown in (Table 2. 4).

Table 2.4: The nanocomposite that assigned as supercapacitor in previous study

Materials	Initial discharge capacity (mA h g^{-1})	Reversible capacity (mA h g^{-1})-cycles	Current density (mA g^{-1})	Researcher
rGO/selenium	533	265-500	675	(Peng et al., 2015)
rGO/TiO_2	368	136.1-100	1000	(Chuchun Zheng et al., 2015)
rGO/titanium dioxide	295.4	112.3-100	1000	(Dong et al., 2014)
rGO/MnO	1017	988.6-120	100	(Xu et al., 2015)
rGO/TiO_2	310	270-100	100	(Qiu et al., 2012)
GO/CuO	1369.3	590-50	100	(Xu et al., 2015)

2.3.7 Self-cleaning

Recently, self-cleaning technology has begun to grow rapidly since self-cleaning coatings and windows have huge commercialization demand. A self-cleaning materials should have good photocatalytic activity with high durability, optical transparency for coating surface, and superhydrophilicity properties (He, 2015). Superhydrophilicity is a state of material having strong affinity to water greater to non-polar air which is a very important properties need as a self-cleaning coating (Drelich, Chibowski, Meng, & Terpilowski, 2011).

Thakur and Karak, (Thakur & Karak, 2015), has fabricate rGO/TiO_2 nanocomposite which shows an excellent self-cleaning properties. The report revealed that the self-cleaning properties increase with increasing amount of TiO_2. Whereas, the increasing amount of rGO will assists in effective healing properties (Thakur & Karak, 2015). Substantially, He shared (He, 2015) the same viewpoint which the photocatalytic

activity improved with increase of rGO/ZnO ratio which is due to the 3 factor; first, development of their charge separation due to electrons infusion from the conduction band of ZnO to graphene; secondly, the reduce of average particle size; and third, the increase of superhydrophilicity.

Meanwhile, Yun et al (Yun et al., 2012) reported that prepared GO/TiO_2 nanocomposite had excellent self-cleaning properties toward methylene blue stained films. Similar with work done by Thakur and Karak, the increasing content of GO led to improvement in film transmittance and higher efficiency in methylene blue adsorptivity. With superhydrophilicity of GO, it can be a suitable candidate for both an adsorbent and a binder (Yun et al., 2012).

2.3.8 Sensor

Sensors based on graphene oxide-based nanocomposite material are getting an endless attention due to their ultrafast response (Zhang et al., 2014), great sensitivity (Lorestani et al., 2015), esteem long-term stability (Su & Peng, 2015), super conductivity (Yang et al., 2015), reproducible (Ikhsan et al., 2015) and facile fabrication. Recently, nanocarbon material has appeared to be a momentous outlook in the topic of humidity and gas sensor. Its sensitivity towards water molecule is due to the numerous oxygen functional groups that decorated on basal plane and the edge of graphene oxide, such as carboxylic acid, hydroxyl, and epoxy group which can expand the hydrophilicity (Zhang et al., 2014). Nanostructure material normally show certain apparent benefit for sensor purpose for instance tremendous adsorption capacity, large specific surface area, great mechanical stiffness, extraordinary high carrier mobility and better stability (Yao & Xue, 2015; Zhang et al., 2014), So far, many researchers have employed GO-based material to detect humidity (Yao & Xue, 2015; Zhang et al., 2014),

hydrogen peroxide (Lorestani et al., 2015), trimethylamine (Gui et al., 2015), ammonia (Tiwari, Atri, & Sharma, 2015), and nitrogen dioxide (Su & Peng, 2015).

To date, many biosensors based on GO-based nanomaterial have catch researchers' attention. One of it is glucose biosensor which successfully synthesized by one step electrodeposition (Du et al., 2015). In this study, rGO/β-lactoglobulin acts as stabilizer and an excellent template for the growth of dendritic gold nanostructures (Au NPs). Au NPs draws a particular consideration in electrochemical field since it has good chemical stability, large surface area, exceptionally biocompatible, enhance the electrode conductivity and capable to assist electron transfer between electrode and biomolecule (Peng et al., 2015; Yola, Eren, & Atar, 2015). In the study done by Peng et al. (Peng et al., 2015), Au NPs were employed to immobilize the probe DNA via Au-S bond to detect multidrug resistance gene in cancer treatment. The hybridization of GO with toluidine blue and Au NPs, GO was used to enlarge the loading capacity of the toluidine blue and preclude the leakage of the toluidine blue from the electrode surface (Peng et al., 2015). Yola et al. (Yola et al., 2015), also employed GO anchored to Au involving 2-aminoethanethiol for detection of tyrosine in milk which fabricate a superior sensor with low detection limit (Yola et al., 2015). The list of sensor, material detection, and detection limit is summarizing in (Table 2. 5).

Table 2.5: The type, material detection and detection limit of previous synthesized sensor

Type of sensor	Sensor	Material detection	Detection limit	Researcher
Gas sensor	GO/poly (diallyldimethylammonium chloride)	Humidity	-	(Zhang et al., 2014)
	rGO/Ag	Hydrogen peroxide	0.9×10^{-6}M	(Lorestani et al., 2015)
	GO/nanodiamond	Humidity	-	(Yao & Xue, 2015)
	GO/WO_3	triethylamine	-	(Gui et al., 2015)
	rGO/polypyrrole	ammonia	-	(Tiwari et al., 2015)
	rGO/WO_3	NO_2	-	(Su & Peng, 2015)
Biosensor	rGO/β-lactoglobulin/Au	Glucose	2.29×10^{-5} M	(Du et al., 2015)
	GO/Au/toluidine blue	Multidrug resistance	2.95×10^{-12}M	(Peng et al., 2015)
	rGO/ZnS/	Ascorbic acid (AA), dopamine (DA) and uric acid (UA)	3×10^{-5} M-AA 5×10^{-7} M-DA 4×10^{-7} M-UA	(Yang, 2015)
	GO/Pt/CeO_2/1-naphthol	Influenza	4.3×10^{-13}g mL^{-1}	(Yang, Zhuo, Yuan, & Chai, 2015)
	GO/multi-walled carbon nanotube	Sunset Yellow (SY) and Tartrazine (TT)	2.5×10^{-8}M-SY 1×10^{-8} M-TT	(Qiu et al., 2016)
	rGO/Fe_3O_4	Acetylcholine	3.9×10^{-8} M	(Qian et al., 2014)
	rGO/CeO_2	NO	9.6×10^{-9} M	(Hu, Xie, Bao, Yu, & Li, 2015)
	rGO/chitosan/tyrosinase	Bisphenol A	7.4×10^{-10} M	(Reza et al., 2015)
	rGO/SnO_2	Dopamine	1×10^{-6} M	(Nurzulaikha et al., 2015)

	GO/Au/2-aminoethanethiol	Tyrosine in milk	1.5×10^{-10} M	(Yola et al., 2015)
Environmental sensor	rGO/poly (3-aminophenylboronic acid)	Fluorine	9×10^{-11} M	(Wu et al., 2015)
	rGO/polyaniline	Mercury ion	3.5×10^{-11} M	(Yang et al., 2015)
	GO/Ag	Nitrite ion	2.1×10^{-6} M and 3.7×10^{-5} M	(Ikhsan et al., 2015)
	GO/Ag	Dye	1×10^{-6} M	(Ding, Xie, Liu, Wang, & Xu, 2015)

2.3.9 Catalyst

Various catalyst based on GO nanocomposite have been studied recently. Despite the fact that there has been a significant exertion committed to the utilization of different metals as suitable catalyst, there is still a need in finding suitable backings for the catalyst framework and this zone needs to be investigated more.

One of the latest researches is done by Zahed and Monfared (Zahed & Hosseini-Monfared, 2015) which synthesis GO/Ag nanocomposite as a catalyst for aerobic oxidation of benzyl alcohol. Silver is well known as a catalyst for many oxidation reactions. The Ag particles that consist of very small particle can contribute to greater specific surface area, but it is also might lead to agglomeration from corrosive surface energy. Therefore, the present of GO can support and separate the nanoparticle, avoiding it from agglomerate and make it recyclable (Zahed & Hosseini-Monfared, 2015). This catalyst also is confirmed to be reuse for several times. In different work, GO/Ag nanocomposite is employed as a catalyst for reduction of 4-nitrophenol (Yizhao Li et al., 2015). This nanocomposite was reported to be highly reactive and very stable catalyst. The high activity of GO/Ag nanocomposite may be credited to present of GO

that also lead to exceptionally productive contact between 4-nitrophenol and Ag nanoparticles on GO surface.

In previous work done by Song et al. (Song et al., 2010), GO-COOH has inherent peroxidase-like action and its catalysis is emphatically subject to pH, temperature, and H_2O_2 concentration, like horseradish peroxidase. Peroxidase has extraordinary potential for handy application and can be utilized as a diagnostic kit for hydrogen peroxide and glucose (Song et al., 2010). Horseradish peroxidase has been generally used to manufacture sensors for product detection of the glucose oxidase. GO-COOH is low cost, simple to acquire, steadier to biodegradation, and less defenseless against denaturation compared to horseradish peroxidase. Hence, these focal points show that GO-COOH can be valuable in ecological observing and medicinal diagnostic. A few of recent fabricated catalyst shave been listed in (Table 2. 6).

Table 2.6: The previously synthesised catalyst and its catalytic activity

Catalyst	Catalytic activity	Researcher
rGO/Cu	Reduction of 4-nitrophenol	(Yeh, Wu, & Chen, 2014)
GO/Ag	Reduction of 4-nitrophenol	(Yizhao Li et al., 2015)
GO/magnetite/ Ag	Reduction of 4-nitrophenol	(Ji, Shen, Yue, et al., 2015)
GO-COOH	Reduction of H_2O_2	(Song et al., 2010)
GO/Ag	Aerobic oxidation of benzyl alcohol	(Ding et al., 2015)

2.3.10 Biomedical

Graphene oxide-based nanocomposite has expose fascinating purposes in the biomedical field. GO is extensively use in biomedical application due to its two-

dimensional plane and one-atom thickness give it with superior specific surface area for immobilization of numerous substance including a wide range of metals, biomolecules, fluorescent molecules and drugs (Yang et al., 2009).

Yang et al. (Yang et al., 2009) has reported a hybrid of GO with superparamagnetic Fe_3O_4 for controlled targeted drug carries. The GO/Fe_3O_4/doxorubicin nanocomposite exhibits a hydrophilic surface and its superparamagnetic properties make it easily congregate under acidic environment and move in magnetic field besides it can simply be redispersed to make a stable suspension under basic condition (Yang et al., 2009). Similarly, Zhang, Xia, Zhao, Liu and Zhang (Zhang, Xia, Zhao, Liu, & Zhang, 2010) also has fabricated GO as a novel nanocarrier for the loading and targeted deliveries of anticancer drug by functionalize it with sulfonic acid and binding with folic acid. Compared to nanocomposite synthesized by Yang et al. (Yang et al., 2009), this nanocomposite tends to load two anticancer drugs, which are doxorubicin and camptothecin simultaneously. Since they have an efficient loading property of multiple anticancer drugs, the therapeutic efficacy could be enhance which lead to wide potential clinical practice (Zhang et al., 2010).

Titanium and its alloy is well known as electrochemical devices due to large surface area, excellent mechanical properties, bioactivity and corrosion resistance (Yan et al., 2015). With that, Yan et al. (Yan et al., 2015), has employed GO cross-linked gelatin as reinforcement fillers in hydroxyapatite coating by electrochemical deposition process on TiO_2 nanotube arrays. The enlarged surface area of nanotubular surface of TiO_2 offers a huge active reaction sites for chemical reaction and develops the growth, adhesion, and differentiation of the cell (Yan et al., 2015). Meanwhile, Wang et al. (Wang et al., 2010) has exploring the sensing property of GO/aptamer-carboxyfluorescein in vitro and in situ molecular probing in living cell. The effectual release to molecular targets in living

cells recommend that GO could be a decent vehicle to transport gene into cells, shielding the loading genes from the enzymatic cleavage and empowering in situ molecular probing in living cells (Wang et al., 2010).

2.4 Summary

In summary, recent studies on graphene oxide-based nanocomposites going somewhat rapidly. Owing to their spectacular and unique properties, researchers have been competing to develop novel nanocomposite with various synthesis methods. The synthesis method plays avital role in order to produce a larger scale production and control the quality of nanocomposite. At the same time, the methods should be efficient, affordable, and safer for the environment. The present of GO also gives a great contribution toward enhancing the performance of other material. Therefore, there a lot more work need to be done in order to manipulate the two-dimensional GO sheets for future advanced technology.

CHAPTER 3: DESIGN, METHODS AND PROCEDURE

3.1 Chemical reagents

All chemicals, which were purchased from Merck Co., were of analytical purity and were used without further purification. Milli Q-Plus water (resistance, 18.3 MΩ) was utilized for all experimental procedures. All experiments were carried out at atmospheric air pressure.

3.2 Materials

Graphite flakes (code no. 3061) were purchased from Ashbury Inc. (NJ, USA). Sulphuric acid (H_2SO_4, 98%), potassium permanganate ($KMnO_4$, 99.9%), hydrogen peroxide (H_2O_2, 30%), hydrochloric acid (HCl, 37%), and sodium hydroxide (NaOH, 99.99%) were purchased from Merck. Zinc nitrate hexahydrate ($Zn(NO_3)_2.6H_2O$) was purchased from Systerm, Malaysia. Gelatin and starch was obtained from Sigma-Aldrich (St. Louis, MO). Distilled water was used throughout the sample preparation.

3.3 Synthesis

3.3.1 Preparation of exfoliated graphite GO

Exfoliated graphite oxide was prepared based on a modified Hummer's method (Hummers Jr & Offeman, 1958). Typically, graphite flakes were oxidized by mixing H_2SO_4 and H_3PO_4 at a ratio of 4:1 (v/v) at room temperature. The graphite and potassium permanganate were added slowly to the above mixture solution. Then, the mixtures were stirred for three days to complete the oxidation of the graphite. After that, hydrogen peroxide was added to stop the reaction. The mixture was sonicated and washed with HCl and water several times until the pH became neutral. During the washing and sonication process, the graphite oxide was exfoliated to graphene oxide nanosheets (GONs). The product was dried in a vacuum oven overnight at 60°C. The resulting product was a loose brown powder with a hydrophilic nature.

3.3.2 Preparation of ZnONPs+rGO composite by gelatin

First, GO was synthesized using Hummers' method (Hummers Jr & Offeman, 1958). Then, the ZnO NPs to be decorated on the sheets with different GO concentrations were synthesized using a simple sol–gel method in a gelatin medium, which was used as a polymerization agent. In this synthesis, analytical grade zinc nitrate hexahydrate $Zn(NO_3)_2.6H_2O$, gelatin (type B from bovine skin), and distilled water were used as the starting materials. All the materials used were purchased from Sigma–Aldrich. First, a gelatin solution was prepared by adding gelatin (1.25 g) to 50 ml of distilled water at 60 °C. The zinc nitrate (4.46 g) was dissolved separately in a minimal amount of distilled water at room temperature, and solutions of GO with 0.9, 1.7, and 3.3 wt%/v concentration were added to this zinc nitrate solution. Finally, the obtained solution was added to the gelatin solution. After this, the compound solutions were stirred and heated at 80 °C until a gel with a dark brown color was obtained. The gel was calcined at 300 °C for 1 h, at a heating rate of 2 °C/min. Finally, a post-annealing process was performed for 2 h at 400 °C under an Ar gas atmosphere to remove the gelatin material and obtain the final nanocomposite. The process is shown in Figure 3. 1 and Figure 3. 2.

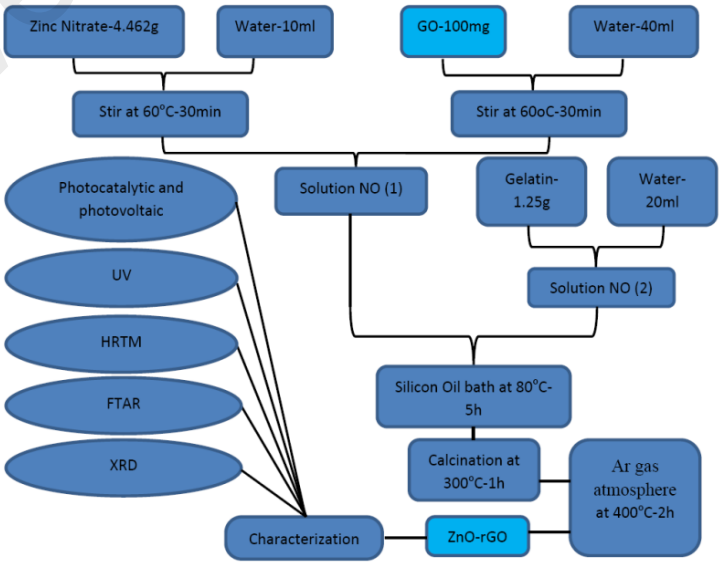

Figure 3.1: Synthesis process of ZnO–NPs by gelatin

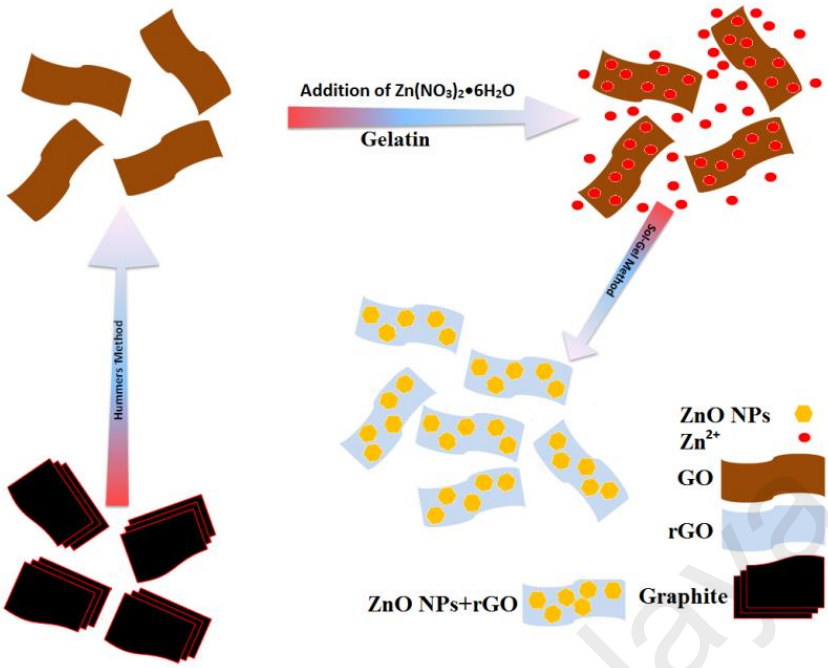

Figure 3.2: Schematic illustration of the formation mechanism of a ZnONPs/rGO composite via a sol-gel method with gelatin

3.3.3 Preparation of ZnONPs+rGO composite by starch

ZnONPs were synthesized and decorated onto the resulting GO sheets via a sol–gel method in a starch environment. In this synthesis, analytical grade zinc nitrate hexahydrate (Zn $(NO_3)_2.6H_2O$), starch and distilled water were used as the starting materials. First, a starch solution was prepared by adding starch at 22 wt.%/v to 150 ml of distilled water at 60°C. The zinc nitrate (4.46 g) was dissolved separately in 50 ml of distilled water at room temperature, and a solution of GO with a 1.7 wt.%/v concentration was added to this zinc nitrate solution. Finally, the resulting solution was added to the starch solution. After this, the compound solutions were stirred and heated at 80°C until a gel with a dark-brown colour was obtained (~12 h). The gel was calcined at 350°C for 1 h at a heating rate of 2°C/min to obtain the composite. Eventually, the product, ZnONPs+rGO, was obtained using centrifugation, washed with distilled water and ethanol several times to remove the excess polymer and ions, and then dried at

60°C for 24 h in a vacuum oven. The as-synthesized ZnONPs+rGO composites with 0, 0.9, 1.7 and 3.3 wt.%/v GO were called ZnONPs, ZnONPs+rGO1, ZnONPs+rGO2 and ZnONPs+rGO3, respectively. The process is shown in Figure 3. 3

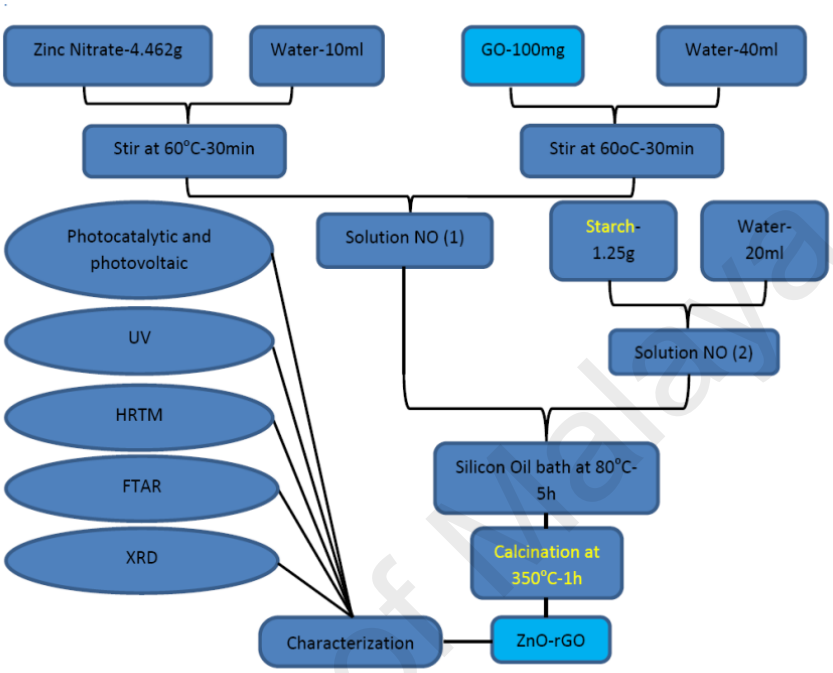

Figure 3.3: Synthesis process of ZnO–NPs by starch

Furthermore, to optimize the experimental conditions for the preparation of pure ZnONPs and ZnONPs+rGO, numerous samples with different parameters were synthesized, as listed in Table 3. 1. The experimental mechanisms discussed above are summarized in Figure 3. 4.

Table 3.1: Experimental conditions different for the preparation of ZnONPs and ZnONPs+rGO

Sample code	Temperature (^{o}C)	Time (h)	Rate (C/min)	GO (wt.%/v)	Starch (wt.%/v)
A	300	2	2	1.7	22
B	350	2	2	1.7	30
C	350	2	2	1.7	12
D	350	2	2	1.7	22
E	350	1	2	1.7	22
F	350	3	2	1.7	22
G	350	2	1	1.7	22
H	350	2	3	1.7	22
I	350	1	2	3.3	22
J	350	1	2	0.9	22
K	350	1	2	0	22
L	400	2	2	1.7	22
M	350	1	2	0	0
N	400	1	2	0	22
P	500	1	2	0	22

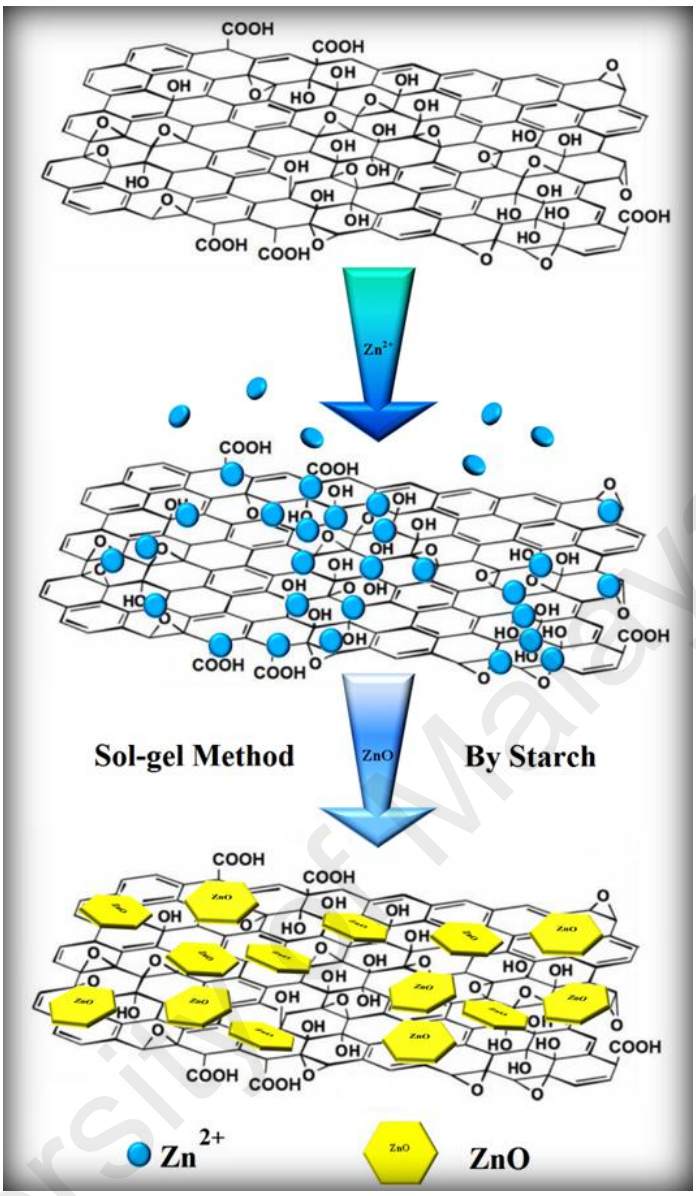

Figure 3.4 : Schematic illustration of the formation mechanism of a ZnONPs+rGO composite via a sol-gel method with starch

3.4 Applications

3.4.1 Preparation of photocatalytic degradation samples

The photocatalytic performance of the as-prepared samples was evaluated using the photocatalytic degradation of Methylene Blue (MB) under UV light irradiation. Here, 10 mg of the resulting material was dispersed in 30 ml of the MB aqueous solution (10 mg/l). The mixed suspension was magnetically stirred for 1 h in the dark to

reach an adsorption–desorption equilibrium. Under ambient conditions and stirring, the mixed suspension was exposed to UV irradiation produced by a 500-W High-pressure Hg lamp with the main wave crest at 365 nm for different times (1 to 6 h). At certain time intervals, 2.5 ml of the mixed suspension was extracted and centrifuged to remove the photocatalyst. The degradation process was monitored by measuring the absorption of MB in the filtrate at 664 nm using a UV–vis absorption spectrometer.

3.4.2 Device fabrication and photocurrent measurements

All working electrodes were prepared using the doctor blade method (Barpuzary & Qureshi, 2013; Kim et al., 2009; Ohsaki et al., 2005; Wengeler, Schmitt, Peters, Scharfer, & Schabel, 2013). For the preparation of the working electrodes, all samples were dispersed in a chitosan solution (0.5 wt.%/v) to form a 10 mg/ml solution and then ultrasonicated for 5 min. Next, 0.1 ml of colloidal solution was dropped onto a cleaned ITO surface (1×1 cm^2) and then allowed to dry overnight at room temperature. The solar cell devices were assembled using working electrodes that consist of ZnONPs, ZnONPs+rGO1, ZnONPs+rGO2 and ZnONPs+rGO3 photoanode-modified ITO films and Pt foil as a counter electrode, which were filled with the electrolyte in a 50-μm-thick spacer. The I^-/I_3^- liquid electrolyte consists of 0.5 M KI, 0.05 M I_2, 0.6 M tetrabutylammonium iodide and 0.5 M 4-tertbutylpyridine in acetonitrile. A PLS-SXE150 halogen lamp (Beijing Perfectlight Technology Corp., China) was utilized as an illumination source. The light intensity at the photoanodes was 20 mW/cm^2, the area illuminated by the photoanodes was 0.5 cm^2, and the distance between the working electrode and the lamp was approximately 40 cm. The photocurrent was recorded continuously during the on and off period of the lamp. The transient photocurrent measurements of the devices were performed using a potentiostat/galvanostat (Autolab PGSTAT30) from Ecochemie (Netherlands). Finally, for a better understanding of the

actual size, configuration and structure of the device, the fabrication processes device is shown in Figure 3. 5.

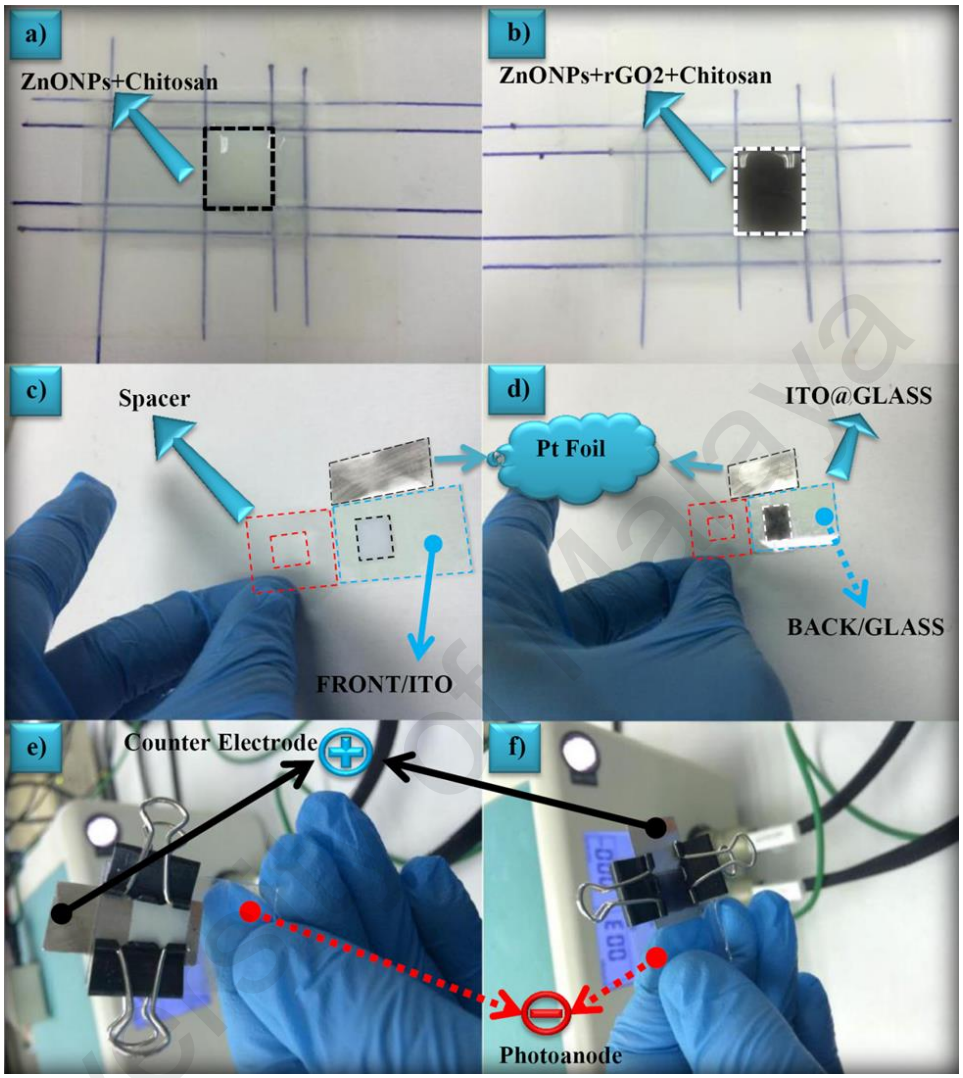

Figure 3.5: Actual size, configuration and structure of the fabricate solar cell device of ZnONPs and ZnONPs+rGO2 composites. (a, b) colloidal solution was dropped onto a cleaned ITO surface (1×1 cm^2) and then allowed to dry overnight at room temperature, (c, d) Pt foil, Spacer and ITO@GLASS for both samples, (e, f) solar cell device of ZnONPs and ZnONPs+rGO2 composites respectively

3.5 Characterization techniques and instrumentation

In this section, the characterization methods and instruments that have been used in this project are described. The prepared nanostructures were characterized by powder X-ray diffraction (XRD), ultraviolet–visible (UV–vis) spectroscopy, Fourier-transform

infrared Spectroscopy (FTIR), Field emission scanning electron microscopy, transmission electron microscopy (TEM) and high resolution transmission electron microscope (HRTEM).

3.5.1 X-ray diffraction (XRD) analysis

X-ray diffraction is one of the primary techniques used by mineralogists and solid state chemists to examine the physical-chemical make-up of unknown materials. Two important characteristics can be obtained using the XRD pattern produced by this technique. These include a fingerprint characterization of the crystallite materials and a determination of their structure. The fundamental of XRD analysis are based on Bragg's law ($n\lambda = 2d_{hkl}\sin\theta$). According to this low, scattered waves originating from each atom which are in the different planes, will be in phase with each other. Figure 3. 6 shows the requirements for this condition.

In our study, the phase evolutions and structure of the ZnO nanoparticles were studied by Siemens D5000 XRD Diffractometer. The diffraction experiments were applied at a fixed wavelength (λ, CuKα = 1.54056 Å) and different angles (2θ). The ZnO (hexagonal) lattice parameters, e.g., the values of d, the distances between adjacent crystal planes (hkl), were calculated from the Bragg equation, λ=2d sinθ; the lattice constants a, b and c, inter planar angles, the angles φ between the planes ($h_1k_1l_1$) of spacing d_1 and the plane ($h_2k_2l_2$) of spacing d_2 and the primary cell volumes, V, were calculated from the Lattice Geometry equation (Cullity, 1956).

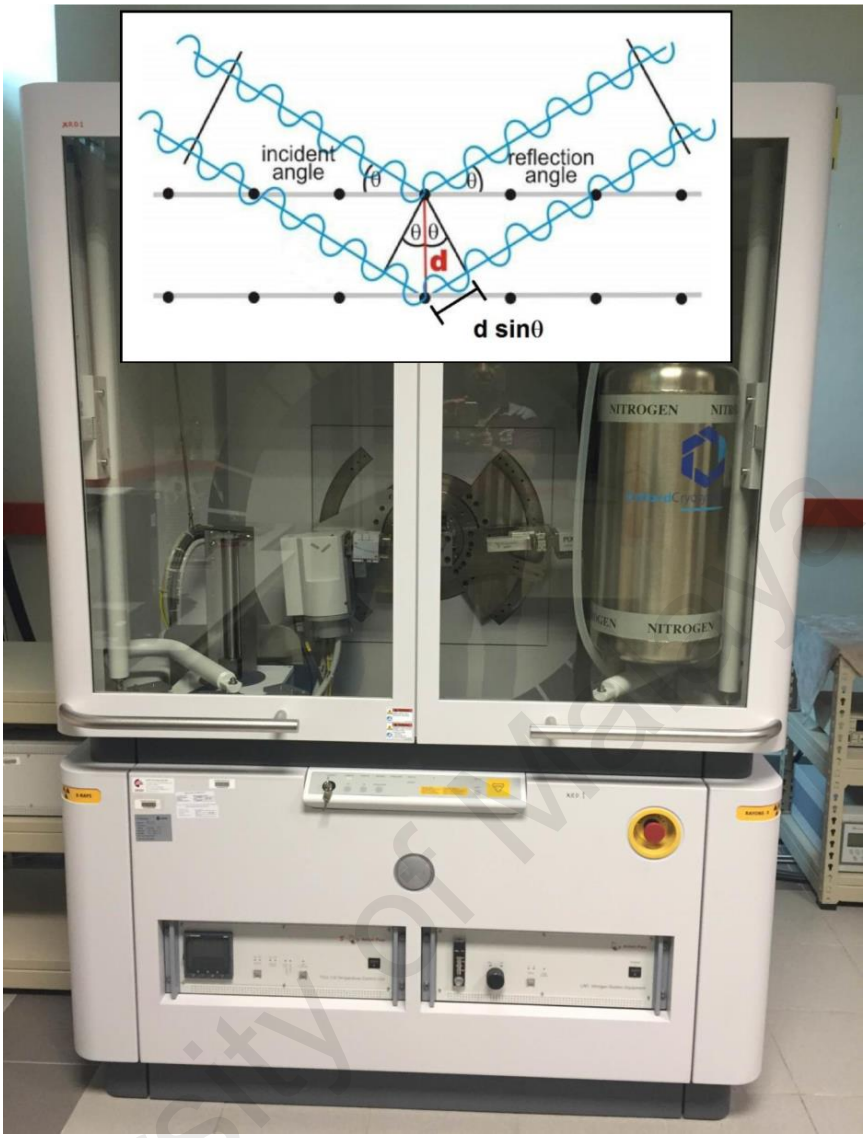

Figure 3.6: Schematic of the diffraction of an X-ray beam by parallel atomic planes in crystallite materials

The crystallite sizes of nanopowders were determined by means of the X-ray line broadening method using the Scherrer equation: $D=k\lambda/\beta\cos\theta$, where D is the particle size in nanometers, λ is the wavelength of the radiation (1.54056 Å for CuKα radiation), k is a constant equal to 0.94, B is the corrected peak width at half-maximum intensity and θ is the peak position.

3.5.2 Fourier Transforms Infrared Spectroscopy (FTIR)

The most useful tool for identifying chemicals, organic or inorganic, is FTIR machine. This tool can be used to analyze materials in the liquids, solid, and gasses. The

characteristic of the chemical bond can be detected from the wavelength of the absorbed light as can be seen in the spectrum. The chemical bonds of the molecule can be determined by studying the infrared absorption spectrum. Each pure compound has a unique FTIR spectra that called fingerprint. Although the spectrum of an organic material is very rich and detailed, inorganic compounds have a simple absorption spectra. For example, ZnO has and absorption bond around 400 cm^{-1}. Therefore, the unknown materials can be identified by comparison of their spectrum to a library of known compounds. The FTIR machine that used was Fourier transform-infrared (FT-IR) spectrometer (1650; Perkin Elmer,Waltham, MA). The absorption bonds between 280 to 4000 cm^{-1} can be detected by this machine which gives us this ability to detect two of the absorption bonds of ZnO Figure 3. 7.

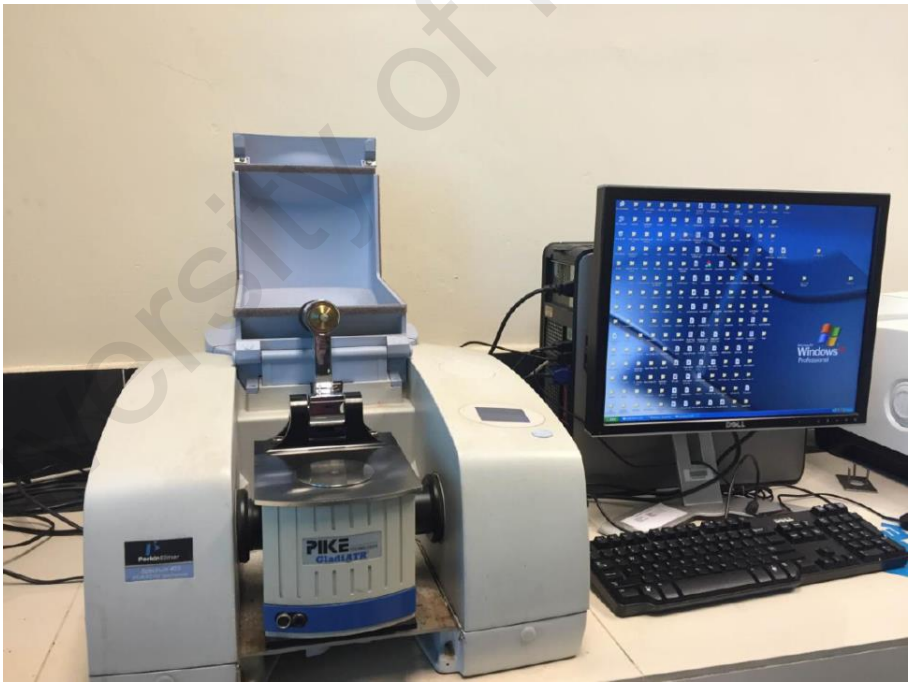

Figure 3.7: Schematic of the Fourier Transforms Infrared Spectroscopy (FTIR)

3.5.3 High resolution transmission electron microscope

HRTEM is a technique used to study the microstructure of the materials. This is a tool that produce the two-dimensional image of the desired sample. In this technique, a focused beam of electrons is projected and interact with the sample. This interaction causes the scattering of electrons. So, by this way a final image is taken from the incident and diffracted beam. The working principle of the HRTEM is similar to a simple microscope. The projection lenses are used for the illumination of the sample, and so the image of the sample is being projected on a screen. In HRTEM, the electromagnetic lenses are used to give the pathway or to guide the beam of electrons while in a simple microscope the glass lenses are used. In this thesis, Hitachi H-7100 and JEOL JEM-2100F TEM are used. In order to prepare sample for TEM, one or two drops of the sample dispersed in water or ethanol followed by drop casting onto carbon coated copper grid. The copper grid is placed in an oven to evaporate the excess solvent Figure 3. 8.

Figure 3.8: Schematic of the high-resolution transmission electron microscope

3.5.4 Transmission Electron Microscopy (TEM)

Transmission electron microscopy (TEM) is a microscopy technique whereby a beam of electrons is focused onto an ultra-thin specimen and transmitted through it, interacting with the specimen as it passes through. As a result of this interaction, an image is formed. The image is magnified and focused onto an imaging device, such as layer of photographic film or fluorescent screen or is detected using a sensor (e.g., CCD camera). In this work a Hitachi H-7100 electron microscopy is used in TEM studies. To prepare sample to use for TEM, a little amount of powders was dispersed in ethanol. The concentration of the suspension should be controlled and depends on the type of the material. One or two drops of the solution are poured on top surface of copper grid. The copper grid is placed in an oven at 40 °C for one day.

3.5.5 Field emission scanning electron microscopy (FESEM)

Scanning electron microscopy (SEM) is one of the most versatile and well known analytical techniques. Compared to a conventional optical microscope, an electron microscope offers advantages that include high magnification, large depth of focus, and high resolution, as well as easy sample preparation and observation. In this technique, electrons generated from an electron gun enter the surface of the sample and generate many low energy secondary electrons. The intensity of these electrons is governed by the surface topology of the sample. An image of the sample surface is therefore constructed by measuring secondary electron intensity as a function of the position of the scanning primary electron beam. In our microscopy lab, a state-of-the-art, high resolution FEI Quanta 200F field emission scanning electron microscopy (FESEM) from OXFORD is available. To prepare a sample from the powders, first, a little amount of the powders was dispersed in acetone and then poured on top surface of a silicon wafer, because silicon is conducting a clear picture can be obtained. Finally, the coated silicon was dried at 50 °C for 1h Figure 3. 9.

Figure 3.9: Schematic of the Field emission scanning electron microscopy (FESEM)

3.5.6 Ultraviolet-visible spectroscopy (UV-vis)

Ultraviolet and visible (UV-Vis) absorption spectroscopy can be described as the measurement of the attenuation of a light beam after reflection from a sample surface or after it passes through a sample. A single wavelength over an extended spectral range can be used for absorption measurements. Infrared spectroscopy looks at vibrational motions but ultraviolet-visible spectroscopy looks at transitions of electrons. Because, ultraviolet and visible light are energetic enough to excite outer electrons to go to higher energy levels. Although UV-Vis spectra have broad features that are of limited use for sample identification, they are very helpful for quantitative measurements. UV-Vis spectroscopy is used to characterize the absorption, transmission, and reflectivity of several of technologically important materials, such as pigments, coatings, windows, and filters. Also, it is used to calculate the optical properties of materials. For example, the absorption spectrum can be used to calculate optical band gap. Several methods are

used for this, such as Kubelka–Munk model and first derivative methods as mentioned in literature. For this work, the Thermal Scientific Evolution 300 UV-vis spectrophotometer was used to get the absorption spectra of the materials in liquid dispersed form in the range of 200 to 1000 nm, in powder form in the range of 300 to 750 nm.

3.5.7 Raman Spectroscopy

The Raman spectra of all ZnS-graphene composite were obtained using a CRM200 Confocal Raman Microscope (WITec GmbH, Ulm, Germany) employing a 532-nm excitation wavelength to confirm the reduction of graphene. Excitation was provided by a HeNe laser (Melles Griot). The exciting laser radiation was coupled into a Zeiss microscope through a wavelength-specific single mode optical fiber. The incident laser beam was collimated via an achromatic lens and passes a holographic band-pass filter before it was focused onto the sample through the microscope objective. The sample is located on a piezo-electrically driven microscope scanning stage with an x, y resolution of ca. 3 nm and a repeatability of ±5 nm, and *z* resolution of ca. 0.3 nm and ±2 nm repeatability. The Raman back-scattered radiation was detected by a back-illuminated deep depletion, 1024×128 pixel charge-coupled device camera operating at -82^{o} .

3.5.8 Photoluminescence spectroscopy (PL)

The room temperature PL experimental set-up is the Renishaw System 2000. The PL system is excited with a 20mW He-Cd laser working at 325nm (3.815eV) and is detected in a back-scattering geometry through a photomultiplier and lock-in amplifier. The low-temperature PL system is computer-based controlled. The sample is located in a cryostat, which allows the measuring temperature to be adjusted from about 4 K to room temperature. The resulting luminescence is collected through two lenses and is coupled into a SPEX 750M monochromator by which the luminescence is then

spectrally dispersed. Then, a photomultiplier tube (PMT) that is suitable for detecting light from near-UV to 1200 nm detects the dispersed luminescence. The DC signals produced by the PMT are measured using a Stanford Research Systems SR830 lock-in amplifier, and data are recorded and processed by computer system.

CHAPTER 4: CHAPTER IV: RESULTS AND DISCUSSIONS

4.1 Synthesis and characterization of ZnO NPs/reduced graphene oxide nanocomposite prepared in gelatin medium as highly efficient photo-degradation of MB

In this study, ZnO nanoparticles (NPs) were decorated on a graphene oxide (GO) sheet via the sol–gel method in a gelatin medium. Long-chain gelatin compounds were utilized to terminate the growth of the ZnO-NPs on GO and stabilize them. The obtained products were post-annealed at 400 ^{o} C to remove the gelatin and produce a reduced graphene oxide (RGO) sheet. Microscopic studies showed that the NPs were dispersed on the GO sheet. They had a spherical shape and a size of approximately 19 nm. In addition, these studies revealed that the NPs were single crystals. The X-ray diffraction pattern of the NPs indicated a hexagonal (wurtzite) structure. The results of Fourier transform infrared spectroscopy (FTIR) revealed that the GO sheet was transformed into RGO by the post-annealing process. The obtained ZnO-NPs/RGO nanocomposite was used as photocatalyst to remove methylene blue (MB). Observations showed that the efficiency of the photocatalyst activity of the ZnO NPs was significantly increased by RGO.

Figure 4. 1 shows FESEM and TEM images of the ZnO NPs that were decorated on the GO sheet. It can be seen in the FESEM image (Figure 4.1 (a)) that the entire area of the GO sheet is covered by the ZnO NPs. The inset of Figure 4. 1(a) shows that the ZnO NPs have a spherical shape. The TEM image reveals that the ZnO NPs are dispersed on the GO (Figure 4. 1(b)). In addition, the TEM image shows an average particle size of approximately 19±2 nm for the NPs. The inset of Figure 1(b) shows an HRTEM image of a single nanoparticle. As can be seen, the nanoparticle is a single crystal with a high crystal quality, and there is no defect from a stacking fault. In addition, the HRTEM image shows that the lattice distance is approximately 0.26 nm, which is consistent with

the distance along the c-axis of a bulk wurtzite ZnO crystal. Therefore, based on the HRTEM image, the nanoparticles were grown along the [001] direction without any defects.

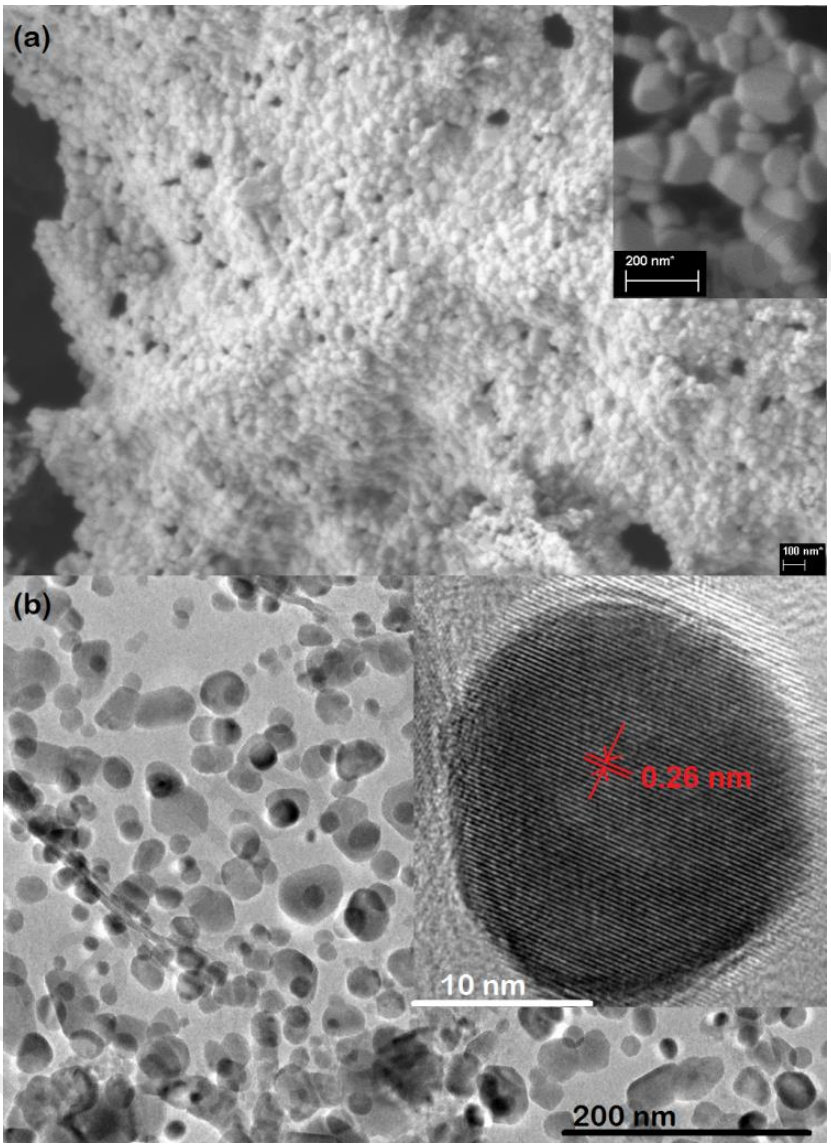

Figure 4.1: (a) FESEM image of ZnO-NPs on the GO sheet. The inset shows ZnO nanoparticles that were deposited on the GO. (b) TEM image of dispersed ZnO NPs on the GO. The inset shows an HRTEM image of a single ZnO nanoparticle

The XRD patterns of the obtained products are shown in Figure 4. 2 The XRD pattern of GO indicates an intense and sharp diffraction peak at $2\theta=10.6^{o}$, attributed to the (001) lattice plane corresponding to a d-spacing of 0.83 nm. This is consistent with the lamellar structure of GO. In addition, Figure 4. 2 shows the XRD pattern of the

ZnO-NPs that are decorated on the GO sheet. All the detectable peaks can be indexed to the ZnO wurtzite structure (Ref. code: 00-036- 1451). It can be seen that there are no peaks from GO or other impurities in the XRD pattern of the ZnO NPs. This could be due to the transformation of GO to RGO, with the RGO peaks not appearing because of the strong peak of the ZnO NPs in the XRD pattern. However, additional characterization is needed to explain this phenomenon.

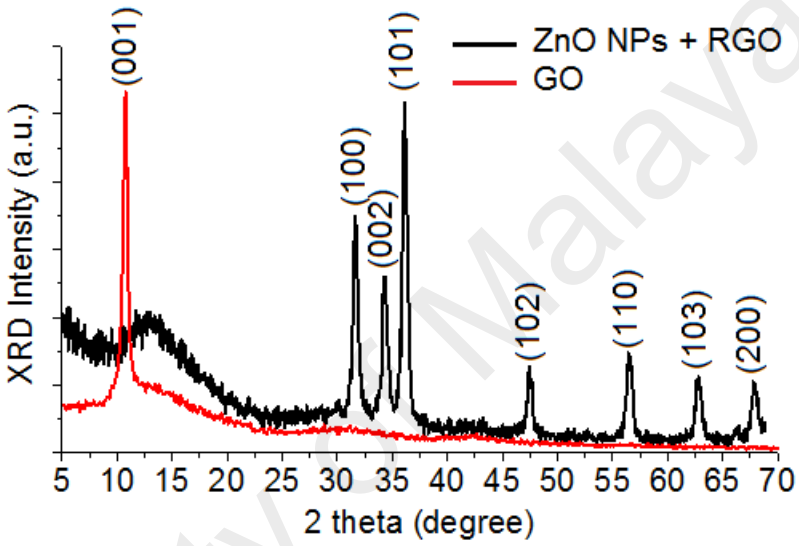

Figure 4.2: XRD patterns of the GO sheet and ZnO-NPs/GO composite

Figure 4. 3 shows the FTIR spectra of the pristine GO and ZnO NPs/ GO nanocomposite. In the FTIR spectrum for GO, the broad peak centered at 3190 cm^{-1} is attributed to the O–H stretching vibrations, and the peaks at 1731, 1625, 1183, and 1040 cm^{-1} are assigned to the C=O stretching, sp^2-hybridized C=C group, O–H deformation, C–OH stretching, and C–O stretching, respectively (Shen et al., 2011). In contrast, the peaks at 1731 and 1183 cm^{-1} are missing from the FTIR spectrum of the ZnO-NPs/GO nanocomposite, which indicates the reduction of GO and its transformation into RGO (Ren, Yan, Ji, Chen, & Li, 2011; Zou, Zhu,Sun, & Wang, 2011). In fact, the post-annealing process at 400 ^oC not only removed the gelatin but also caused the transformation of GO to RGO. Therefore, the obtained nanocomposite consisted of ZnO

NPs decorated on an RGO sheet. The broad peak at 3250 cm^{-1} in the FTIR spectrum of the ZnO-NPs/GO nanocomposite might be attributed to the O–H stretching vibration of absorbed water molecules. In addition, the FTIR spectrum of ZnO-NPs/RGO shows a peak at 431 cm^{-1}. The band at 431 cm^{-1} corresponds to the E_2 mode of hexagonal ZnO (Raman active) (Zak, Abd Majid, Darroudi, & Yousefi, 2011).

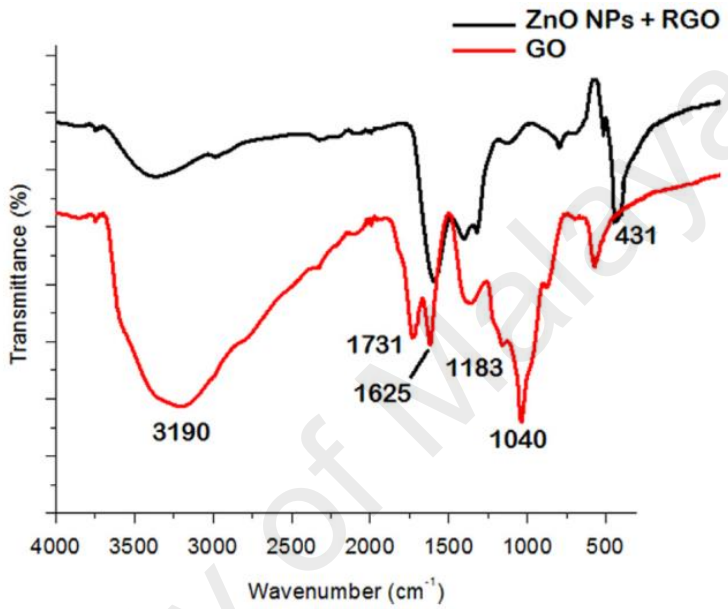

Figure 4.3: FTIR spectra of the GO sheet and ZnO-NPs/RGO composite

UV–vis absorption spectra of ZnO NPs and ZnO-NPs/RGO at room temperature are shown in Figure 4. 4 These spectra reveal a characteristic absorption peak for ZnO at a wavelength of 360 for both samples, which can be assigned to the intrinsic bandgap absorption of ZnO, owing to the electron transitions from the valence band to the conduction band (O_{2p}-Zn_{3d}) (Sáaedi et al., 2013). As can be seen, the peak position of the UV–vis spectrum of ZnO NPs has not been affected by the graphene. However, it is observed that the absorbance of the ZnO-NPs/RGO composite increases in comparison to the absorbance of the ZnO NPs. Such an increase in absorbance may be due to the absorption contribution from RGO, the increase in the surface electric charge of the oxides, and the modification of the fundamental process of electron–hole pair formation

during irradiation (Xu, Zhang, Cheng, & Zhu, 2011). Therefore, the presence of RGO in ZnO can increase the light absorption intensity and range, which is beneficial to the photocatalytic performance.

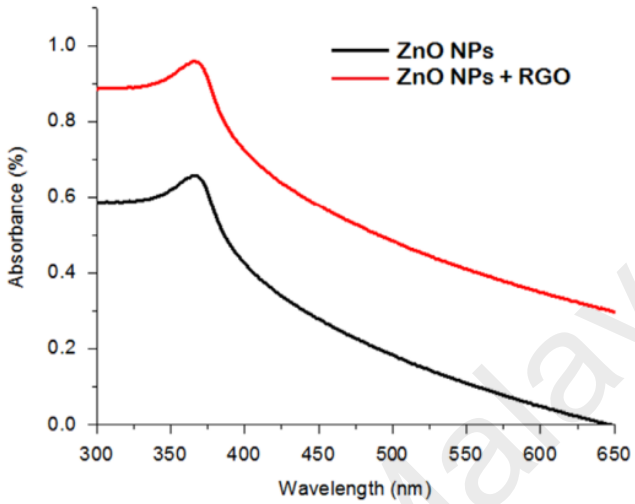

Figure 4.4: UV–vis absorption spectra of the GO sheet and ZnO-NPs/RGO composite

Figure 4. 5 (a) illustrates the optical absorption spectra of the MB aqueous solution with 10 mg of the as-prepared ZnO-NPs/ RGO composite after exposure to UV light irradiation for different intervals of times. It can be seen that the intensity of the absorption peak of MB at 663 nm decreases with an increase in the irradiation time, which indicates that the MB molecules are degraded by the catalysis. Figure 4. 5 (b) shows the relative concentration (C_t/C_0) of MB as a function of time, where C_t is the concentration of MB at the irradiation time t, and C_0 is the concentration of the dye before irradiation. The result is plotted against those of the as-prepared ZnO-NPs/ RGO and ZnO NPs under same conditions. The MB solution was degraded by as much as 99.5% by the ZnO-NPs/RGO and by approximately 63% by the ZnO NPs. This indicates the higher photocatalytic activity of the ZnO-NPs/RGO. In fact, the wide surface of RGO causes the ZnO NPs to disperse. Therefore, the dispersed NPs absorb more light and generate more electron–hole pairs to remove dye molecules.

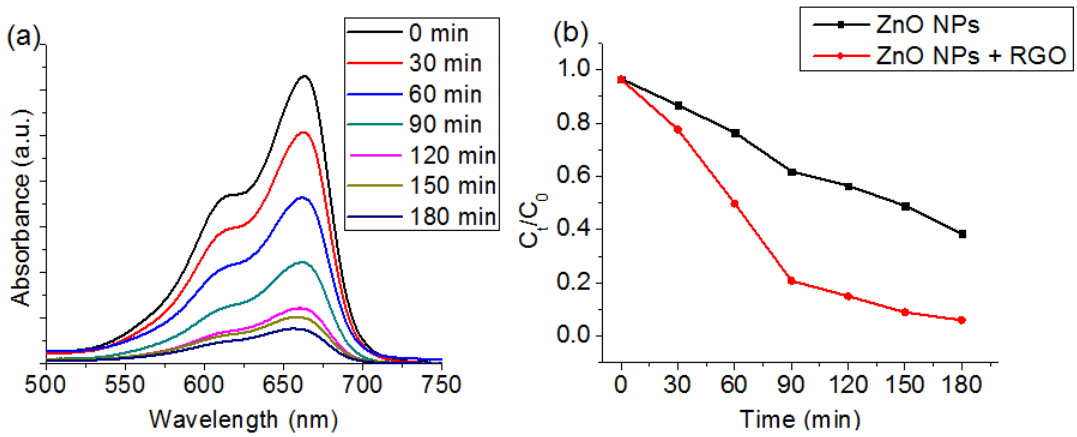

Figure 4.5: (a) The UV–vis absorbance of MB over time during photocatalytic degradation under UV light irradiation using ZnO-NPs/RGO. (b) Photocatalytic degradation of MB by ZnO NPs and ZnO-NPs/RGO under UV light irradiation

4.2 Effects of graphene oxide concentration on optical properties of ZnO/RGO nanocomposites and their application to photocurrent generation

In this study, the effects of different concentrations of graphene oxide (GO) on the structure and optical properties of ZnO nanoparticles (NPs) were investigated. The nanocomposites were synthesized via the sol-gel method in a gelatin medium. X-ray diffraction patterns (XRD) and Fourier transform infrared spectroscopy indicated that the GO sheets were reduced and changed to reduced GO (RGO) during the calcination of the nanocomposites at 400 ^{o} C. In addition, the XRD patterns of the NPs indicated a hexagonal (wurtzite) structure for all the products. Microscopic studies showed that the NPs were decorated and dispersed on the RGO sheets very well. However, these studies revealed that the RGO concentration had an effect on the crystal growth process for the ZnO NPs. Furthermore, these studies showed that the NPs could be grown with a single crystal quality in an optimum RGO concentration. According to the XRD results that were obtained from pure ZnO NPs, the calcinations temperature was decreased by the RGO. UV–vis and room temperature photoluminescence studies showed that the optical properties of the ZnO/RGO nanocomposite were affected by the RGO concentration. Finally, the obtained ZnO/RGO nanocomposite was used to generate a photocurrent.

Observations showed that the photocurrent intensity of the nanocomposite was significantly increased by increasing the RGO, with an optimum RGO concentration.

The XRD patterns of the obtained products are shown in Figure 4. 6. The XRD pattern of GO indicates an intense and sharp diffraction peak at $2\theta=10.6^{o}$, which is attributed to the (001) lattice plane corresponding to a d-spacing of 0.83 nm. This is consistent with the lamellar structure of GO. In addition, Figure 4. 6 shows the XRD patterns of the ZnO/GO composites with low (RGO1), mid (RGO2), and high (RGO3) GO concentrations. All of the detectable peaks can be indexed to the ZnO wurtzite structure (Ref. code: 00-036-1451). As can be seen, there are no peaks from GO or other impurities in the XRD patterns of the ZnO/GO composites. This could be due to the transformation of GO to RGO, with the RGO peaks, which are shown in Figure 4. 6, not appearing here because of the strong peak for the ZnO in the XRD patterns. However, the intensities of the XRD peaks decrease with an increase in the GO concentration. This could be because the amount of ZnO decreased in the composite, which resulted in a decrease in the XRD peak intensities.

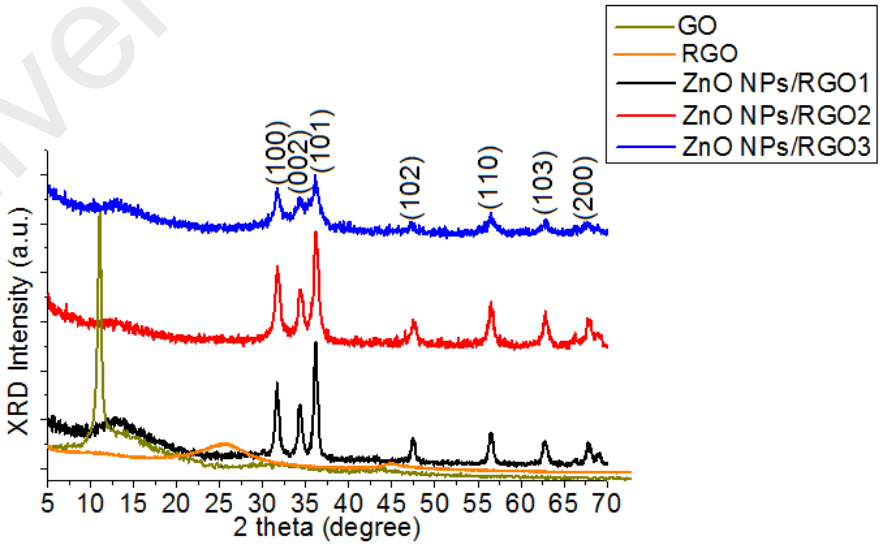

Figure 4.6: XRD patterns of the GO, RGO sheets and ZnO/RGO nanocomposites with different concentrations of the GO

Figure 4. 7 shows the FTIR spectra of the pristine GO, gelatin powder, and ZnO-NPs/RGO nanocomposites. In the FTIR spectrum for GO, the broad peak centered at 3190 cm_1 is attributed to the O–H stretching vibrations, and the peaks at 1731, 1625, 1183, and 1040 cm^{-1} are assigned to the C=O stretching, sp^2-hybridized C=C group, O–H deformation, C–OH stretching, and C–O stretching, respectively(Hummers Jr & Offeman, 1958). In contrast, the peaks at 1731, 1183, and 1040 cm^{-1} are missing from the FTIR spectra of the ZnO-NPs/GO nanocomposites, which indicate the reduction of GO and its transformation into RGO (Huang et al., 2014; Ren et al., 2011). In addition, FTIR spectrum of gelatin powder is shown in Figure 4. 7. It can be seen that the gelatin's peaks are decreased dramatically in the FTIR spectra of the ZnO-NPs/RGO nanocomposites. In fact, the post-annealing processes at 400 ^{o} C not only caused the transformation of GO to RGO but also removed the gelatin, which is good agreement with the XRD results. In addition, the FTIR spectra of ZnO-NPs/RGO show a peak at 437 cm^{-1}. The band at 437 cm^{-1} corresponds to the E_2 mode of hexagonal ZnO (Raman active) (Zak, Abd Majid, et al., 2011). Therefore, the obtained nanocomposite consisted of ZnO NPs decorated on an RGO sheet.

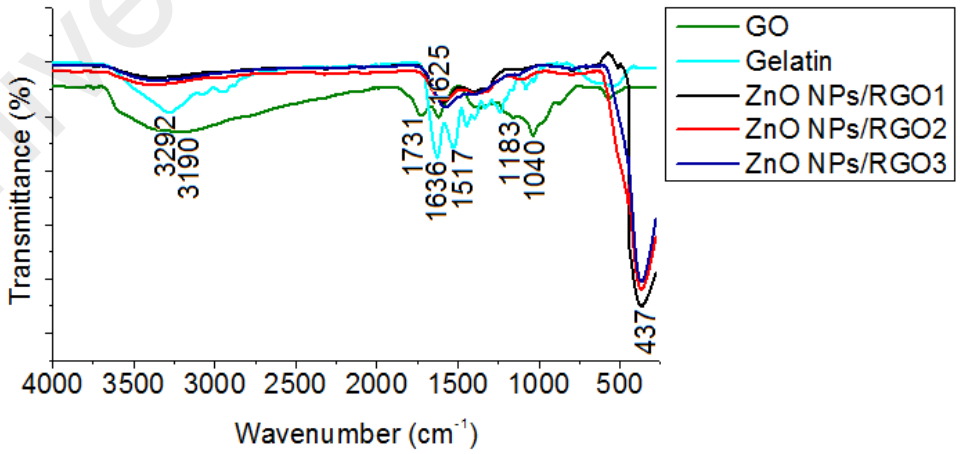

Figure 4.7: FTIR spectra of the GO sheet, gelatin powder, and ZnO-NPs/RGO composites

Figure 4. 8(a-c) show TEM images of the ZnO/RGO composites with different concentrations for the RGO sheets. The TEM images reveal that the ZnO NPs are decorated and dispersed on the RGO sheets. However, this dispersion is less for ZnO/RGO1 than for the other samples. Figure 4. 8 (c) shows that the ZnO population in ZnO/RGO3 is less than that in the other samples. This explains why the XRD peak intensities decreased with an increase in the GO concentration. In addition, the TEM images show an average particle size of approximately 19.6 nm for the NPs in all samples. Figure 4. 8 (a'–c') show HRTEM images of single nanoparticles from sheets with different RGO concentrations. These HRTEM images show that the concentration of the RGO sheet affects the crystalline quality of the NPs. It can be observed that there are several areas of damage and defects for the ZnO nanoparticles, which were grown on the sheets with the low and high concentrations of RGO (Figures 4. 8(a') and 4. 8(c')). On the other hand, the crystalline space of the ZnO/RGO2 nanocomposite is clear and shows a nondefective structure for the nanoparticle (Figure 4. 8(b')). In fact, the HRTEM results are in good agreement with the XRD results. In addition, the HRTEM image of the ZnO/RGO2 nanocomposite shows that the lattice distance is approximately 0.26 nm (Figure 4. 8(b')), which is consistent with the distance along the c-axis of a bulk wurtzite ZnO crystal. Therefore, based on the HRTEM image, the nanoparticles were grown along the [001] direction without any defects.

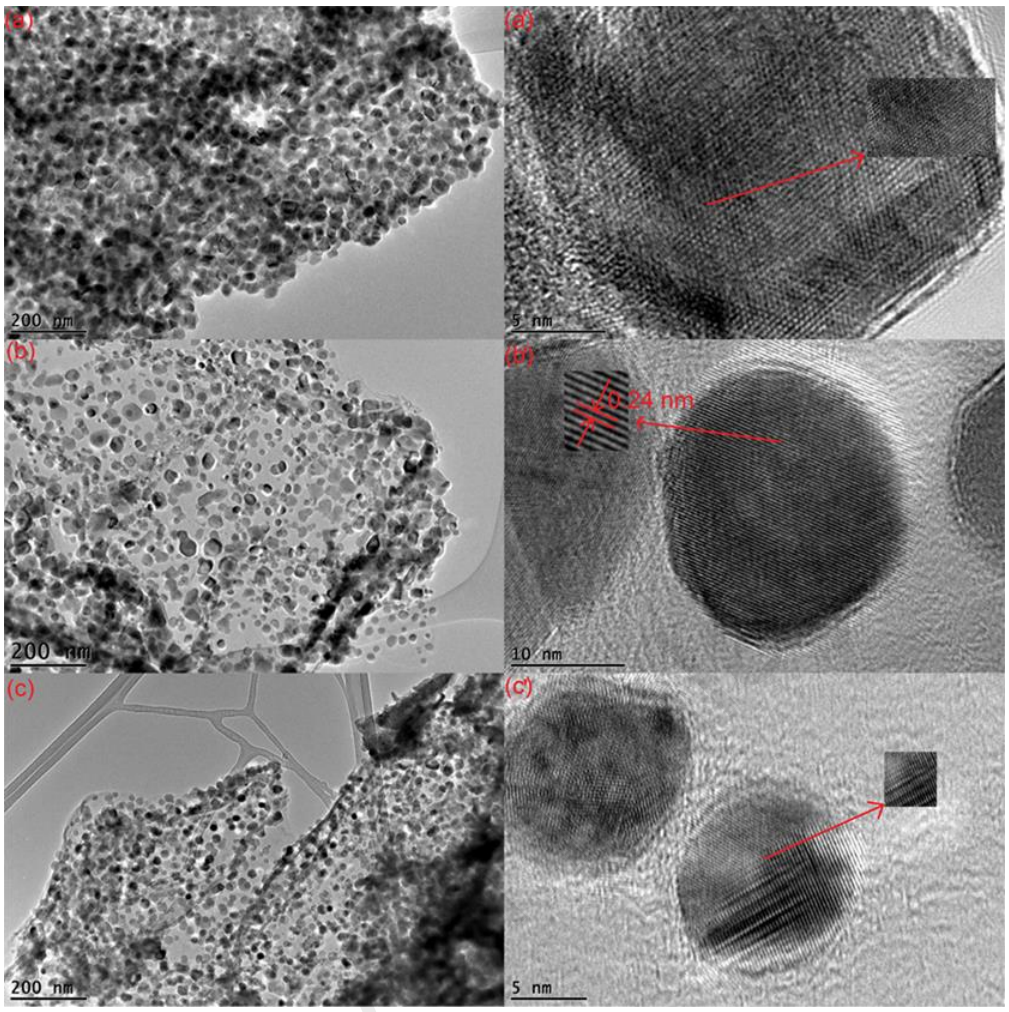

Figure 4.8: TEM image of the ZnO/RGO nanocomposites with (a) low RGO concentration (ZnO-NPs/RGO1), (b) mid RGO concentration (ZnO-NPs/RGO2), and (c) high RGO concentration (Zn ONPs/ RGO3). HRTEM image of the ZnO NPs that were decorated on the RGO sheet with (a') low RGO concentration, (b') mid RGO concentration, *and* (c') high RGO concentration

Figure 4. 9 shows TEM image of the ZnO/RGO2 nanocomposites with more details. As can be seen, the NPs were dispersed on the RGO sheet very well. In addition, it can be observed that most of the NPs have a hexagonal shape.

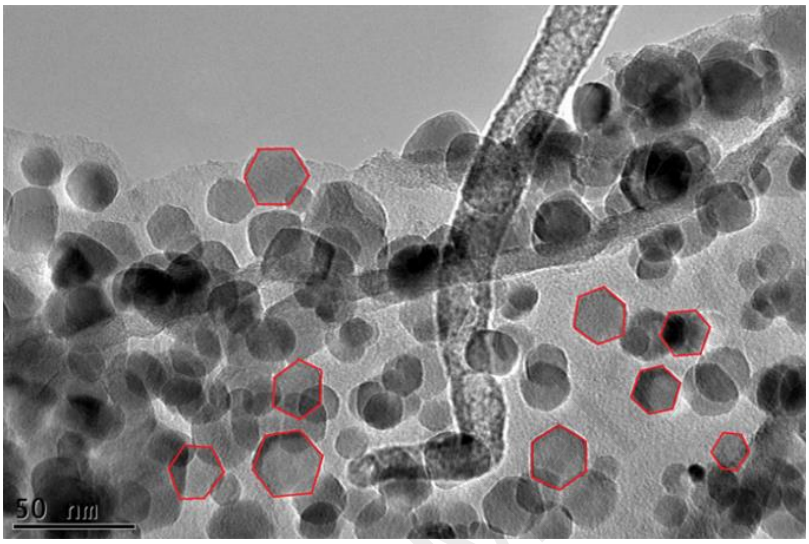

Figure 4.9: High magnification of TEM image of the ZnO/RGO2 nanocomposites

To better understand the effects of the RGO sheets on the growth process for the ZnO NPs, ZnO NPs were synthesized without graphene at 400 and 500 ^{o} C. The XRD patterns of these conditions are shown in Figure 4. 10. It can be observed that the XRD pattern of the NPs that were sintered at 400 ^{o} C indicates a low crystalline quality. On the other hand, the XRD pattern of the NPs that were sintered at 500 ^{o} C indicates a good crystalline quality. In addition, the TEM images for NPs sintered under these conditions confirm the XRD results (Figure 4. 11). Furthermore, these TEM images show that the NPs were not very well dispersed without the RGO sheet. According to the obtained results, it can be concluded that the RGO sheets not only play a role as a dispersion site for the NPs but also play a role as a useful site to grow ZnO NPs. In fact, the RGO sheets could decrease the calcination temperature. The widely-accepted mechanism for the synthesis of graphene decorated with inorganic nanostructures is the attraction of positively charged metal ions by the polarized bonds of the functional

groups on the GO. The attachment of these metal ions to the surface and edges of the GO results in a redox reaction and the formation of nucleation sites, which eventually lead to the growth of nanostructures on the 2-D graphene sheets (Xue et al., 2011).

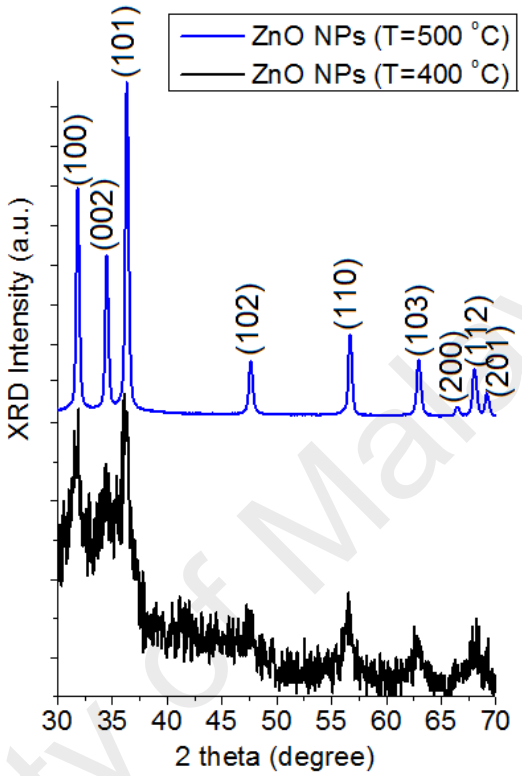

Figure 4.10: XRD patterns of the pure ZnO NPs that were grown by 400 and 500 ^{o} C temperature

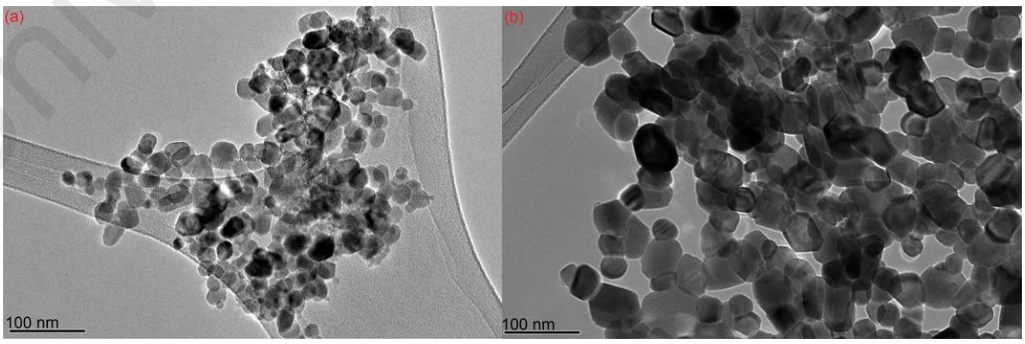

Figure 4.11: TEM image of the pure ZnO NPs that were grown at (a) 400 ^{o} C and (b) 500 ^{o} C

Optical studies were carried out using UV–vis and PL spectrometers. Figure 4. 12(a) shows the UV–vis spectra of the pure ZnO NPs that were sintered at 400 ^{o} C and

the ZnO/ RGO nanocomposites with sheets having different RGO concentrations. The UV–vis spectra reveal a characteristic absorption peak for ZnO at a wavelength of 360 nm for all the samples, which can be assigned to the intrinsic band-gap absorption of ZnO, owing to the electron transitions from the valence band to the conduction band ($O_{2p} \rightarrow Zn_{3d}$) (Sáaedi et al., 2013). As can be seen, the peak position of the UV–vis spectrum of the ZnO NPs has not been affected by the graphene. However, it is observed that the absorbance of the ZnO/RGO nanocomposites increases in comparison to the absorbance of the ZnO NPs until an optimum concentration of graphene. Such an increase in absorbance may be due to the absorption contribution from RGO, the increase in the surface electric charge of the oxides, and the modification of the fundamental process of electron–hole pair formation during irradiation (Xu et al., 2011). Therefore, the presence of RGO in ZnO can increase the light-absorption intensity and range, which is beneficial to the optoelectronic performance. However, increasing the graphene concentration beyond an optimum content could affect the crystalline quality of the ZnO NPs, which were decorated on the RGO, as a result of a decrease in the ZnO NPs population on Zn/RGO3 nanocomposites.

Figure 4. 12(b) shows the PL spectra of the products. A significant difference can be seen between the PL spectrum of the pure ZnO NPs, which were grown at 400 ^{o} C, and that of the ZnO/RGO nanocomposites. The PL spectrum of the pure ZnO NPs shows no detectable UV peak and a strong and broad peak in the visible region. The UV emission is also called the near-band-edge (NBE) emission because of the recombination of free excitons through an exciton–exciton collision process. It has been suggested that the green band emission (deep level emission (DLE)) corresponds to a singly ionized oxygen vacancy in ZnO and results from the recombination of a photo-generated hole with the singly ionized charge state of this defect. Therefore, Figure 4. 12(b) shows that the ZnO NPs have very high concentrations of oxygen vacancies.

However, the intensity of the UV peak is increased and that of the visible peak is decreased by increasing the graphene concentration. However, the UV/DLE ratio of the ZnO/ RGO2, which is one of the main factors that is usually used for comparing the optical properties of samples, is bigger than the UV/DLE ratios of the other nanocomposites. Therefore, the ZnO/RGO2 nanocomposites have a better relative crystalline quality. According to these results, it can be understood that the graphene concentration has an optimum value in relation to improving the optical quality of the ZnO NPs. In fact, the optical study results are in good agreement with the XRD and TEM results. Therefore, the ZnO/RGO2 nanocomposite is the best composite of ZnO and RGO for improving the crystalline and optical quality of the ZnO NPs, which were sintered at a lower temperature than is normally used to grow pure ZnO NPs by the sol–gel method in a gelatin medium.

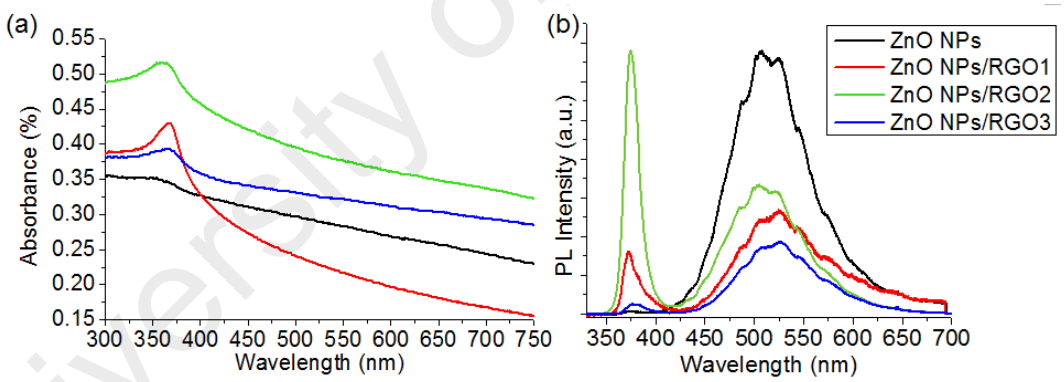

Figure 4.12: (a) UV-vis spectra of the pure ZnO NPs, ZnO/RGO1, ZnO/RGO2, and ZnO/RGO3 nanocomposites. (b) PL spectra of the pure ZnO NPs, ZnO/ RGO1, ZnO/RGO2, and ZnO/RGO3 nanocomposites

Figure 4. 13 shows the Raman spectrum of the ZnO/RGO2 nanocomposite. It is established that the graphene obtained by the chemical reduction of GO exhibits two characteristic main peaks: the D band at 1361 cm^{-1} arising from a breathing mode of j-point photons of A_{1g} symmetry and the G band at 1604 cm^{-1} arising from the first order scattering of the E_{2g} phonons of sp^2 C atoms (Gao et al., 2010). In comparison to the pristine GO, the Raman spectra of the ZnO/RGO2 nanocomposite show that the D and

G bands shifted to lower wave numbers at 1346 and 1593 cm^{-1}, respectively. This is because of the reduction process for the GO, which can be supported by gelatin as the reducing, capping, and stabilizing agent (Liu et al., 2011). In addition to the peaks associated with the D and G bands of graphene, the Raman spectrum of the ZnO/RGO2 nanocomposite has one sharp peak at 437 cm^{-1} corresponding to the E_2 (high) mode of the Raman active mode, a characteristic peak for the wurtzite hexagonal phase of ZnO, which is in good agreement with the FTIR results. The Raman results confirmed that the ZnO/RGO2 nanocomposite was composed of graphene nanosheets and pure ZnO.

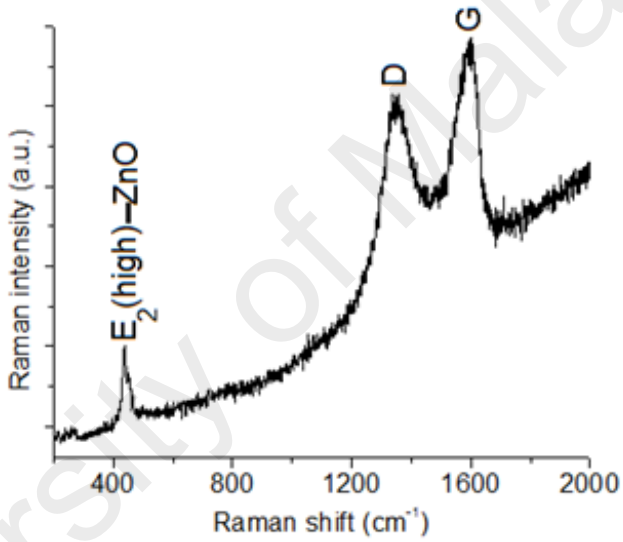

Figure 4.13: Raman spectrum of the ZnO/RGO2 nanocomposites

Figure 4. 14 shows the photocurrent responses of ZnO NPs and ZnO/RGO nanocomposites with different concentrations of GO. The photocurrent generation was increased by the introduction of graphene nanosheets. A plausible reason is that the photogenerated electrons on the conduction band of ZnO NPs are trapped by the graphene nanosheets, which prevents the photogenerated electrons and holes from recombining (Ferrari et al., 2014). In addition, the photocurrent generation of the ZnO/ RGO nanocomposite increases with an increase in the concentration of RGO. In fact, the charge separation efficiency increases due to the electronic interaction between ZnO

and RGO in the composite. However, a further increase in the RGO concentration leads to a decrease in the photocurrent generation. The reason is the same as that described in the sections on the XRD and PL studies. In fact, the decrease in the ZnO NP population due to an increase in the GO concentration causes a decrease in the photogenerated electrons and holes. Hence, the optimum concentration of GO is a very important factor that should be considered to generate a high current density. A comparison results between the present work and previous report show that efficiency of the photocurrent in the present work is 50% higher than the photocurrent efficiency of the ZnO/RGO nanocomposites that were synthesized by a simple chemical bath deposition (Tian et al., 2012). but it is around 60% and 80% lower than other complex, expensive, and time-consuming techniques (Fu et al., 2012; Luo et al., 2012). However, the advantage of our method to obtain these results is its simplicity. In addition, the sol-gel method that has been used in this research is a cost-effective method that is most important to synthesize this type of nanocomposites for different applications.

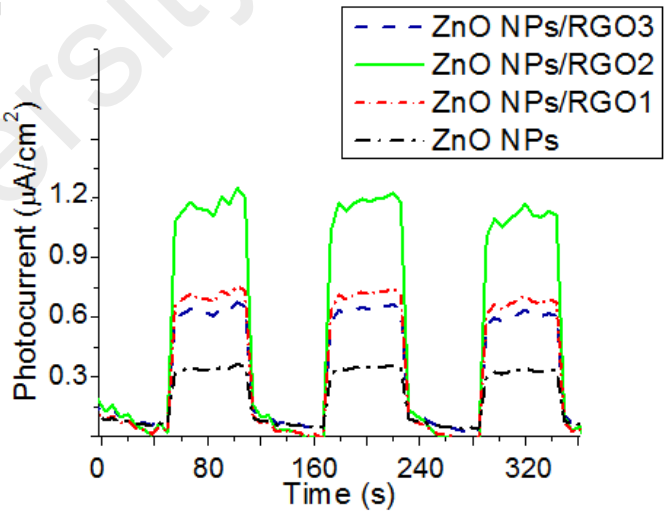

Figure 4.14: Photocurrent response of the ZnO NPs and ZnO/RGO nanocomposites with different concentrations of the RGO

4.3 One-pot sol–gel synthesis of reduced graphene oxide uniformly decorated zinc oxide nanoparticles in starch environment for highly efficient photodegradation of Methylene Blue

In this study, ZnO NPs+reduced graphene oxide (rGO) nanocomposites were synthesized using a sol–gel method with starch as the polymerisation agent. Long-chain starch compounds were used to terminate the growth of the ZnO NPs on rGO and stabilise them. The resulting products were annealed at 350°C to remove the starch and produce a reduced graphene oxide (rGO) sheet in one-pot without any post-annealing processes. Microscopic studies showed that the NPs were dispersed on the rGO sheet. They had a spherical shape and a size of approximately 25±10 nm. In addition, these studies revealed that the NPs were single crystals. The X-ray diffraction pattern of the NPs indicated a hexagonal (wurtzite) structure. The results of Fourier transform infrared spectrum analysis (FTIR) revealed that the GO sheet was transformed into rGO via the sol-gel method in the starch environment. The results of photoluminescence spectroscopy demonstrated that the incorporation of reduced graphene oxide (rGO) sheets with ZnO NPs suppressed the electron‑hole recombination of the composite. Therefore, a significant enhancement in the photocatalytic degradation of methylene blue (MB) was observed with the ZnO NPs + rGO nanocomposite compared to the bare ZnO nanoparticles.

4.3.1 Crystalline structure

The XRD patterns of the resulting products are shown in Figure 4. 14. The XRD pattern of GO indicates an intense and sharp diffraction peak at $2\theta = 10.6°$, attributed to the (001) lattice plane corresponding to a d-spacing of 0.83 nm, which is consistent with the lamellar structure of GO. In addition, Figure 4. 15 shows the XRD pattern of the ZnO NPs that were decorated on the rGO sheet. All of the detectable peaks can be

indexed to the ZnO wurtzite structure (JCPDS card no: 00-036-1451). There are no peaks from GO or other impurities in the XRD pattern of the ZnO NPs. This result could be because of the transformation of GO to rGO; the rGO peaks do not appear here because of the strong peak for the ZnO NPs in the XRD pattern. Furthermore, this pattern shows the XRD results for the ZnO NPs. The ZnO NPs, which were synthesized under the same conditions in a starch environment, do not show crystalline behaviour. Thus, the GO sheets can use a reduced calcination temperature to form ZnO crystals in starch environments. Further characterisations will also confirm these results.

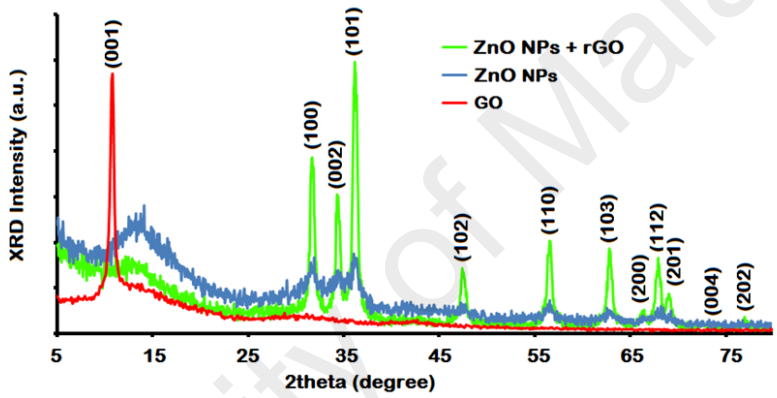

Figure 4.15: XRD patterns of the GO sheet, ZnO NPs, and ZnO NPs+rGO nanocomposite

4.3.2 Microstructure

Figure 4. 15 shows TEM images of the ZnO NPs that were decorated on the rGO sheet. The TEM images show that the ZnO NPs had spherical shapes. The TEM images at different magnifications (1 μm–2 nm) reveal that the ZnO NPs were dispersed on the rGO (Figure 2(a–f)). In addition, these images show that the average particle size was approximately 25 ± 10 nm. The inset of Figure 2(f) shows an HRTEM image of a single nanoparticle. As observed, the nanoparticle is a single crystal with a high crystal quality, and there are no defects from stacking faults. Furthermore, the HRTEM image shows

that the lattice distance is approximately 0.27 nm, which is consistent with the distance along the c-axis of a bulk wurtzite ZnO crystal. Therefore, based on the HRTEM image, the nanoparticles were grown in the [001] direction without any defects. Finally, figure 4. 16 (a, b) shows size histograms of the ZnO NPs below the relative TEM images. These histograms indicate that the main particle sizes of the ZnO NPs calcined at a temperature of 350°C were approximately 25 ± 10 nm. The TEM and size distribution results confirm that a narrow size distribution can be obtained for ZnO NPs prepared in a starch environment and calcined at a temperature of 350°C. Meanwhile, we used the iSolution software to calculate the particle sizes.

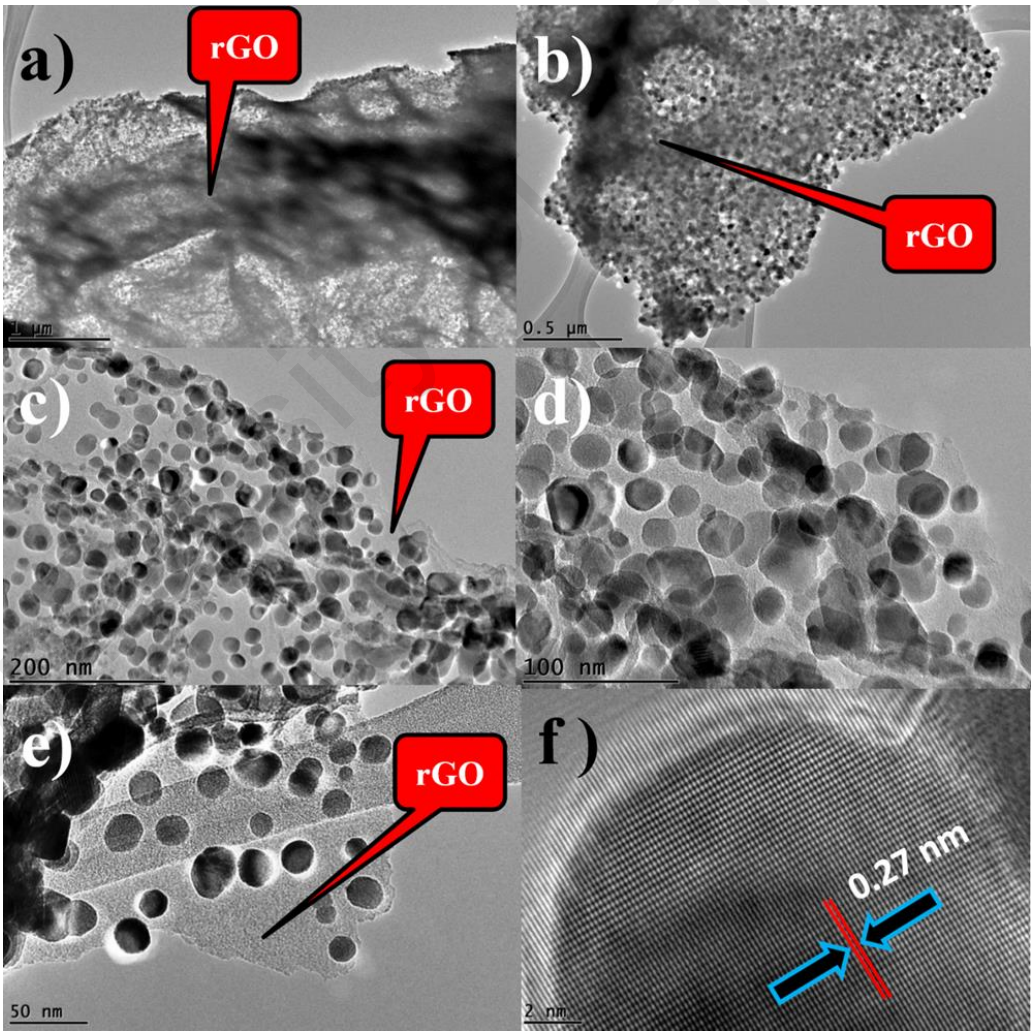

Figure 4.16: TEM images low-magnification; (a), (b) high-magnification; (c) - (e) and (f) HRTEM images of ZnO NPs+rGO

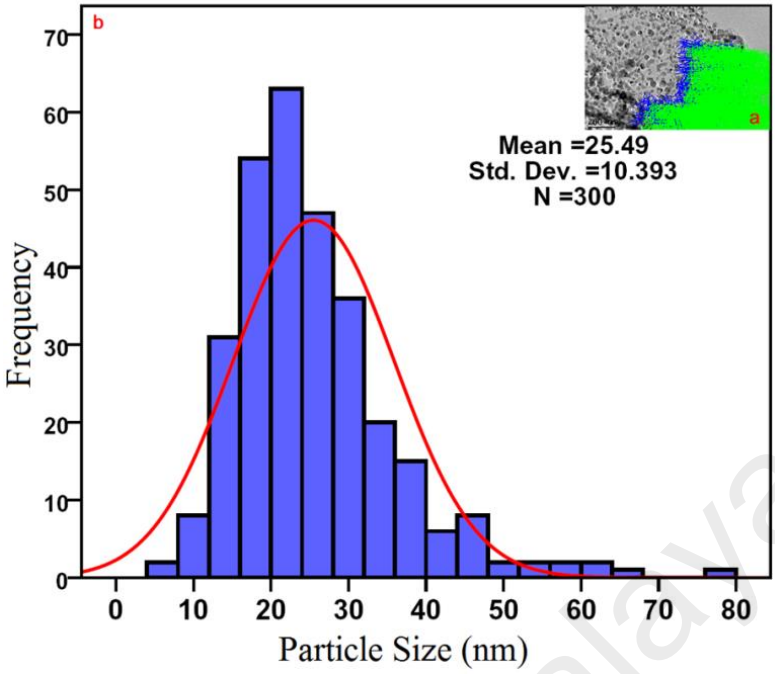

Figure 4.17: Size distribution diagrams of ZnO NPs+rGO by histogram curve

4.3.3 Chemical Composition

Figure 4. 18 shows the FTIR spectra of the pristine GO, starch powder, ZnO NPs, and ZnO NPs + rGO nanocomposites. In the FTIR spectrum of GO, the broad peak centred at 3190 cm^{-1} is attributed to the O–H stretching vibrations, and the peaks at 1731, 1625, 1183, and 1040 cm^{-1} are assigned to the C=O stretching, sp^2-hybridised C=C group, O–H deformation, C–OH stretching, and C–O stretching, respectively (Hummers & Offeman, 1958). In contrast, the peaks at 1731, 1183, and 1040 cm^{-1} are missing from the FTIR spectra of the ZnO NPs+rGO nanocomposites, which indicate the reduction of GO and its transformation to rGO (Peng-Gang, Ding-Xiang, Xu, Tao, Zhong-Ming, 2011; Zou, Zhu, Sun, & Wang, 2011). In addition, the FTIR spectrum of starch powder is shown in Figure 4. 18. The peaks of the starch are dramatically smaller in the FTIR spectra of the ZnO NPs+rGO nanocomposites. In fact, the annealing process at 350°C caused the transformation of GO to rGO and removed the starch,

which is in good agreement with the XRD results. In addition, the FTIR spectrum of the ZnO NPs+rGO shows a peak at 437 cm^{-1}. The band at 437 cm^{-1} corresponds to the E_2 mode of hexagonal ZnO (Raman active) (Jan et al., 2014). Therefore, the resulting nanocomposite consisted of ZnO NPs decorated on an rGO sheet. A weak peak appears at 437 cm^{-1} for the pure ZnO NPs. Therefore, the FTIR results also show that pure ZnO NPs cannot form at 350°C in a starch environment.

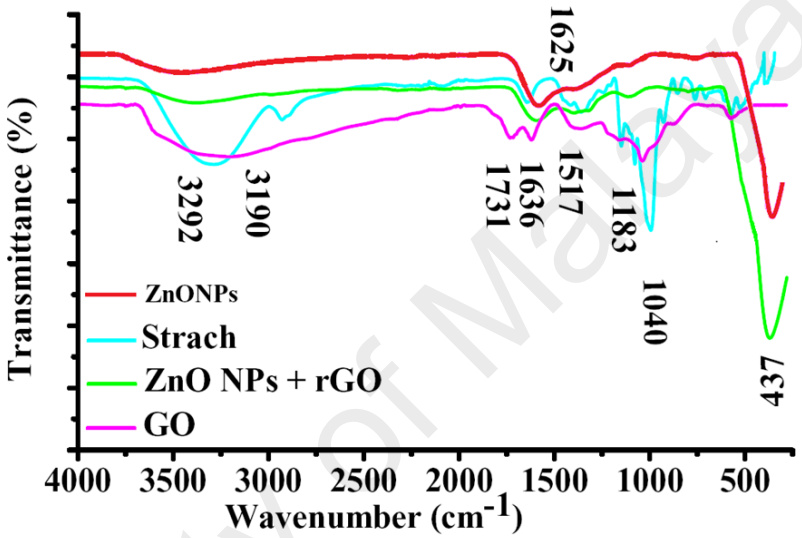

Figure 4.18: FTIR spectra of the GO sheet, starch powder, ZnO NPs, and ZnO NPs+rGO nanocomposites

4.3.4 Optical properties

Figure 4. 19 shows the Raman spectrum of the ZnO NPs+rGO nanocomposite. The graphene obtained from the chemical reduction of GO exhibits two characteristic main peaks: the D band at ~1365 cm^{-1}, which arises from a breathing mode of κ-point photons with A_{1g} symmetry, and the G band at ~1610 cm^{-1}, which arises from the first-order scattering of the E_{2g} mode phonons of the sp^2-bonded carbon atoms (Gao et al., 2010). The D and G band positions and intensity ratios of I(D)/I(G) for the GO and ZnO NPs+rGO composites, prepared using the sol–gel method, are summarised in Table 4. 1.

Table 4.1: D and G peak positions and intensity ratios of I(D)/I(G) (obtained by Raman analysis) of GO and ZnO NPs+rGO composites prepared Sol-gel method

	GO	ZnONPs+rGO
D band (cm^{-1})	1365	1357
G band (cm^{-1})	1610	1600
I(D)/I(G)	0.81	1.13

In comparison to the pristine GO, the Raman spectrum of the ZnO NPs+rGO nanocomposite shows that the D and G bands shifted to lower wave numbers at ~1357 and ~1600 cm^{-1}, respectively, because of the reduction process for the GO, which can be supported by starch as the reducing, capping, and stabilising agent (Liu et al., 2011). In addition to the peaks associated with the D and G bands of graphene, the Raman spectrum of the ZnO NPs+rGO nanocomposite shows a sharp and narrow peak at 437 cm^{-1} corresponding to the E_2 (high) mode of the Raman active mode, a characteristic peak for the wurtzite hexagonal phase of ZnO. The Raman results confirmed that the ZnO NPs+rGO nanocomposite was composed of graphene nanosheets and pure ZnO.

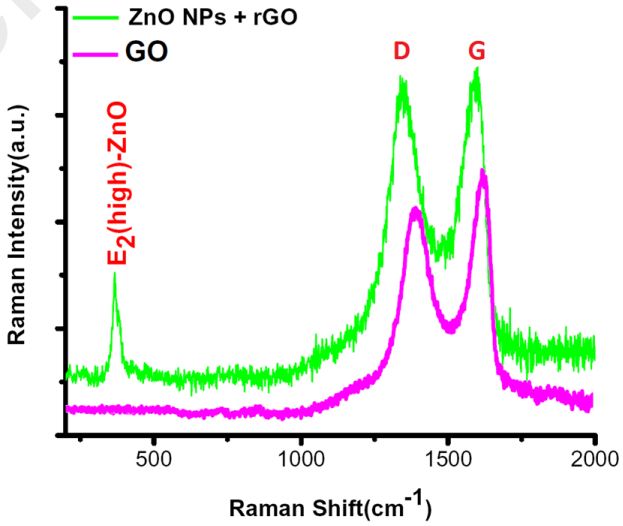

Figure 4.19: Raman spectrum of the ZnO NPs+rGO nanocomposites

The UV–vis absorption spectra of the ZnO NPs and ZnO NPs+rGO at room temperature are shown in Figure 4. 19. These spectra reveal a characteristic absorption peak for ZnO at a wavelength of ~360 nm for ZnO NPs and ~375 nm for the ZnO NPs + rGO samples due to the electron transitions from the valence band to the conduction band ($O_{2p} \rightarrow Zn_{3d}$), which can be assigned to the intrinsic band-gap absorption of ZnO (Yu, Yu, Cheng, & Zhou, 2006). Furthermore, it is observed that the sharp characteristic absorption peak at 365 nm indicates the existence of good crystalline and impurity suppressed ZnO NPs (Lv et al., 2011; Lv, Pan, Liu, & Sun, 2012). As observed, the small redshift (~15 nm) of the absorption edge compared to pure ZnO should be attributed to the chemical bonding between ZnO and rGO, which is similar to the result in the case of ZnO NPs + rGO composite materials (Liu et al., 2012; Lv et al., 2011). However, it is observed that the absorbance of the ZnO NPs+rGO composite increases in comparison to the absorbance of the ZnO NPs. This increase in absorbance may be due to the absorption contribution from rGO, the increase in the surface electric charge of the oxides, and the modification of the fundamental process of electron–hole pair formation during irradiation (Xue et al., 2011). Therefore, the presence of rGO in the ZnO can increase the light absorption, which is beneficial to the photocatalytic performance.

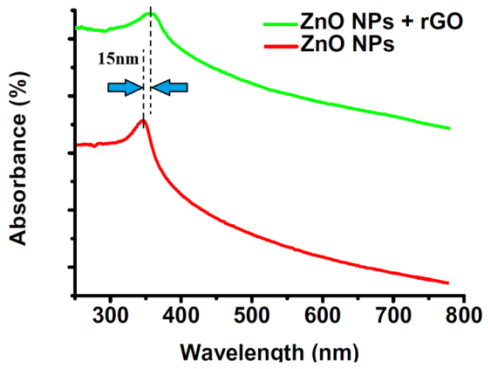

Figure 4.20: UV-vis spectra of the pure ZnO NPs and ZnO NPs+rGO nanocomposites

4.3.5 Photocatalytic measurements

4.3.5.1 MB Degradation

Figure 4. 21 illustrates the optical absorption spectra of the MB aqueous solution with 10 mg of the as-prepared ZnO NPs+rGO composite after exposure to UV-vis light irradiation for different intervals of times. The intensity of the absorption peak of the MB at 663 nm decreases with an increase in the irradiation time, which indicates that the MB molecules are degraded by the catalysis.

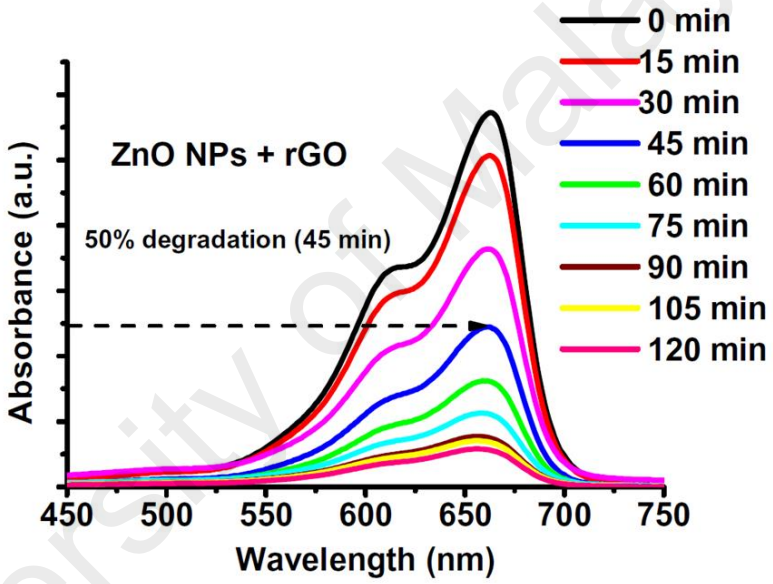

Figure 4.21: The UV-vis absorbance of MB over time during photocatalytic degradation under UV-vis light irradiation using ZnO NPs+rGO

Further experiments were performed to compare the effect of graphene oxide on the catalytic activity of the as-prepared ZnO NPs (sample L), and the results are shown in Figure 4. 22. The samples K and J with concentrations of 0.9 and 3.3 GO (wt.%/v), respectively, and F, which is the same ZnO NPs + rGO with a concentration of 1.7 GO (wt.%/v) of the composite, show significant improvements and higher efficiencies in the photodegradation of MB compared to the pure ZnO NPs. The efficiency for bare ZnO

NPs is 37%, and nearly 63% of the primary dye still remained in the solution for pure ZnO NPs. For the K and J composites over the same time interval as the ZnO NPs, the efficiency has increased to 86% and 88% for sample K and sample J, respectively, and reached a maximum value of 92.5% for ZnO NPs + rGO (sample F) (Table 4. 2).

Table 4.2: Photocatalytic degradation percent of MB on samples

Sample	GO (wt.%/v)	Degradation efficiency (%)
ZnO NPs (Sample L)	0	37%
Sample K	0.9	86%
Sample J	3.3	88%
ZnO NPs+rGO (Sample F)	1.7	92.5%

In general, the degradation efficiency of MB dye was calculated using the following expression:

$$D(\%) = \left[1 - \frac{C_t}{C_0}\right] \times 100 \qquad (1)$$

(Sookhakian, Amin, & Basirun, 2013)

Where C_0 is the absorbance of MB in dark and C_t is the absorbance of MB under light irradiation conditions at time t minutes.

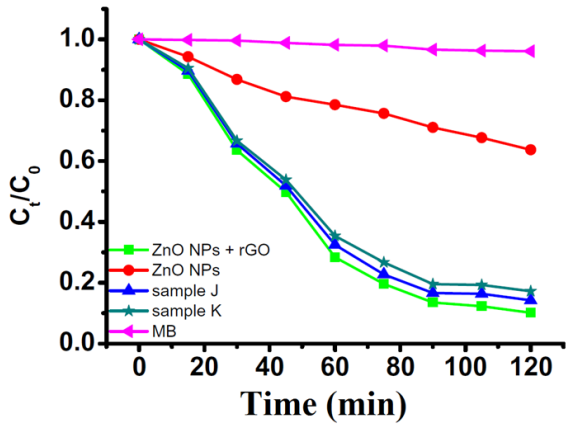

Figure 4.22: Degradation rate of MB at different intervals with and without catalyst

The photocatalytic rate constant for the MB degradation (k) was determined from the first-order plot using the following equation:

$$\ln(\frac{C_0}{C_t}) = kt \qquad (2)\ (\text{Fu et al., 2013})$$

Here, C_0 is the initial absorbance, C_t is the absorbance after time t, and k is the first-order rate constant. Figure 4. 23 shows this plot for the ZnO NPs and ZnO NPs+rGO nanocomposites. The calculated rate constants for the ZnO NPs and ZnO NPs+rGO nanocomposites were 0.011 and 0.023 min^{-1}, respectively.

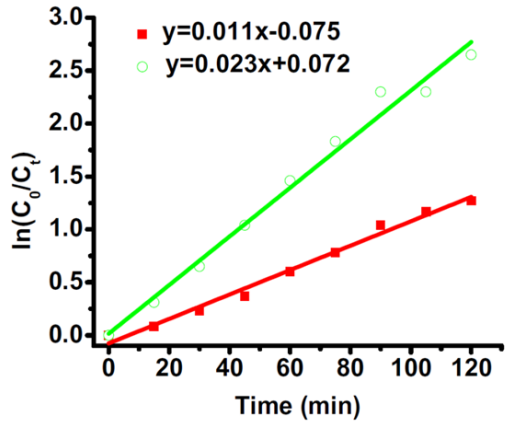

Figure 4.23: Kinetic study of photocatalytic MB degradation using ZnO NPs and ZnO NPs + rGO

The stability test of photocatalytic degradation of MB by ZnO NPs + rGO under UV-vis light irradiation was performed and illustrated in Figure 4. 24. The photocatalytic measurement was performed with five consecutive cycles, each for 120 min. There was no significant decrease in the photodegradation efficiency, indicating perfect reuse and performance of the ZnO NPs + rGO composite.

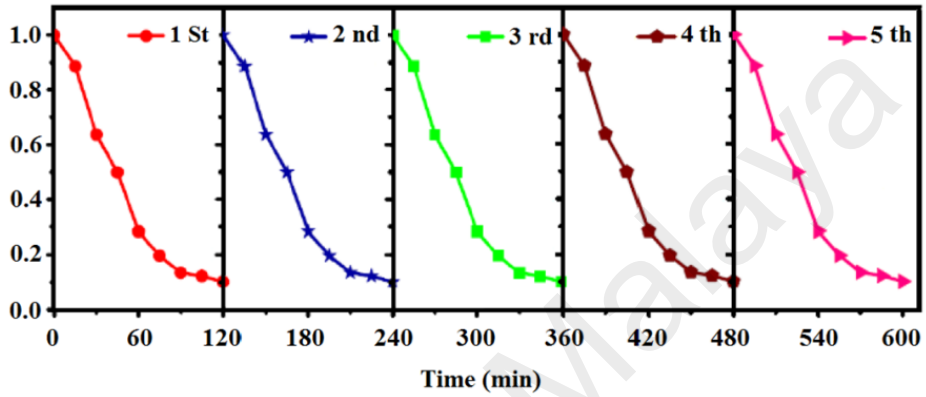

Figure 4.24: Photo-stability of ZnO NPs + rGO by investigating its photocatalytic activity under UV light irradiation with five times of cycling uses

In addition, for stability of the nanocatalyst, the nanocomposites were characterised using XRD and FTIR after five treatments (600 min). These results are shown in Figure 4. 25 (a, b). No difference between these results and the first characterisations that were performed before treatment could be observed. Therefore, it can be understood that the nanocomposites will be stable in crystal structure, phase and chemical composition after photocatalyst treatment, which is beneficial to the photocatalytic performance.

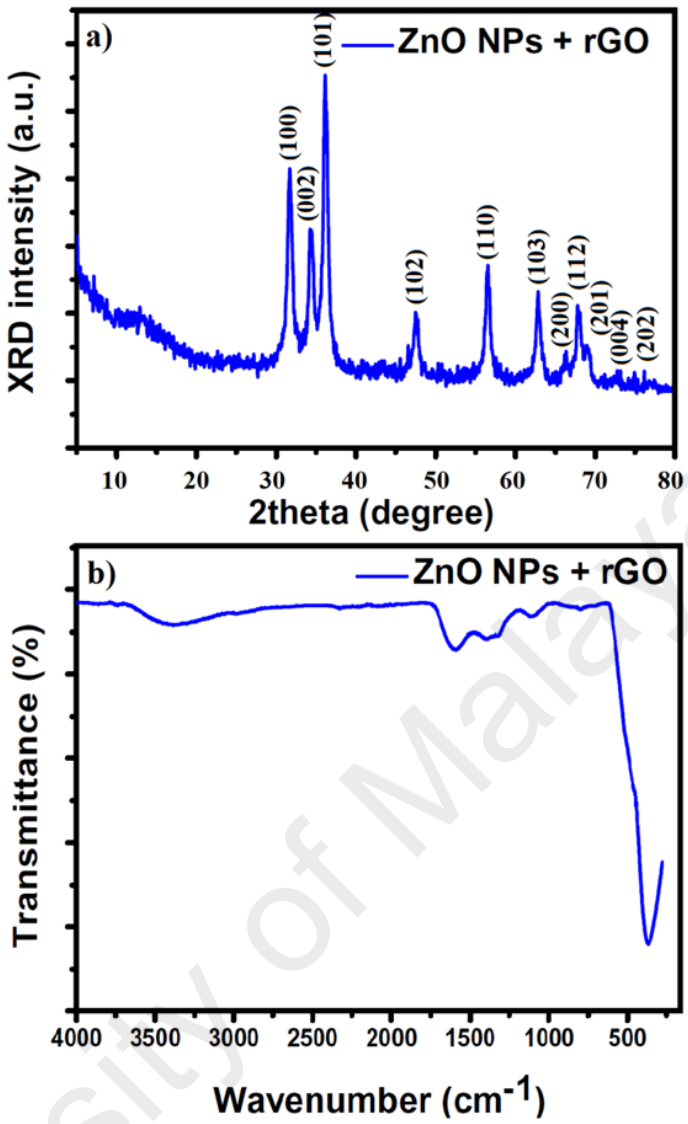

Figure 4.25: XRD pattern (a), FTIR spectra (b) of ZnO NPs + rGO after five cycles

4.3.5.2 Photodegradation Reaction Mechanisms

In addition, Figure 4. 26 shows that the conduction band and valence band for ZnO are −4.05 eV and −7.25 eV (vs. vacuum), respectively (Lv et al., 2012). The work function of rGO is −4.8 eV (Sookhakian et al., 2013).

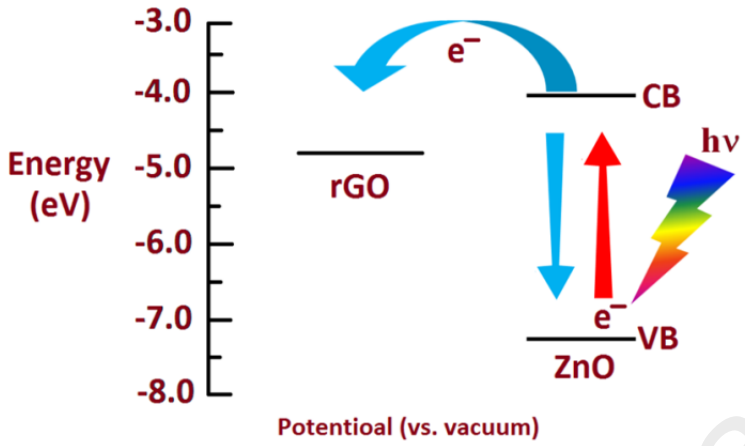

Figure 4.26: The energy level diagram for ZnO NPs+rGO

Therefore, under UV-light irradiation, electron–hole pairs are generated within ZnO, and these photoinduced electrons are easily transferred from the ZnO conduction band to rGO sheet via a percolation mechanism and then scavenged by dissolved oxygen, which causes electron–hole separation. In contrast, the holes can react with either adsorbed water or surface hydroxyls to form hydroxyl radicals. Consequently, the adsorption equilibrium is destroyed, and more MB molecules could move from the solution to the interface and, thus, decompose to CO_2, H_2O, and other minerals via a redox reaction. In general, from the thermodynamic point of view, if the conduction band was more negative than the O_2/O_2^- couples, the photogenerated electrons could reduce O_2 to produce O_2^-. Meanwhile, if the position of the valence band was more positive than the $OH^-/{}^\bullet OH$ couples, the photogenerated holes could oxidize OH^- or H_2O to form ${}^\bullet OH$. Some semiconductors, including TiO_2, ZnO, SnO_2, $SrTiO_3$, $BaTiO_3$ and NiO, corresponded to the case considered above (Grätzel, 2001; Hoffmann, Martin, Choi, & Bahnemann, 1995; Tachikawa, Fujitsuka, & Majima, 2007; Xiang, Yu, & Wong, 2011; Xu et al., 2011; Yu, Yu, Ho, Jiang, & Zhang, 2002). Accordingly, when a

semiconductor is illuminated with photons, electrons in the valance band of the semiconductor are excited into the conduction band, resulting in the generation of electron–hole pairs. These electron–hole pairs either recombine or migrate to the surface of the photocatalyst to initiate a series of photocatalytic reactions and produce hydroxyl radicals, $^{\bullet}OH$ and superoxide radicals, $^{\bullet}O_2^-$ in water, resulting in the degradation of organic pollutants. It has been found that $^{\bullet}OH$ is a major contributor to the photocatalytic degradation of the dye. Therefore, the photodegradation reaction mechanisms of MB under UV- vis light irradiation is summarised by the following equations:

$$ZnO + h\nu \rightarrow ZnO(e^- + h^+) \quad (3)$$

$$e^- + rGO \rightarrow rGO(e^-) \quad (4)$$

$$rGO(e^-) + O_2 \rightarrow rGO + {}^{\bullet}O_2^- \quad (5)$$

$$h^+ + OH^- \rightarrow {}^{\bullet}OH \quad (6)$$

$^{\bullet}OH$ + MB $\rightarrow$ Degradation ($CO_2.H_2O$) (Behnajady, Modirshahla, & Hamzavi, 2006; Xiang et al., 2011; Xu et al., 2011) (7)

Therefore, rGO can effectively improve the charge separation and suppress the recombination of excited carriers, indicating the higher photocatalytic activity of the ZnO NPs+rGO. To further confirm the above assumption, photoluminescence (PL) spectra of the as-prepared samples were investigated as shown in Figure 4. 26. The two typically sharp and broad peaks of pure ZnO nanoparticles can be found at 364 and 538 nm (Weng, Yang, Zhang, & Xu, 2014), corresponding to the near band edge (NBE) emission and deep level emission (DLE), respectively. The NBE emission originates from the recombination of free excitons in the near band edge of the wide band gap ZnO

nanoparticles, and the DLE emission is assigned to various intraband defects in the crystal, such as zinc vacancies, interstitial zinc, oxygen vacancies, interstitial oxygen, and antisite oxygen (Mehran Sookhakian et al., 2014). The UV emission is also called near-band-edge (NBE) emission because of the recombination of free excitons through an exciton–exciton collision process. It has been suggested that the green band emission (deep level emission (DLE)) corresponds to a singly ionised oxygen vacancy in ZnO and results from the recombination of a photogenerated hole with the singly ionised charge state of this defect (Azarang, Shuhaimi, Yousefi, & Sookhakian, 2014). In addition, compared to the pure ZnO nanoparticles and ZnO NPs + rGO, the PL spectra are approximately similar to the pure ZnO but are quenched in the ZnO NPs + rGO. A significant fluorescence quenching of ZnO NPs can be observed after coupling ZnO NPs with rGO due to the interactions of the ZnO NPs surfaces with rGO, which illustrates that the electron-hole pairs in the excited ZnO NPs could be efficiently separated, and efficient transfer of photoinduced electrons between ZnO NPs and rGO could occur. In fact, the large surface area of the rGO causes the ZnO NPs to disperse. Therefore, the dispersed NPs absorb light and generate more electron–hole pairs to remove dye molecules.

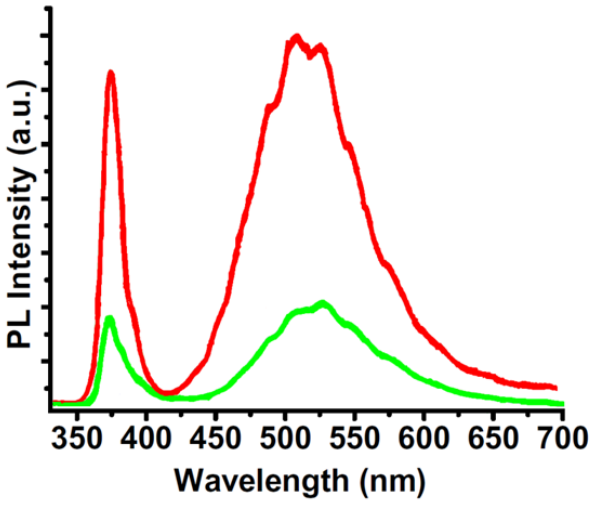

Figure 4.27: PL spectra of the pure ZnO NPs, ZnO NPs + rGO

4.4 Crystalline quality assessment, photocurrent response and optical properties of reduced graphene oxide uniformly decorated zinc oxide nanoparticles based on graphene oxide concentration

In this study, Zinc oxide-nanoparticles (ZnONPs)-reduced graphene oxide (rGO) composites with a high degree of crystallinity and a high dispersity were successfully synthesized via a one-pot, facile sol-gel method in a starch environment, during which the formation of zinc oxide nanoparticles, the reduction of graphene oxide and the loading of ZnONPs onto the rGO surface occur simultaneously. Starch, as a natural capping agent, plays a significant role in controlling the degree of dispersion and coverage of ZnONPs. The effect of rGO on the crystalline structure and optical properties of ZnONPs was determined via X-ray diffraction, UV–visible diffused reflectance spectroscopy and photoluminescence spectroscopy. The ZnONPs+rGO composites exhibit excellent potential for photocurrent generation compared with pure ZnONPs under visible light irradiation, provided that efficient photo-induced charge separation and transportation can be achieved at the interface. The maximum photocurrent response, crystalline quality and factor optical properties (NBE/DLE ratio) were obtained for the ZnONPs+rGO2 composite with a 1.7% mass fraction of rGO, which is twice that achieved on pure ZnONPs.

4.4.1 Microstructure

Figure 4. 28(a–c) shows TEM images of the ZnONPs+rGO composites with different concentrations (0.9, 1.7 and 3.3 wt.%/v GO) for the rGO sheets. The TEM images reveal that the ZnONPs are decorated and dispersed on the rGO sheets. However, this dispersion is less for ZnONPs+rGO1 than for the other samples. Figure 4.

28(c) shows that the ZnONP population in ZnONPs+rGO3 is less than that in the other samples. This result explains why the XRD peak intensities decreased with an increase in the GO concentration. In addition, the size histograms of the ZnONPs+rGO are shown Figures 4. 28(a-c). The histograms show that the main particle sizes of the ZnONPs+rGO1, ZnONPs+rGO2 and ZnONPs+rGO3 with different concentrations for the rGO sheets (0.9, 1.7 and 3.3 wt.%/v) were 22±14, 20±6, and 25±10 nm, respectively. Figures 4. 28(d-f) shows HRTEM images of single nanoparticles from sheets with different GO concentrations. These HRTEM images show that the concentration of the rGO sheet affects the crystalline quality of the NPs. It can be observed that there are several areas of damage and defects for the zinc oxide nanoparticles, which were grown on the sheets with the low and high concentrations of GO Figures 4. 28(d) and 4. 28(f). On the other hand, the crystalline space of the ZnONPs+rGO2 composite is clear and shows a non-defective structure for the nanoparticle Figure 4. 28(e). In fact, the HRTEM results are in good agreement with the XRD results. In addition, the HRTEM image of the ZnONPs+rGO2 composite shows that the lattice distance is approximately 0.26 nm Figure 4. 28, which is consistent with the distance along the c-axis of a bulk wurtzite ZnO crystal. Therefore, based on the HRTEM image, the nanoparticles were grown along the [001] direction without any defects.

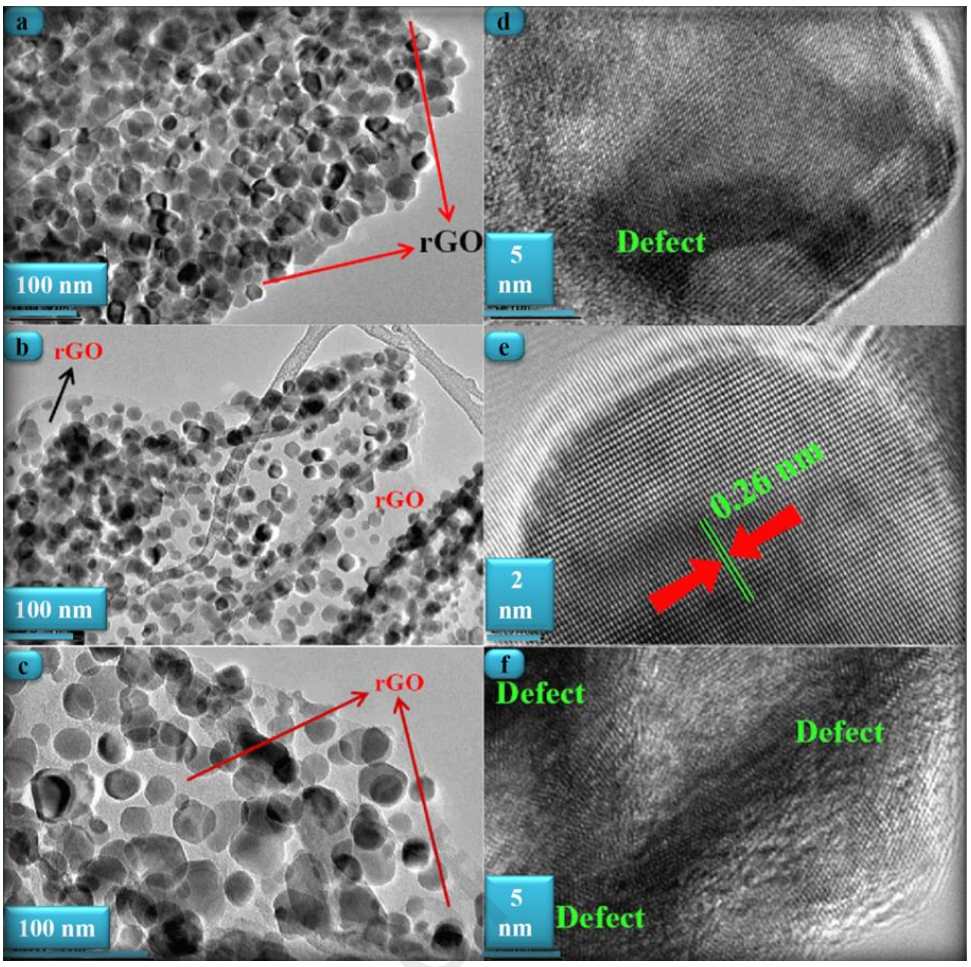

Figure 4.28: TEM image of the ZnONPs+rGO composites with a (a) low rGO concentration ZnONPs+rGO1, (b) mid rGO concentration ZnONPs+rGO2, and (c) high rGO concentration ZnONPs+rGO3. The HRTEM image of the ZnONPs that were decorated on the rGO sheet with a (d) low rGO concentration, (e) mid rGO concentration, and (f) high rGO concentration

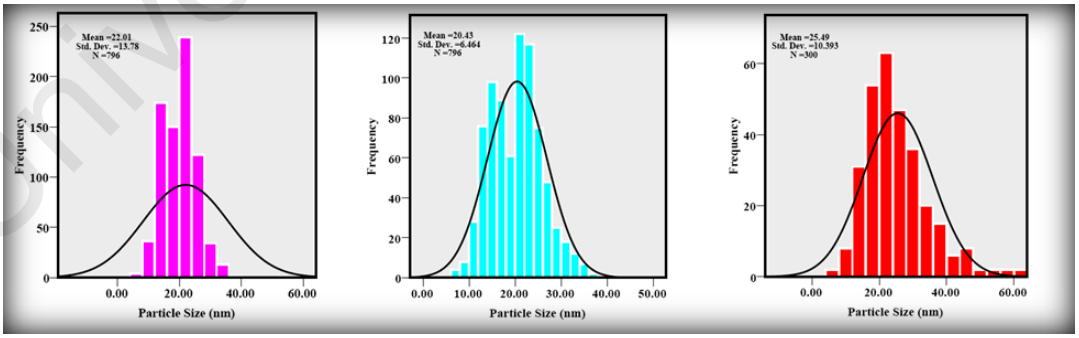

Figure 4.29: Size distribution diagrams of (a) ZnONPs+rGO1, (b) ZnONPs+rGO2, and (c) ZnONPs+rGO3 composites by histogram curve

To further investigate the influence of starch and rGO on the nanoparticle distribution on the samples, FESEM analyses of pure ZnONPs and ZnONPs+rGO(1, 2

and 3) composites with different concentrations for the rGO sheets (0.9, 1.7 and 3.3 wt.%/v) were performed (Figures 4. 30(a, b)). As observed in Figure 4. 30(a), zinc oxide nanoparticles agglomerate in the absence of starch. The FESEM image of pure ZnONPs (Figure 4. 30(a)) clearly shows that the particles agglomerate due to the large surface to volume ratio of nanoparticles. Because of their strong surface reactivity, most nanoparticles undergo agglomeration. To overcome this challenge, starch has been used to obtain a narrower particle size distribution and also to control the particle size of the final product. Therefore, to investigate the effect of starch as a natural surfactant, the FESEM images of the as-synthesized ZnONPs are shown in Figure 4. 30(b). As observed in Figure 4. 30(b), the presence of starch significantly affects the size distribution of the nanoparticles, and starch as a natural capping agent is able to separate the nanoparticles and prevent their agglomeration.

However, when the rGO is added to the system, the ZnONPs covered the surface of the rGO uniformly, and a good loading of the ZnONPs on the rGO nanosheets occurred (Figures 4. 28(a-c)). Moreover, as observed in Figures 4. 28(a-c), the surface of the rGO thin film is clearly visible, while the typical wrinkle-like features are barely visible. A more careful and close-up view reveals that the individual ZnONPs with sizes in the range of 22–25 nm is well separated from each other and are well distributed on the graphene sheets, i.e., no large areas of the graphene sheets without ZnO decoration are found. Moreover, the partially enlarged image in Figure 4. 28(b) clearly illustrates that there is no apparent aggregation of the ZnONPs on the graphene sheets; in addition, the rGO nanosheets can function as conductive bands for the interconnection between the various ZnONPs and the transfer of photogenerated charge carriers to enhance the transient photocurrent. Based on these results, the possible mechanism of growth can be predicted. The positively charged Zn^{2+} ions attached onto the surface of the graphene oxide due to its negative charge. The initial nucleation of ZnONPs was formed during

the sol-gel process due to the reaction of the adsorbed Zn^{2+} onto GO via the O^{2-} ions. An in situ charge transfer process occurred between ZnO nuclei and graphene oxide to produce rGO. However, starch, as a natural polymerization agent, acts as terminator for the growth of ZnONPs. Starch was expended during the calcined process in 350 °C to prevent the nanoparticles from agglomerating.

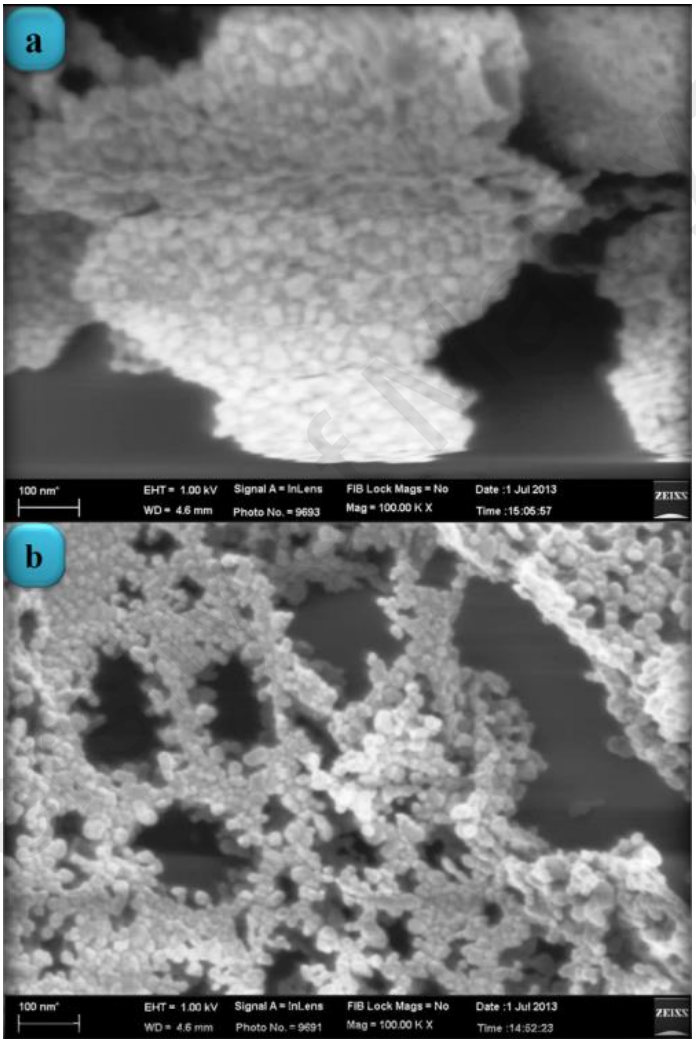

Figure 4.30: (a) FESEM image of pure ZnONPs in the absence of starch (sample M). (b) FESEM image of pure ZnONPs in the presence of starch (sample K)

4.4.2 Crystalline structure

Figure 4. 31 shows the X-ray diffractogram of graphite, GO and rGO. An intense and sharp diffraction peak for GO appears at 2θ = 10.6°, which is attributed to the (001) lattice plane with the interlayer spacing of 0.83 nm, which is consistent with the lamellar structure of GO. This spacing is much wider than that of the graphite narrow peak located at 26.8°, which has an interlayer spacing of 0.33 nm. This result indicates that GO sheets have been effectively exfoliated from the raw graphite (Sookhakian et al., 2015; Zhang, Zhang, Tang, & Xu, 2012). As a comparison, after the sol-gel process of the pure GO without the presence of ZnONPs, the diffractogram illustrates the disappearance of this strong peak along with the appearance of a very broad (002) peak and a very weak (100) peak at 2θ of 24.32° and 42.55°, respectively; the peaks at 24.32° and 42.55° correspond to interlayer spacing's of 0.36 nm and 0.21 nm, respectively (Sookhakian et al., 2015). This result indicates that the GO was reduced to rGO during the sol-gel process due to the removal of the functional groups (Sookhakian et al., 2015).

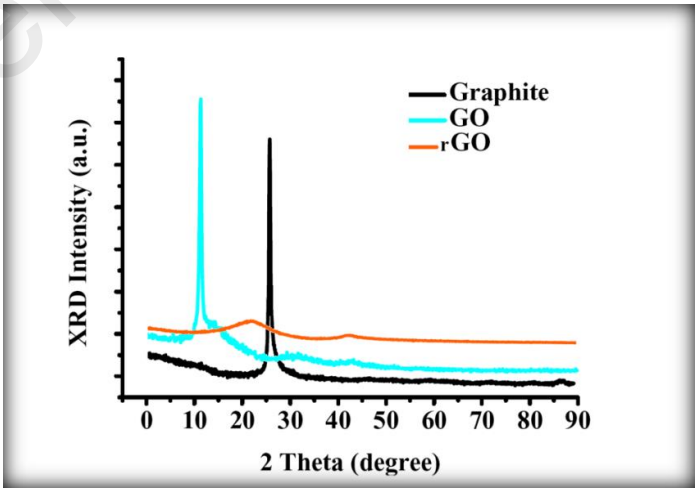

Figure 4.31: XRD patterns of graphite, GO and rGO sheets

The phase structures of the ZnONPs+rGO composites with the different mass fractions of rGO in the presence of starch are illustrated in Figure 4. 32. It is evident that

all of the samples exhibit similar XRD patterns to blank ZnO, i.e., the existence of rGO does not affect the growth of new crystal orientations of ZnO; thus, rGO only functions as a platform where the ZnONPs can nucleate and grow. The peaks located at 2θ values of 32.09°, 34.53°, 36.91°, 48.43°, 57.22°, 63.13°, and 68.47°, which can be indexed to the (100), (002), (101), (102), (110), (103), and (200) lattice planes, respectively, of the ZnO wurtzite structure (JCPDS card no. 00-036-1451) with the lattice constant a = b = 0.3218 nm, c = 0.5330 nm. Furthermore, compared with the pure ZnONPs, the high intensity diffraction peak of ZnONPs+rGO composites with different mass fraction of rGO at 34.53° is broadened slightly, which is attributed to slight reduction of the crystalline size of the ZnONPs in the composite in the presence of rGO.

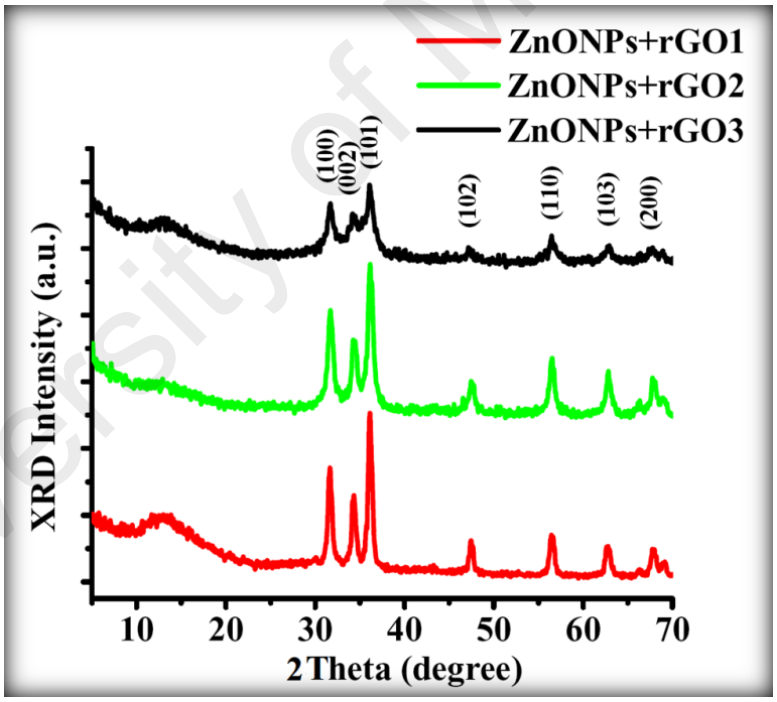

Figure 4.32: XRD patterns of the ZnONPs+rGO composites with low rGO concentration (ZnONPs+rGO1), min rGO concentration (ZnONPs+rGO2), and high rGO concentration (ZnONPs+rGO3)

From the Scherrer equation (1), the estimated crystallite sizes of ZnONPs in the absence of rGO and in the presence of rGO with different mass ratios were calculated

(Table 4. 3). Notably, no typical diffraction peaks of rGO are observed in the ZnONPs+rGO composites, which might be due to the low diffraction intensity peak and small amount of rGO (Azarang, Shuhaimi, Yousefi, & Sookhakian, 2014).

$$D = \frac{\kappa\lambda}{\beta_{hkl}\cos\theta} \quad (1)$$

where D is the crystallite size in nanometres, λ is the wavelength of the radiation (1.54056 A^o for CuKα radiation), k is a constant equal to 0.94, β_{hkl} is the peak width at half-maximum intensity (FWHM) and θ is the peak position (Holzwarth & Gibson, 2011).

Table 4.3: Peak position and calculated the crystallite size of the pure ZnONPs and ZnONPs+rGO composite with low rGO concentration ZnONPs+rGO1, mid rGO concentration ZnONPs+rGO2, and high rGO concentration ZnONPs+rGO3

Sample code	2θ (^{o})	FWHM (^{o})	Crystallite size (nm)
ZnONPs (Sample K)	34.3282	0.2528	25.07656
ZnONPs+rGO1(Sample J)	34.3842	0.3801	22.03493
ZnONPs+rGO2 (Sample E)	34.3894	0.3936	21.01845
ZnONPs+rGO3(Sample I)	34.3956	0.3992	20.03745

To better understand the effects of the rGO sheets on the growth process for the ZnONPs, zinc oxide nanoparticles were synthesized without graphene at 400 and 500 °C. The XRD patterns of these conditions are shown in Figure 4. 32. It can be observed

that the XRD pattern of the NPs that were sintered at 400 °C indicates a low crystalline quality. On the other hand, the XRD pattern of the NPs that were sintered at 500 °C indicates a good crystalline quality.

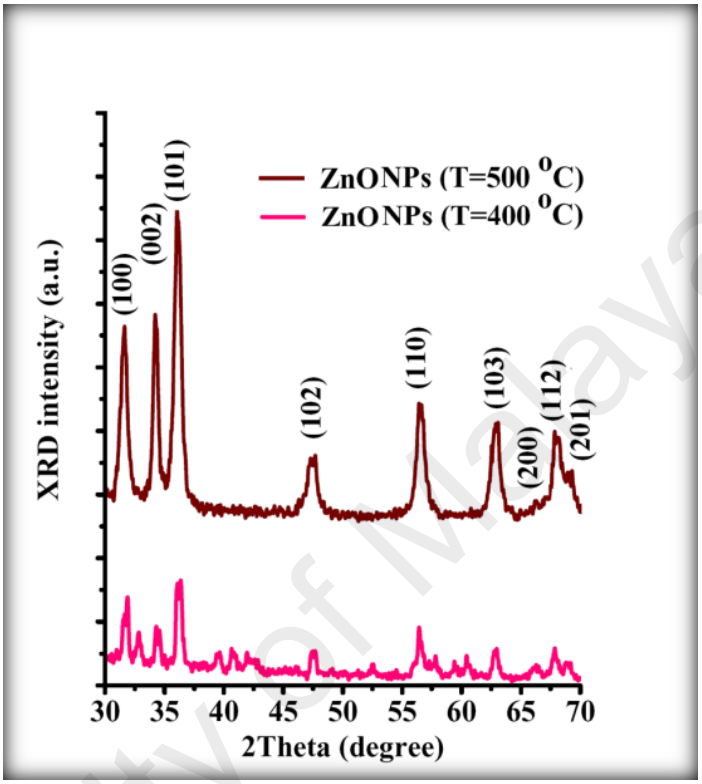

Figure 4.33: XRD patterns of the pure ZnONPs that were grown by 400 and 500 °C temperature sample N and sample P, respectively

In addition, the TEM images for NPs sintered under these conditions confirm the XRD results (Figures 4. 33(a, b)). Furthermore, these TEM images show that the NPs were not very well dispersed without the rGO sheet. According to the obtained results, it can be concluded that the rGO sheets not only play a role as a dispersion site for the NPs but also play a role as a useful site to grow the ZnONPs. In fact, the rGO sheets could decrease the calcination temperature. The widely accepted mechanism for the synthesis of graphene decorated with inorganic nanostructures is the attraction of positively charged metal ions by the polarized bonds of the functional groups on the

GO. The attachment of these metal ions to the surface and edges of the GO results in a redox reaction and the formation of nucleation sites, which eventually leads to the growth of nanostructures on the 2-D graphene sheets (Xue et al., 2011).

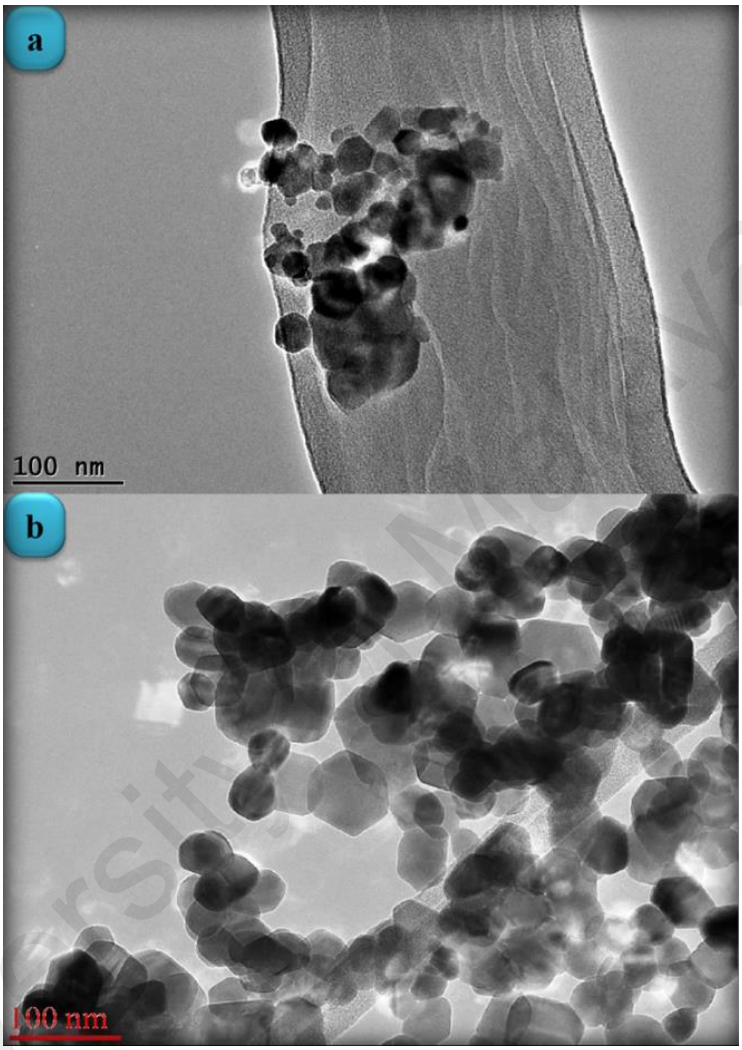

Figure 4.34: TEM image of the pure ZnONPs that were grown at (a) 400 °C and (b) 500 °C

4.4.3 Chemical Composition

Figure 4. 35 shows the FTIR spectra of the pristine GO, starch powder, ZnONPs+rGO1, ZnONPs+rGO2, and ZnONPs+rGO3 composites. In the FTIR spectrum of GO, the broad peak centred at 3190 cm^{-1} is attributed to the O–H stretching vibrations, and the peaks at 1731, 1625, 1183, and 1040 cm^{-1} are assigned to the C=O

stretching, sp^2-hybridized C=C group, O–H deformation, C–OH stretching, and C–O stretching, respectively (Hummers & Offeman, 1958). In contrast, the peaks at 1731, 1183, and 1040 cm^{-1} are missing from the FTIR spectra of the ZnONPs+$rGO_{(1,\ 2\ and\ 3)}$ composites, which indicate the reduction of GO and its transformation to rGO (Peng-Gang et al., 2011; W. Zou et al., 2011). In addition, the FTIR spectrum of starch powder is shown in Figure. 10. The peaks of the starch are dramatically smaller in the FTIR spectra of the ZnONPs+$rGO_{(1,\ 2\ and\ 3)}$ composites. In fact, the annealing process at 350°C caused the transformation of GO to rGO and removed the starch, which is in good agreement with the XRD results. In addition, the FTIR spectrum of the ZnONPs+$rGO_{(1,\ 2\ and\ 3)}$ shows a peak at 437 cm^{-1}. The band at 437 cm^{-1} corresponds to the E_2 mode of hexagonal ZnO (Raman active) (Jan et al., 2014). Therefore, the resulting composite consisted of ZnONPs decorated on an rGO sheet. A weak peak appears at 437 cm^{-1} for the pure ZnONPs. Therefore, the FTIR results also show that pure ZnONPs cannot form at 350°C in a starch environment.

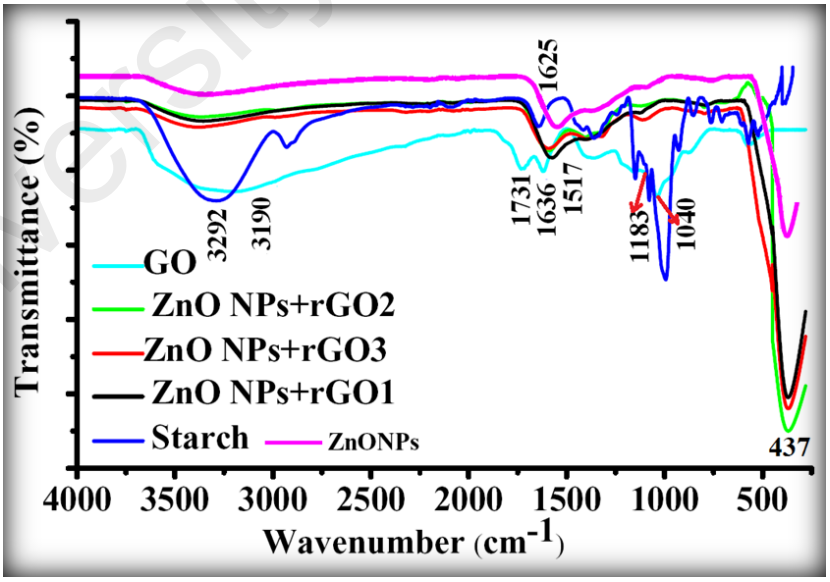

Figure 4.35: FTIR spectra of the GO sheet, starch powder, and ZnONPs+rGO1, ZnONPs+rGO2, and ZnONPs+rGO3 composites

4.4.4 Optical properties

Figure 4. 35 shows the Raman spectrum of the ZnONPs+rGO2 composite. The graphene obtained from the chemical reduction of GO exhibits two characteristic main peaks: the D band at ~1365 cm^{-1}, which arises from a breathing mode of κ-point photons with A_{1g} symmetry, and the G band at ~1610 cm^{-1}, which arises from the first-order scattering of the E_{2g} mode phonons of the sp^2-bonded carbon atoms (Gao et al., 2010; Stankovich et al., 2007). The D and G band positions and intensity ratios of I(D)/I(G) for the GO and ZnONPs+rGO2 composites prepared using the sol–gel method are summarized in Table 4. 4. In comparison to the pristine GO, the Raman spectrum of the ZnONPs+rGO2 composite shows that the D and G bands shifted to lower wave numbers at ~1357 and ~1600 cm^{-1}, respectively, because of the reduction process for the GO, which can be supported by starch as the reducing, capping, and stabilizing agent (Liu et al., 2011). In addition to the peaks associated with the D and G bands of graphene, the Raman spectrum of the ZnONPs+rGO2 composite shows a sharp and narrow peak at 437 cm^{-1} corresponding to the E_2 (high) mode of the Raman active mode, a characteristic peak for the wurtzite hexagonal phase of ZnO. The Raman results confirmed that the ZnONPs+rGO2 composite was composed of graphene nanosheets and pure ZnO.

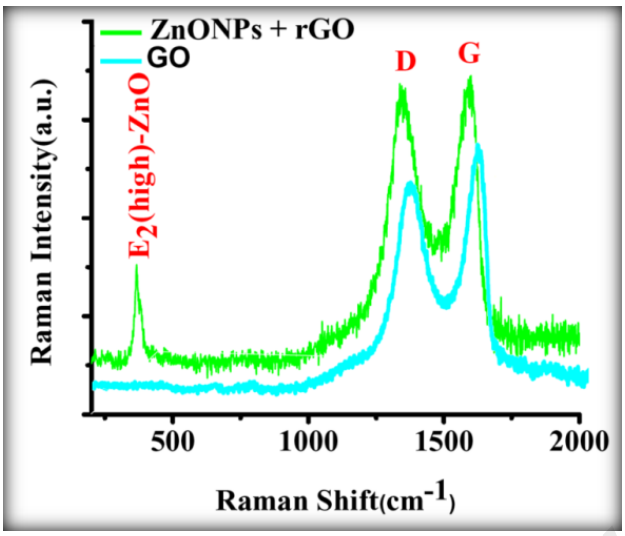

Figure 4.36: Raman spectrum of the GO and ZnONPs+rGO composites

Table 4.4: D and G peak positions and intensity ratios of I(D)/I(G) (obtained by Raman analysis) of GO and ZnONPs+rGO composites prepared sol-gel method by starch

	GO	ZnONPs+rGO
D band (cm^{-1})	1365	1357
G band (cm^{-1})	1610	1600
I(D)/I(G)	0.81	1.13

The room temperature UV-Vis absorption spectra of ZnONPs+(rGOX)$_{X=0,\ 1,\ 2,\ 3}$ are shown in Figure 4. 37. The ZnONPs+(rGOX) $_{X=0,\ 1,\ 2,\ 3}$ composites were dispersed in ethanol with a concentration of 0.1% wt and then the solution was used to perform the UV-Vis measurement. The UV–Vis absorption spectra of the ZnONPs and ZnONPs+rGO at room temperature are shown in Figure 4. 36. These spectra reveal a characteristic absorption peak for different composites at a wavelength of ~360, ~365, ~369, ~374 nm for ZnONPs, ZnONPs+rGO1, ZnONPs+rGO2 and ZnONPs+rGO3

samples due to the electron transitions from the valence band to the conduction band ($O_{2p} \rightarrow Zn_{3d}$), which can be assigned to the intrinsic band-gap absorption of ZnO (Yu et al., 2006). Furthermore, it is observed that the sharp characteristic absorption peak at 365 nm indicates the existence of good crystalline and impurity-suppressed ZnONPs (Lv et al., 2011; Lv et al., 2012), and it was proposed that the Zn-O-C bond between ZnO and rGO was formed, which is in good agreement with the FTIR and Raman results. Similar phenomena were also observed for RGO/ZnO composites prepared by Zhang et al (Zhang, Chen, Liu, & Xu, 2013), confirming what we proposed in this paper. As observed, the small redshifts (~5, ~4, and ~5 nm) of the absorption edge compared to pure ZnO should be attributed to the chemical bonding between ZnO and rGO, which is similar to the result in the case of the ZnONPs+rGO composite materials (Liu et al., 2012; Lv et al., 2011). However, it is observed that the absorbance of the ZnONPs+rGO(1, 2 and 3) composites increases in comparison to the absorbance of the ZnONPs. This increase in absorbance may be due to the absorption contribution from rGO, the increase in the surface electric charge of the oxides, and the modification of the fundamental process of electron–hole pair formation during irradiation (Xue et al., 2011). Therefore, the presence of rGO in the ZnO can increase the light absorption, which is beneficial to the optoelectronic performance. From the plot curve $\frac{dA}{dE}$, which is the first derivative of energy absorption with respect to energy, the estimated band gap energies of ZnONPs in the absence of rGO and in the presence of rGO with different mass ratio were calculated Figure 4. 38 (Zak, Razali, Majid, & Darroudi, 2011). The band gap value of ZnONPs was calculated using ultraviolet–visible (UV–Vis) spectroscopy and decreased with increased rGO concenteration.

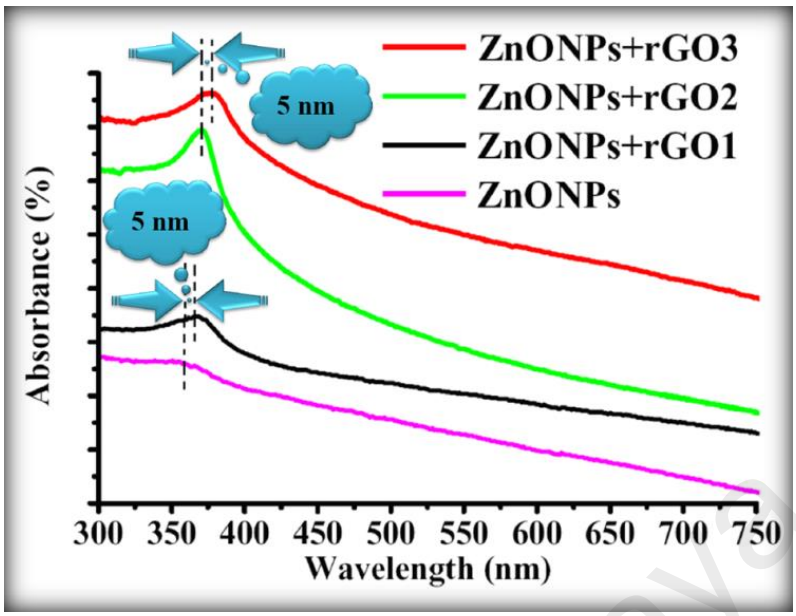

Figure 4.37: UV-Vis spectra of the pure ZnONPs, ZnONPs+rGO1, ZnONPs+rGO2, and ZnONPs+rGO3 composites

Eventually, the optical absorption edge of the ZnONPs shifts to a slightly higher wavelength with the increase in the ratio of rGO in the ZnONPs+rGO composites. Therefore, these results indicate that although the band gap of ZnONPs very slightly decreases in the presence of rGO, as shown in Figure 4. 37, the band gap narrowing of all the ZnONPs+rGO hybrids was clearly observed. Furthermore, the hybrids containing higher concentrations of rGO show a narrower band gap, indicating that the interaction between the ZnO nanoparticles and the rGO sheets enhances with an increase the concentration of rGO. These results support that the preparation of ZnONPs+rGO with a sol-gel process with starch is successful (Cheng et al., 2013).

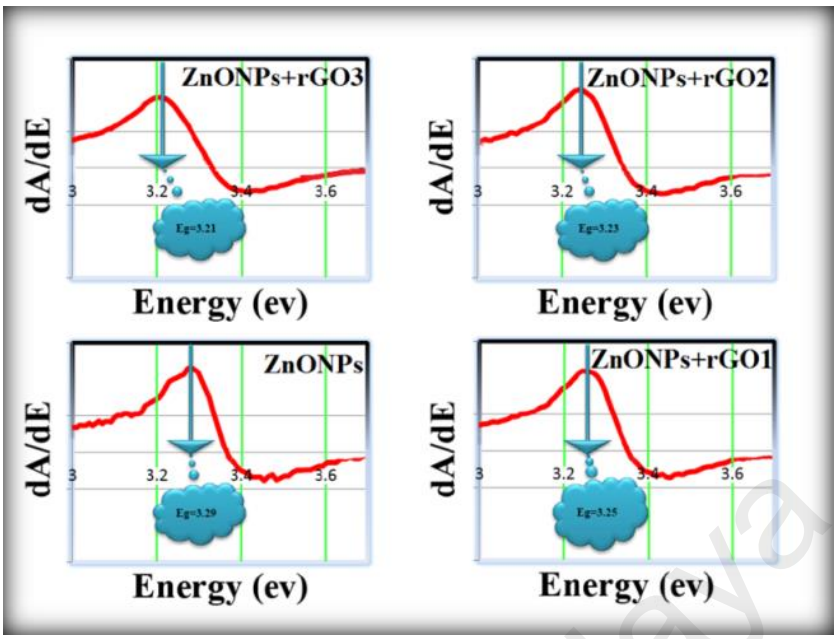

Figure 4.38: The band gap of the ZnONPs, ZnONPs+rGO1, ZnONPs+rGO2, and ZnONPs+rGO3 composites estimated from first derivative

Figure 4. 39 shows the photoluminescence (PL) spectra of the products. A significant difference can be seen between the PL spectrum of the pure ZnONPs, which were grown at 350 °C, and that of the ZnONPs+rGO composites. To further confirm the above assumption, PL spectra of the as-prepared samples were investigated as shown in Figure 4. 39. The two typically sharp and broad peaks of pure ZnO nanoparticles can be found at ~364 and ~538 nm(Weng et al., 2014), corresponding to the near band edge (NBE) emission and deep level emission (DLE), respectively. The NBE emission originates from the recombination of free excitons in the near band edge of the wide band gap ZnO nanoparticles, and the DLE emission is assigned to various intraband defects in the crystal, such as zinc vacancies, interstitial zinc, oxygen vacancies, interstitial oxygen, and antisite oxygen (Sadollahkhani et al., 2014). The UV emission is also called near band edge (NBE) emission because of the recombination of free excitons through an exciton–exciton collision process. It has been suggested that the green band emission DLE corresponds to a singly ionized oxygen vacancy in ZnO and

results from the recombination of a photogenerated hole with the singly ionized charge state of this defect. Therefore, Figure 4. 39 shows that the ZnONPs have very high concentrations of oxygen vacancies. However, the intensity of the UV peak is increased and that of the visible peak is decreasing with an increasing the graphene concentration. However, the NBE/DLE ratio of the ZnONPs+rGO2, which is one of the main factors that is usually used for comparing the optical properties of samples, is bigger than the NBE/DLE ratios of the other composites. Therefore, the ZnONPs+rGO2 composites have a better relative crystalline quality. According to these results, it can be understood that the graphene concentration has an optimum value in relation to improving the optical quality of the ZnONPs. In fact, the optical study results are in good agreement with the XRD and TEM results. Therefore, the ZnONPs+rGO2 composite is the best composite of ZnO and rGO for improving the crystalline and optical quality of the ZnONPs, which were sintered at a lower temperature than is normally used to grow pure ZnONPs by the sol–gel method in a starch environment.

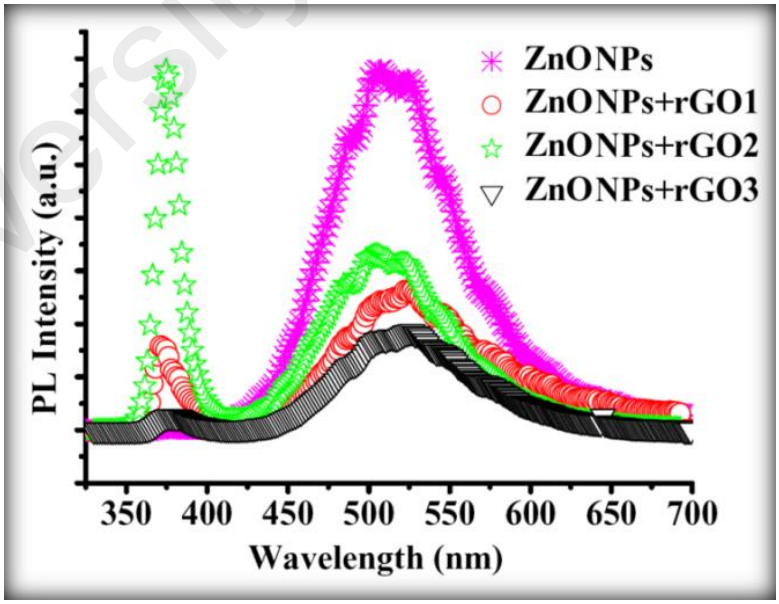

Figure 4.39: PL spectra of the pure ZnONPs, ZnONPs+rGO1, ZnONPs+rGO2, and ZnONPs+rGO3 composites

4.4.5 Studies of the photocurrent response

4.4.5.1 Transient photocurrent response of ZnONPs and ZnONPs+rGO films

A schematic of the solar cell device fabricated using the ZnONPs+rGO modified ITO electrode is illustrated in Figure 4. 40. To investigate the influence of rGO on the photoelectrochemical properties of the fabricated solar cell devices, the transient photocurrent response was measured under visible light irradiation. The transient photocurrents of pure ZnONPs-, ZnONPs+rGO1-, ZnONPs+rGO2-, and ZnONPs+rGO3-modified ITO electrodes irradiated with visible light are illustrated in Figure 4. 39. The applied bias was 0 V vs. an SCE reference electrode.

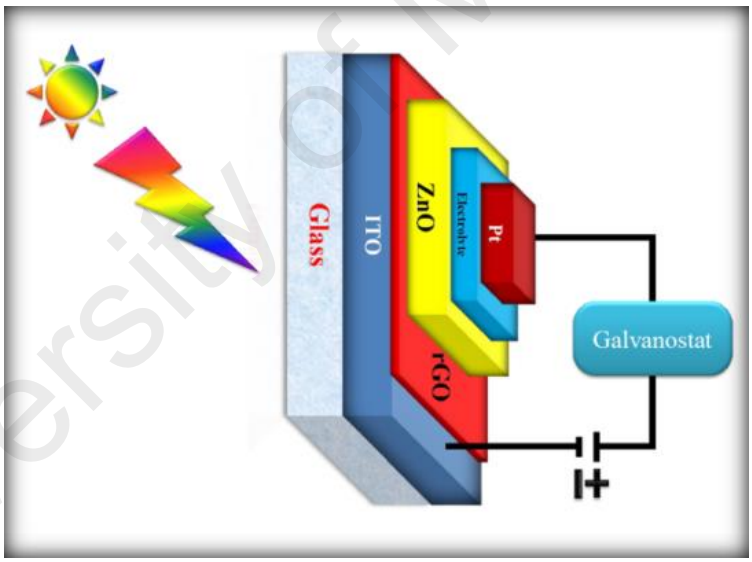

Figure 4.40: Schematic representation of the solar cell device

As observed in Figure 4. 41, a small anodic photocurrent density of 0.85 μA/cm^2 was obtained for pure ZnONPs when the light source was switched on. Moreover, the dark current was ~0.1 nA/cm2 when the light source was switched off. However, the presence of rGO leads to the enhancement of transient photocurrent response of pure

ZnO from 0.85 μA/cm^2 to 1.22 μA/cm^2 for ZnONPs+rGO1. However, with the increase in the rGO concentration up to 1.7 wt.%/v, the transient photocurrent initially increases from 1.22 μA/cm^2 to 1.9 μA/cm^2 for both ZnONPs+rGO1 and ZnONPs+rGO2. A further increase in the rGO concentration up to 3.3 wt.% leads to a decrease in transient photocurrent from 1.9 μA/cm^2 to 1.17 μA/cm^2. The optimized value is obtained from ZnONPs+rGO2 (based on ZnONPs+rGO (1.7 wt.%/v)), under visible light irradiation (100 mWcm^{-2}), which is approximately 4-fold higher than that of the pure ZnONP electrode. Moreover, the transient photocurrents were rapid, steady, prompt and reproducible during several on–off cycles of the visible light irradiation for all samples as well; no overshoots were observed at the beginning and the end of the flash. The rectangular response indicates that no grain boundaries exist in the direction of electron diffusion. The grain boundaries create deep traps to slow the electron transport and may exist at the particulate electrode (Devika, Reddy, & Tu, 2015). This finding also suggests that the excited electrons are collected efficiently in the external circuit (Devika et al., 2015).

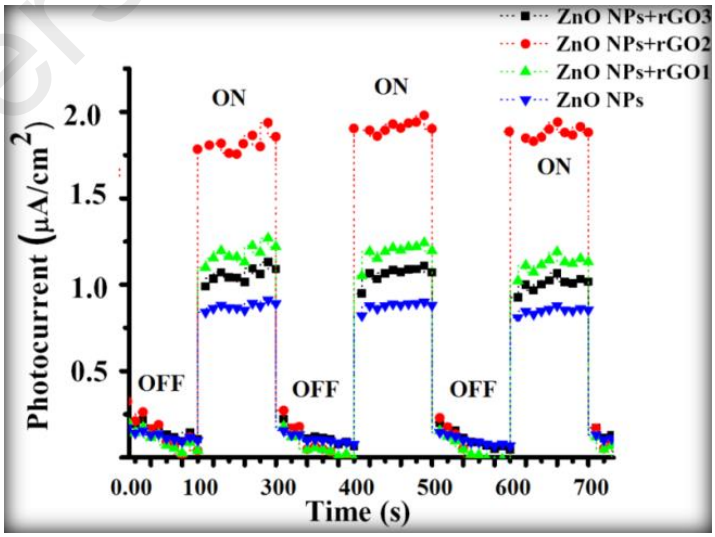

Figure 4.41: Photocurrent versus time (i–t) curves of the solar cell device based on pure ZnO and ZnONPs+rGO composite with different concentration ratios of GO (0.9, 1.7 and 3.3 wt.%/v)

To better understand the effects of the factors of crystalline quality and optical properties (NBE/DLE ratio) on the photocurrent for the ZnONPs, zinc oxide nanoparticles were synthesized without graphene oxide and in the presence of graphene oxide as shown in Table 4. 5. It can be observed that they have direct contact with each other.

Table 4.5: Near band edge (NBE), deep level emission (DLE) ratio and photocurrent of the pure ZnONPs and ZnONPs+rGO composite with low rGO concentration ZnONPs+rGO1, mid rGO concentration ZnONPs+rGO2, and high rGO concentration ZnONPs+rGO3

Sample code	NBE	DLE	NBE /DLE	Photocurrent ($\mu A/cm^2$)
ZnONPs (Sample K)	147.95	6441.84	0.0229	0.85
ZnONPs+rGO1(Sample J)	1589.81	2596.86	0.6122	1.22
ZnONPs+rGO3(Sample I)	247.31	1851.78	0.1335	1.17
ZnONPs+rGO2(Sample E)	6790.51	3307.86	2.0528	1.9

4.4.5.2 Mechanism

Figure 4. 41 shows the possible mechanism of photocurrent generation on ZnONPs+rGO composites under the visible light irradiation. As observed in the figure, the main reason for the enhancement of the photocurrent response of the ZnONPs+rGO composites is related to the stepwise structure of the energy levels constructed in the composite, which causes enhanced charge separation. As observed in Figure 4. 41, the conduction band and valence band for ZnONPs are −4.05 eV and −7.25 eV (vs. vacuum), respectively, and the work function of rGO is −4.8 eV (Azarang, Shuhaimi, Yousefi, & Jahromi, 2015). Therefore, ZnONPs absorb visible light to produce electron–hole pairs. These photo-induced electrons are easily transferred from the ZnO conduction band to the rGO sheets and then to the ITO substrate via a percolation

mechanism; the electrons are finally scavenged by the I^-/I_3^- pair in the electrolyte. Therefore, based on the UV–Vis and PL results, it is clear that the enhanced photocurrent in ZnONPs+rGO composites is related to rGO; these composites not only extend the photoresponse range of solar spectrum to the visible light range but also improve the interfacial electron transfer and constrain the electron–hole pair recombination of ZnONPs in ZnONPs+rGO composites. Moreover, the effect of the rGO content in the improvement of transient photocurrent plays an important role. The transient photocurrent of the ZnONPs+rGO composites decreased when the rGO content was increased beyond the optimum value. This phenomenon can be attributed to the following: (i) rGO may absorb some visible light and thus cause a light harvesting competition between ZnO and rGO with the increase in the rGO content, which leads to the decrease in the transient photocurrent, and (ii) excessive rGO can act as a centre for the recombination of electron–hole pairs instead of providing an electron pathway, as observed in the PL results in Figure 14 (Azarang et al., 2015).

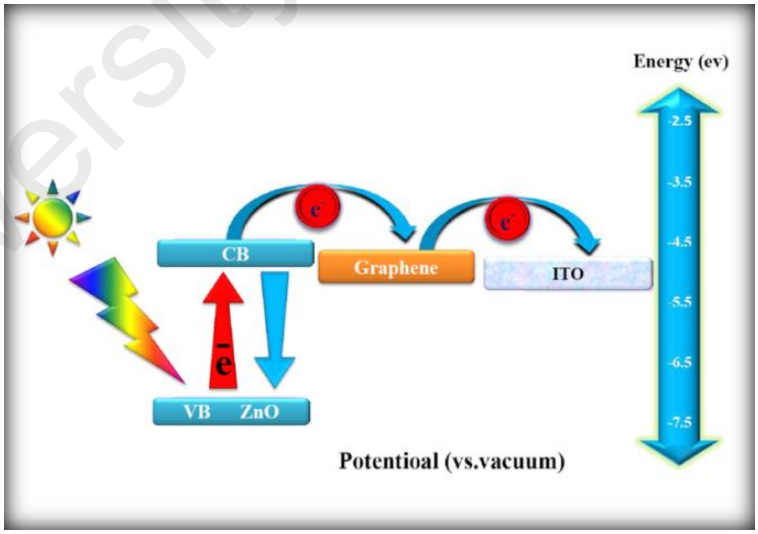

Figure 4.42: Schematic of the mechanism of the photocurrent generation

CHAPTER 5: CONCLUSIONS

5.1 Synthesis and characterization of ZnO NPs/reduced graphene oxide nanocomposite prepared in gelatin medium as highly efficient photo-degradation of MB

ZnO-NPs/RGO was synthesized by the sol–gel method in a gelatin medium. FESEM and TEM images showed that the ZnO NPs were decorated and dispersed on the RGO. An HRTEM image of the NPs revealed that the ZnO NPs were single crystals without any defects. The XRD pattern of the ZnO-NPs/RGO indicated a hexagonal phase for the obtained product. The FTIR results showed that the post-annealing process removed the gelatin medium and formed the ZnO structure. In addition, the FTIR showed that the GO was transformed into RGO by the post-annealing process. The photocatalyst activity revealed the high MB removal efficienc of the ZnO-NPs/RGO in comparison to the ZnO NPs. This method can be used for the large-scale removal of pollutants from wastewater.

5.2 Effects of graphene oxide concentration on optical properties of ZnO/RGO nanocomposites and their application to photocurrent generation

ZnO/RGO nanocomposites with different concentrations of RGO were successfully grown using a sol–gel method. The XRD patterns and TEM images indicated that the RGO could increase the crystalline quality of the ZnO NPs that were decorated on the RGO sheets. In addition, a comparison between the growth processes for the ZnO NPs that were decorated on the RGO and pure ZnO NPs showed that the RGO could decrease the calcination temperature for the ZnO NP growth. In addition, the RGO could be a good site to disperse the ZnO NPs. Furthermore, the optical properties of the ZnO NPs were increased by the RGO. However, the results showed that there was an optimum RGO concentration for increasing the optical properties of the ZnO NPs. Finally, the photocurrent results for the obtained products showed that the RGO

increased the current density of the ZnO NPs. However, this study also revealed that there was an optimum concentration for increasing the current density of the ZnO NPs.

5.3 One-pot sol–gel synthesis of reduced graphene oxide uniformly decorated zinc oxide nanoparticles in starch environment for highly efficient photodegradation of Methylene Blue

ZnO NPs+rGO were synthesized using the sol–gel method in a starch environment. TEM images showed that the ZnO NPs were decorated and dispersed on the rGO. An HRTEM image of the NPs revealed that the ZnO NPs were single crystals without any defects. The XRD pattern of the ZnO NPs+rGO indicated a hexagonal phase of the product obtained. The FTIR results showed that the annealing process removed the starch environment and formed the ZnO structure. In addition, the FTIR showed that the GO was transformed into rGO by the annealing process in a starch environment. The photocatalyst activity showed the high MB removal efficiency of the ZnO NPs+rGO in comparison to the ZnO NPs. This method can be used for the large-scale removal of pollutants from wastewater. Generally, it was established that the reduced graphene oxide sheets played important roles in enhancing the photocatalytic efficiency of the ZnO NPs + rGO nanocomposite compared to the bare ZnO NPs: 1) the prevention of ZnO NPs + rGO agglomeration, leading to the growth of small nanoparticles on the surfaces, 2) the increasing adsorption of MB molecules, and 3) the suppression of electron‑hole recombination.

5.4 Crystalline quality assessment, photocurrent response and optical properties of reduced graphene oxide uniformly decorated zinc oxide nanoparticles based on graphene oxide concentration

A ZnONPs+rGO composite with a diameter of 20±6 nm was successfully synthesized using a simple one-pot sol-gel method with the assistance of starch as a

capping agent. The FTIR and Raman results clearly show the reduction of graphene oxide in the composite to reduced graphene oxide. The transient photocurrent results show that (i) ZnONPs+rGO composites enable significant improvement in the transient photocurrent under visible light irradiation compared to pure ZnO, due to the increase in the light absorption in the visible region, the decrease in the charge recombination, and the increase in charge transport; (ii) the transient photocurrent of ZnONPs+rGO composite is dependent on the weight percentage of the reduced graphene oxide in the composite and the ZnONPs+rGO composite, with 1.7 wt.%/v rGO corresponding to a maximum transient photocurrent of 1.9 μA/cm^2 and a maximum crystalline quality for ZnONPs+rGO2. Furthermore, for a better understanding of the conclusions on the effect of the GO concentration on the crystalline quality and factor optical properties (NBE/DLE ratio), the photocurrent, crystallite size and FWHM for the ZnONPs+rGO composite are shown in Figures 51(a-d).

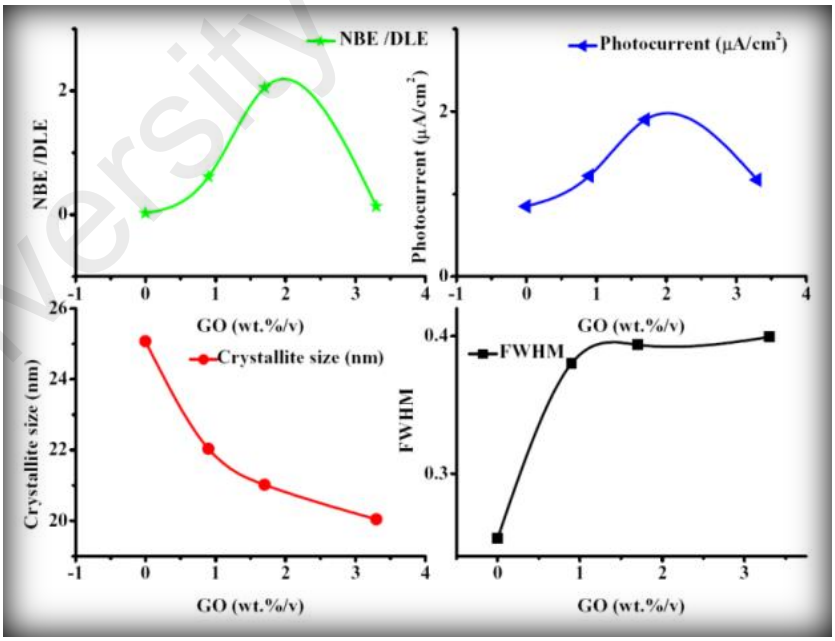

Figure 5.1: The (a) NBE/DLE, (b) photocurrent, (c) crystallite size, and (d) FWHM versus GO concentration as final conclusions

REFERENCES

Azarang, M., Shuhaimi, A., Yousefi, R., & Jahromi, S. P. (2015). One-pot sol–gel synthesis of reduced graphene oxide uniformly decorated zinc oxide nanoparticles in starch environment for highly efficient photodegradation of Methylene Blue. *RSC Advances., 5(28), 21888-21896.*

Azarang, M., Shuhaimi, A., Yousefi, R., Moradi Golsheikh, A., & Sookhakian, M. (2014). Synthesis and characterization of ZnO NPs/reduced graphene oxide nanocomposite prepared in gelatin medium as highly efficient photo-degradation of MB. *Ceramics International, 40(7), 10217-10221.*

Azarang, M., Shuhaimi, A., Yousefi, R., & Sookhakian, M. (2014). Effects of graphene oxide concentration on optical properties of ZnO/RGO nanocomposites and their application to photocurrent generation. *Journal of Applied Physics, 116(8), 084307.*

Bai, S., & Shen, X. P. (2012). Graphene-inorganic nanocomposites. *RSC Advances, 2(1), 64-98.*

Barpuzary, D., & Qureshi, M. (2013). Enhanced photovoltaic performance of semiconductor-sensitized zno-cds coupled with graphene oxide as a novel photoactive material. *ACS Applied Materials and Interfaces, 5(22), 11673-11682.*

Beek, W. J., Wienk, M. M., Kemerink, M., Yang, X., & Janssen, R. A. (2005). Hybrid zinc oxide conjugated polymer bulk heterojunction solar cells. *The Journal of Physical Chemistry B, 109(19), 9505-9516.*

Behnajady, M., Modirshahla, N., & Hamzavi, R. (2006). Kinetic study on photocatalytic degradation of CI Acid Yellow 23 by ZnO photocatalyst. *Journal of hazardous materials, 133(1), 226-232.*

Boruah, P. K., Borah, D. J., Handique, J., Sharma, P., Sengupta, P., & Das, M. R. (2015). Facile synthesis and characterization of Fe3O4 nanopowder and Fe3O4/reduced graphene oxide nanocomposite for methyl blue adsorption: A comparative study. *Journal of Environmental Chemical Engineering, 3(3), 1974-1985.*

Cao, H., Li, B., Zhang, J., Lian, F., Kong, X., & Qu, M. (2012). Synthesis and superior anode performance of TiO 2@ reduced graphene oxide nanocomposites for lithium ion batteries. *Journal of Materials Chemistry, 22(19), 9759-9766.*

Chang, K., & Chen, W. (2011). l-Cysteine-Assisted Synthesis of Layered MoS2/Graphene Composites with Excellent Electrochemical Performances for Lithium Ion Batteries. *ACS Nano, 5(6), 4720-4728.*

Chang, Y. M., Kim, H., Lee, J. H., & Song, Y.-W. (2010). Multilayered graphene efficiently formed by mechanical exfoliation for nonlinear saturable absorbers in fiber mode-locked lasers. *Applied Physics Letters, 97(21), 211102.*

Chauke, V. P., Maity, A., & Chetty, A. (2015). High-performance towards removal of toxic hexavalent chromium from aqueous solution using graphene oxide-alpha cyclodextrin-polypyrrole nanocomposites. *Journal of Molecular Liquids, 211, 71-77.*

Chen, S., Zhu, J., Wu, X., Han, Q., & Wang, X. (2010). Graphene Oxide−MnO2 Nanocomposites for Supercapacitors. *ACS Nano, 4(5), 2822-2830.*

Cheng, G., Akhtar, M. S., Yang, O.-B., & Stadler, F. J. (2013). Novel preparation of anatase TiO2@ reduced graphene oxide hybrids for high-performance dye-sensitized solar cells. *ACS Applied Materials & Interfaces, 5(14), 6635-6642.*

Cheng, Z., Li, Q., Li, Z., Zhou, Q., & Fang, Y. (2010). Suspended Graphene Sensors with Improved Signal and Reduced Noise. *Nano Letters, 10(5), 1864-1868.*

Choi, J., Reddy, D. A., Islam, M. J., Seo, B., Joo, S. H., & Kim, T. K. (2015). Green synthesis of the reduced graphene oxide–CuI quasi-shell–core nanocomposite: A highly efficient and stable solar-light-induced catalyst for organic dye degradation in water. *Applied Surface Science, 358, Part A, 159-167.*

Devika, M., Reddy, N. K., & Tu, C. W. (2015). ZnO/ITO core/shell nanostructure electrodes for future prototype solar cell devices. *RSC Advances, 5(4), 2891-2899.*

Ding, G., Xie, S., Liu, Y., Wang, L., & Xu, F. (2015). Graphene oxide-silver nanocomposite as SERS substrate for dye detection: Effects of silver loading amount and composite dosage. *Applied Surface Science, 345, 310-318.*

Ding, Y., Jiang, Y., Xu, F., Yin, J., Ren, H., Zhuo, Q., Zhang, P. (2010). Preparation of nano-structured LiFePO4/graphene composites by co-precipitation method. *Electrochemistry Communications, 12(1), 10-13.*

Dong, L., Li, M., Dong, L., Zhao, M., Feng, J., Han, Y., Sun, X. (2014). Hydrothermal synthesis of mixed crystal phases TiO2–reduced graphene oxide nanocomposites with small particle size for lithium ion batteries. *International Journal of Hydrogen Energy, 39(28), 16116-16122.*

Dong, S., Dou, X., Mohan, D., Pittman Jr, C. U., & Luo, J. (2015). Synthesis of graphene oxide/schwertmannite nanocomposites and their application in Sb(V) adsorption from water. *Chemical Engineering Journal, 270, 205-214.*

Drelich, J., Chibowski, E., Meng, D. D., & Terpilowski, K. (2011). Hydrophilic and superhydrophilic surfaces and materials. *Soft Matter, 7(21), 9804-9828.*

Dreyer, D. R., Park, S., Bielawski, C. W., & Ruoff, R. S. (2010). The chemistry of graphene oxide. *Chemical Society Reviews, 39(1), 228-240.*

Du, X., Zhang, Z., Miao, Z., Ma, M., Zhang, Y., Zhang, C., Chen, Q. (2015). One step electrodeposition of dendritic gold nanostructures on β-lactoglobulin-functionalized reduced graphene oxide for glucose sensing. *Talanta, 144, 823-829*

Erickson, K., Erni, R., Lee, Z., Alem, N., Gannett, W., & Zettl, A. (2010). Determination of the Local Chemical Structure of Graphene Oxide and Reduced Graphene Oxide. *Advanced Materials, 22(40), 4467-4472.*

Feng, Y., Feng, N., & Du, G. (2013). A green reduction of graphene oxide via starch-based materials. *RSC Advances, 3(44), 21466.*

Ferrari, A. C., Bonaccorso, F., Falko, V., Novoselov, K. S., Roche, S., Boggild, P., Kinaret, J. (2014). Science and technology roadmap for graphene, related two-dimensional crystals, and hybrid systems. *Nanoscale.*

Fowler, J. D., Allen, M. J., Tung, V. C., Yang, Y., Kaner, R. B., & Weiller, B. H. (2009). Practical Chemical Sensors from Chemically Derived Graphene. *ACS Nano, 3(2), 301-306.*

Freitag, M. (2008). Graphene: Nanoelectronics goes flat out. *Nat Nano, 3(8), 455-457.*

Fu, D., Han, G., Yang, F., Zhang, T., Chang, Y., & Liu, F. (2013). Seed-mediated synthesis and the photo-degradation activity of ZnO–graphene hybrids excluding the influence of dye adsorption. *Applied Surface Science, 283(0), 654-659.*

Fu, X. W., Liao, Z. M., Zhou, Y. B., Wu, H. C., Bie, Y. Q., Xu, J., & Yu, D. P. (2012). Graphene/ZnO nanowire/graphene vertical structure based fast-response ultraviolet photodetector. *Applied Physics Letters, 100(22).*

Gao, J., Liu, F., Liu, Y., Ma, N., Wang, Z., & Zhang, X. (2010). Environment-Friendly Method To Produce Graphene That Employs Vitamin C and Amino Acid. *Chemistry of Materials, 22(7), 2213-2218.*

Gao, P., Li, A., Sun, D. D., & Ng, W. J. (2014). Effects of various TiO2 nanostructures and graphene oxide on photocatalytic activity of TiO2. *Journal of hazardous materials, 279, 96-104.*

Gao, T., Gong, L.-j., Wang, Z., Yang, Z.-k., Pan, W., He, L., Xu, W. (2015). Boron nitride/reduced graphene oxide nanocomposites as supercapacitors electrodes. *Materials Letters, 159, 54-57.*

Gao, Y., Hu, M., & Mi, B. (2014). Membrane surface modification with TiO2–graphene oxide for enhanced photocatalytic performance. *Journal of Membrane Science, 455, 349-356.*

Geim, A. K. (2009). Graphene: status and prospects. *Science, 324(5934), 1530-1534.*

Ghavami, M., Mohammadi, R., Koohi, M., & Kassaee, M. Z. (2014). Visible light photocatalytic activity of reduced graphene oxide synergistically enhanced by successive inclusion of γ-Fe2O3, TiO2, and Ag nanoparticles. *Materials Science in Semiconductor Processing, 26, 69-78.*

Gómez-Navarro, C., Weitz, R. T., Bittner, A. M., Scolari, M., Mews, A., Burghard, M., & Kern, K. (2007). Electronic transport properties of individual chemically reduced graphene oxide sheets. *Nano Letters, 7(11), 3499-3503.*

Grätzel, M. (2001). Photoelectrochemical cells. *Nature, 414(6861), 338-344.*

Gui, D., Liu, C., Chen, F., & Liu, J. (2014). Preparation of polyaniline/graphene oxide nanocomposite for the application of supercapacitor. *Applied Surface Science, 307, 172-177.*

Gui, Y., Zhao, J., Wang, W., Tian, J., & Zhao, M. (2015). Synthesis of hemispherical WO3/graphene nanocomposite by a microwave-assisted hydrothermal method and the gas-sensing properties to triethylamine. *Materials Letters, 155, 4-7.*

Gupta, V. K., Eren, T., Atar, N., Yola, M. L., Parlak, C., & Karimi-Maleh, H. (2015). CoFe2O4@TiO2 decorated reduced graphene oxide nanocomposite for photocatalytic degradation of chlorpyrifos. *Journal of Molecular Liquids, 208, 122-129.*

Hao, Y., Wang, Z., Gou, J., & Dong, S. Highly efficient adsorption and removal of Chrysoidine Y from aqueous solution by magnetic graphene oxide nanocomposite. *Arabian Journal of Chemistry.*

He, H. Y. (2015). Photoinduced superhydrophilicity and high photocatalytic activity of ZnO–reduced graphene oxide nanocomposite films for self-cleaning applications. *Materials Science in Semiconductor Processing, 31, 200-208.*

Hoffmann, M. R., Martin, S. T., Choi, W., & Bahnemann, D. W. (1995). Environmental applications of semiconductor photocatalysis. *Chemical Reviews, 95(1), 69-96.*

Holzwarth, U., & Gibson, N. (2011). The Scherrer equation versus the'Debye-Scherrer equation'. *Nature Nanotechnology, 6(9), 534-534.*

Hu, C., Lu, T., Chen, F., & Zhang, R. (2013). A brief review of graphene–metal oxide composites synthesis and applications in photocatalysis. *Journal of the Chinese Advanced Materials Society, 1(1), 21-39.*

Hu, F. X., Xie, J. L., Bao, S. J., Yu, L., & Li, C. M. (2015). Shape-controlled ceria-reduced graphene oxide nanocomposites toward high-sensitive in situ detection of nitric oxide. *Biosensors and Bioelectronics, 70, 310-317.*

Hu, L., Sun, Y., Zhang, F., & Chen, Q. (2013). Facile synthesis of porous Mn2O3 hierarchical microspheres for lithium battery anode with improved lithium storage properties. *Journal of Alloys and Compounds, 576, 86-92.*

Hu, Z., & Liu, H. (2015). Three-dimensional CuO microflowers as anode materials for Li-ion batteries. *Ceramics International, 41(6), 8257-8260.*

Huang, K., Li, Y. H., Lin, S., Liang, C., Wang, H., Ye, C. X., Lei, M. (2014). A facile route to reduced graphene oxide–zinc oxide nanorod composites with enhanced photocatalytic activity. *Powder Technology, 257, 113-119.*

Huang, X., Qi, X., Boey, F., & Zhang, H. (2012). Graphene-based composites. *Chemical Society Reviews, 41(2), 666-686.*

Huang, X., Yin, Z., Wu, S., Qi, X., He, Q., Zhang, Q., Zhang, H. (2011). Graphene-based materials: synthesis, characterization, properties, and applications. *Small, 7(14), 1876-1902.*

Huang, X., Yin, Z., Wu, S., Qi, X., He, Q., Zhang, Q., Zhang, H. (2011). Graphene-Based Materials: Synthesis, Characterization, Properties, and Applications. *Small, 7(14), 1876-1902.*

Hummers Jr, W. S., & Offeman, R. E. (1958). Preparation of graphitic oxide. *Journal of the American Chemical Society, 80(6), 1339.*

Hummers, W. S., & Offeman, R. E. (1958). Preparation of Graphitic Oxide. *Journal of the American Chemical Society, 80(6), 1339-1339.*

Ikhsan, N. I., Rameshkumar, P., Pandikumar, A., Mehmood Shahid, M., Huang, N. M., Vijay Kumar, S., & Lim, H. N. (2015). Facile synthesis of graphene oxide–silver nanocomposite and its modified electrode for enhanced electrochemical detection of nitrite ions. *Talanta, 144, 908-914.*

Jan, T., Iqbal, J., Ismail, M., Mansoor, Q., Mahmood, A., & Ahmad, A. (2014). Eradication of Multi-drug Resistant Bacteria by Ni Doped ZnO Nanorods: Structural, Raman and optical characteristics. *Applied Surface Science, 308(0), 75-81.*

Ji, T.-h., Sun, M., & Han, P. (2014). A review of the preparation and applications of graphene/semiconductor composites. *Carbon, 70, 319.*

Ji, Z., Shen, X., Yue, X., Zhou, H., Yang, J., Wang, Y., Chen, K. (2015). Facile synthesis of magnetically separable reduced graphene oxide/magnetite/silver nanocomposites with enhanced catalytic activity. *Journal of Colloid and Interface Science, 459, 79-85.*

Ji, Z., Shen, X., Zhou, H., & Chen, K. (2015). Facile synthesis of reduced graphene oxide/CeO2 nanocomposites and their application in supercapacitors. *Ceramics International, 41(7), 8710-8716.*

Kamat, P. V. (2009). Graphene-based nanoarchitectures. Anchoring semiconductor and metal nanoparticles on a two-dimensional carbon support. *The Journal of Physical Chemistry Letters, 1(2), 520-527.*

Kim, Y. J., Lee, M. H., Kim, H. J., Lim, G., Choi, Y. S., Park, N. G., Lee, W. I. (2009). Formation of Highly Efficient Dye Sensitized Solar Cells by Hierarchical Pore Generation with Nanoporous TiO2 Spheres. *Advanced Materials, 21(36), 3668-3673.*

Kongkanand, A., Dominguez, R. M., & Kamat, P. V. (2007). Single wall carbon nanotube scaffolds for photoelectrochemical solar cells. Capture and transport of photogenerated electrons. *Nano Letters, 7(3), 676-680.*

Lee, J. M., Pyun, Y. B., Yi, J., Choung, J. W., & Park, W. I. (2009). ZnO nanorod− graphene hybrid architectures for multifunctional conductors. *The Journal of Physical Chemistry C, 113(44), 19134-19138.*

Li, B., & Cao, H. (2011). ZnO@ graphene composite with enhanced performance for the removal of dye from water. *Journal of Materials Chemistry, 21(10), 3346-3349.*

Li, G. L., Liu, G., Li, M., Wan, D., Neoh, K., & Kang, E. (2010). Organo-and water-dispersible graphene oxide− polymer nanosheets for organic electronic memory and gold nanocomposites. *The Journal of Physical Chemistry C, 114(29), 12742-12748.*

Li, M., Yin, W., Han, X., & Chang, X. (2016). Hierarchical nanocomposites of polyaniline scales coated on graphene oxide sheets for enhanced supercapacitors. *Journal of Solid State Electrochemistry, 20(7), 1941-1948.*

Li, Q., & Hai, P. (2014). Rapid microwave-assisted synthesis of silver decorated-reduced graphene oxide nanoparticles with enhanced photocatalytic activity under visible light. *Materials Science in Semiconductor Processing, 22, 16-20.*

Li, Y., Cao, Y., Xie, J., Jia, D., Qin, H., & Liang, Z. (2015). Facile solid-state synthesis of Ag/graphene oxide nanocomposites as highly active and stable catalyst for the reduction of 4-nitrophenol. *Catalysis Communications, 58, 21-25.*

Li, Y., Wang, D., Li, W., & He, Y. (2015). Photoelectric conversion properties of electrochemically codeposited graphene oxide–ZnO nanocomposite films. *Journal of Alloys and Compounds, 648, 942-950.*

Liu, J., Liu, G., & Liu, W. (2014). Preparation of water-soluble β-cyclodextrin/poly(acrylic acid)/graphene oxide nanocomposites as new adsorbents to remove cationic dyes from aqueous solutions. *Chemical Engineering Journal, 257, 299-308.*

Liu, K., Zhang, J.-J., Cheng, F.-F., Zheng, T.-T., Wang, C., & Zhu, J.-J. (2011). Green and facile synthesis of highly biocompatible graphene nanosheets and its application for cellular imaging and drug delivery. *Journal of Materials Chemistry, 21(32), 12034.*

Liu, R., Li, N., Xia, G., Li, D., Wang, C., Xiao, N., Wu, G. (2013). Assembled hollow and core-shell SnO2 microspheres as anode materials for Li-ion batteries. *Materials Letters, 93, 243-246.*

Liu, X., Pan, L., Lv, T., Zhu, G., Sun, Z., & Sun, C. (2011). Microwave-assisted synthesis of CdS-reduced graphene oxide composites for photocatalytic reduction of Cr(VI). *Chemical Communications (Camb), 47(43), 11984-11986.*

Liu, X., Pan, L., Zhao, Q., Lv, T., Zhu, G., Chen, T., Sun, C. (2012). UV-assisted photocatalytic synthesis of ZnO–reduced graphene oxide composites with enhanced photocatalytic activity in reduction of Cr (VI). *Chemical Engineering Journal, 183, 238-243.*

Liu, Y., Liu, L., Shan, J., & Zhang, J. (2015). Electrodeposition of palladium and reduced graphene oxide nanocomposites on foam-nickel electrode for electrocatalytic hydrodechlorination of 4-chlorophenol. *Journal of hazardous materials, 290, 1-8.*

Lorestani, F., Shahnavaz, Z., Mn, P., Alias, Y., & Manan, N. S. A. (2015). One-step hydrothermal green synthesis of silver nanoparticle-carbon nanotube reduced-graphene oxide composite and its application as hydrogen peroxide sensor. *Sensors and Actuators B: Chemical, 208, 389-398.*

Lübke, M., Makwana, N. M., Gruar, R., Tighe, C., Brett, D., Shearing, P., Darr, J. A. (2015). High capacity nanocomposite Fe3O4/Fe anodes for Li-ion batteries. *Journal of Power Sources, 291, 102-107.*

Luo, L., Yang, Y., Zhang, A., Wang, M., Liu, Y., Bian, L., Pan, X. (2015). Hydrothermal synthesis of fluorinated anatase TiO2/reduced graphene oxide nanocomposites and their photocatalytic degradation of bisphenol A. *Applied Surface Science, 353, 469-479.*

Luo, Q.-P., Yu, X.-Y., Lei, B.-X., Chen, H.-Y., Kuang, D.-B., & Su, C.-Y. (2012). Reduced graphene oxide-hierarchical ZnO hollow sphere composites with enhanced photocurrent and photocatalytic activity. *The Journal of Physical Chemistry C, 116(14), 8111-8117.*

Lv, T., Pan, L., Liu, X., Lu, T., Zhu, G., & Sun, Z. (2011). Enhanced photocatalytic degradation of methylene blue by ZnO-reduced graphene oxide composite synthesized via microwave-assisted reaction. *Journal of Alloys and Compounds, 509(41), 10086-10091.*

Lv, T., Pan, L., Liu, X., & Sun, Z. (2012). Enhanced photocatalytic degradation of methylene blue by ZnO–reduced graphene oxide–carbon nanotube composites synthesized via microwave-assisted reaction. *Catalysis Science & Technology, 2(11), 2297. doi: 10.1039/c2cy20023f*

Marcano, D. C., Kosynkin, D. V., Berlin, J. M., Sinitskii, A., Sun, Z., Slesarev, A., Tour, J. M. (2010). Improved synthesis of graphene oxide. *ACS Nano, 4(8), 4806-4814.*

Maruthamani, D., Divakar, D., & Kumaravel, M. (2015). Enhanced photocatalytic activity of TiO2 by reduced graphene oxide in mineralization of Rhodamine B dye. *Journal of Industrial and Engineering Chemistry, 30, 33-43.*

Mehrali, M., Latibari, S. T., Mehrali, M., Metselaar, H. S. C., & Silakhori, M. (2013). Shape-stabilized phase change materials with high thermal conductivity based on paraffin/graphene oxide composite. *Energy Conversion and Management, 67, 275-282.*

Mkhoyan, K. A., Contryman, A. W., Silcox, J., Stewart, D. A., Eda, G., Mattevi, C., Chhowalla, M. (2009). Atomic and Electronic Structure of Graphene-Oxide. *Nano Letters, 9(3), 1058-1063.*

Muhammad Ekramul Mahmud, H. N., Huq, A. K. O., & Yahya, R. b. (2016). The removal of heavy metal ions from wastewater/aqueous solution using polypyrrole-based adsorbents: a review. *RSC Advances, 6(18), 14778-14791.*

Myung, S.-T., Kikuchi, M., Yoon, C. S., Yashiro, H., & Sun, Y.-K. (2015). A new synthetic method of titanium oxyfluoride and its application as an anode material for rechargeable lithium batteries. *Journal of Power Sources, 288, 376-383.*

Nurzulaikha, R., Lim, H. N., Harrison, I., Lim, S. S., Pandikumar, A., Huang, N. M., Ibrahim, I. (2015). Graphene/SnO2 nanocomposite-modified electrode for electrochemical detection of dopamine. *Sensing and Bio-Sensing Research, 5, 42-49.*

Ohsaki, Y., Masaki, N., Kitamura, T., Wada, Y., Okamoto, T., Sekino, T., Yanagida, S. (2005). Dye-sensitized TiO 2 nanotube solar cells: fabrication and electronic characterization. *Physical Chemistry Chemical Physics, 7(24), 4157-4163.*

Park, K. C., Ma, D. Y., & Kim, K. H. (1997). The physical properties of Al-doped zinc oxide films prepared by RF magnetron sputtering. *Thin Solid Films, 305(1), 201-209.*

Peng-Gang, R., Ding-Xiang, Y., Xu, J., Tao, C., & Zhong-Ming, L. (2011). Temperature dependence of graphene oxide reduced by hydrazine hydrate. *Nanotechnology, 22(5), 055705.*

Peng, H.-P., Hu, Y., Liu, P., Deng, Y.-N., Wang, P., Chen, W., Lin, X.-H. (2015). Label-free electrochemical DNA biosensor for rapid detection of mutidrug resistance gene based on Au nanoparticles/toluidine blue–graphene oxide nanocomposites. *Sensors and Actuators B: Chemical, 207, Part A, 269-276.*

Peng, X., Wang, L., Zhang, X., Gao, B., Fu, J., Xiao, S., Chu, P. K. (2015). Reduced graphene oxide encapsulated selenium nanoparticles for high-power lithium–selenium battery cathode. *Journal of Power Sources, 288, 214-220.*

Qi, K., Sun, Y., Duan, H., & Guo, X. (2015). A corrosion-protective coating based on a solution-processable polymer-grafted graphene oxide nanocomposite. *Corrosion Science, 98, 500-506.*

Qian, J., Yang, X., Jiang, L., Zhu, C., Mao, H., & Wang, K. (2014). Facile preparation of Fe3O4 nanospheres/reduced graphene oxide nanocomposites with high peroxidase-like activity for sensitive and selective colorimetric detection of acetylcholine. *Sensors and Actuators B: Chemical, 201, 160-166.*

Qiu, J., Zhang, P., Ling, M., Li, S., Liu, P., Zhao, H., & Zhang, S. (2012). Photocatalytic Synthesis of TiO2 and Reduced Graphene Oxide Nanocomposite for Lithium Ion Battery. *ACS Applied Materials & Interfaces, 4(7), 3636-3642.*

Qiu, X., Lu, L., Leng, J., Yu, Y., Wang, W., Jiang, M., & Bai, L. (2016). An enhanced electrochemical platform based on graphene oxide and multi-walled carbon nanotubes nanocomposite for sensitive determination of Sunset Yellow and Tartrazine. *Food Chemistry, 190, 889-895.*

Qu, J., Shi, L., He, C., Gao, F., Li, B., Zhou, Q., Qiu, J. (2014). Highly efficient synthesis of graphene/MnO< sub> 2</sub> hybrids and their application for ultrafast oxidative decomposition of methylene blue. *Carbon, 66, 485-492.*

Raghavan, N., Thangavel, S., & Venugopal, G. (2015). Enhanced photocatalytic degradation of methylene blue by reduced graphene-oxide/titanium dioxide/zinc oxide ternary nanocomposites. *Materials Science in Semiconductor Processing, 30, 321-329.*

Rai, A. K., Anh, L. T., Gim, J., Mathew, V., Kang, J., Paul, B. J., Kim, J. (2013). Simple synthesis and particle size effects of TiO2 nanoparticle anodes for rechargeable lithium ion batteries. *Electrochimica Acta, 90, 112-118.*

Ren, P. G., Yan, D. X., Ji, X., Chen, T., & Li, Z. M. (2011). Temperature dependence of graphene oxide reduced by hydrazine hydrate. *Nanotechnology, 22(5), 055705.*

Reza, K. K., Ali, M. A., Srivastava, S., Agrawal, V. V., & Biradar, A. M. (2015). Tyrosinase conjugated reduced graphene oxide based biointerface for bisphenol A sensor. *Biosensors and Bioelectronics, 74, 644-651.*

Robinson, J. T., Perkins, F. K., Snow, E. S., Wei, Z., & Sheehan, P. E. (2008). Reduced Graphene Oxide Molecular Sensors. *Nano Letters, 8(10), 3137-3140.*

Romero Aburto, R., Alemany, L. B., Weldeghiorghis, T. K., Ozden, S., Peng, Z., Lherbier, A., Ajayan, P. M. (2015). Chemical Makeup and Hydrophilic Behavior of Graphene Oxide Nanoribbons after Low-Temperature Fluorination. *ACS Nano, 9(7), 7009-7018.*

Saada, R., Kellici, S., Heil, T., Morgan, D., & Saha, B. (2015). Greener synthesis of dimethyl carbonate using a novel ceria–zirconia oxide/graphene nanocomposite catalyst. *Applied Catalysis B: Environmental, 168–169, 353-362.*

Sáaedi, A., Yousefi, R., Jamali-Sheini, F., Cheraghizade, M., Khorsand Zak, A., & Huang, N. M. (2013). Optical and electrical properties of p-type Li-doped ZnO nanowires. *Superlattices and Microstructures, 61, 91-96.*

Sadollahkhani, A., Kazeminezhad, I., Lu, J., Nur, O., Hultman, L., & Willander, M. (2014). Synthesis, structural characterization and photocatalytic application of ZnO@ZnS core-shell nanoparticles. *RSC Advances, 4(70), 36940-36950.*

Safa, S., Sarraf-Mamoory, R., & Azimirad, R. (2014). Investigation of reduced graphene oxide effects on ultra-violet detection of ZnO thin film. *Physica E: Low-Dimensional Systems and Nanostructures, 57, 155-160.*

Safavi, A., Tohidi, M., Mahyari, F. A., & Shahbaazi, H. (2012). One-pot synthesis of large scale graphene nanosheets from graphite-liquid crystal composite via thermal treatment. *Journal of Materials Chemistry, 22(9), 3825-3831.*

Setshedi, K. Z., Bhaumik, M., Onyango, M. S., & Maity, A. (2015). High-performance towards Cr(VI) removal using multi-active sites of polypyrrole–graphene oxide nanocomposites: Batch and column studies. *Chemical Engineering Journal, 262, 921-931.*

Shahil, K. M. F., & Balandin, A. A. (2012). Graphene–Multilayer Graphene Nanocomposites as Highly Efficient Thermal Interface Materials. *Nano Letters, 12(2), 861-867.*

She, X., Zhang, X., Liu, J., Li, L., Yu, X., Huang, Z., & Shang, S. (2015). Microwave-assisted synthesis of Mn3O4 nanoparticles@reduced graphene oxide nanocomposites for high performance supercapacitors. *Materials Research Bulletin, 70, 945-950.*

Shen, J. F., Yan, B., Shi, M., Ma, H. W., Li, N., & Ye, M. X. (2011). One step hydrothermal synthesis of TiO2-reduced graphene oxide sheets. *Journal of Materials Chemistry, 21(10), 3415-3421.*

Sheshmani, S., Akhundi Nematzadeh, M., Shokrollahzadeh, S., & Ashori, A. (2015). Preparation of graphene oxide/chitosan/FeOOH nanocomposite for the removal of Pb(II) from aqueous solution. *International Journal of Biological Macromolecules, 80, 475-480.*

Shi, P., & Ye, N. (2015). Investigation of the adsorption mechanism and preconcentration of sulfonamides using a porphyrin-functionalized Fe3O4-graphene oxide nanocomposite. *Talanta, 143, 219-225.*

Song, Y., Qu, K., Zhao, C., Ren, J., & Qu, X. (2010). Graphene Oxide: Intrinsic Peroxidase Catalytic Activity and Its Application to Glucose Detection. *Advanced Materials, 22(19), 2206-2210.*

Sookhakian, M., Amin, Y. M., & Basirun, W. J. (2013). Hierarchically ordered macro-mesoporous ZnS microsphere with reduced graphene oxide supporter for a highly efficient photodegradation of methylene blue. *Applied Surface Science, 283(0), 668-677.*

Sookhakian, M., Amin, Y. M., Zakaria, R., Baradaran, S., Mahmoudian, M. R., Rezayi, M., Basirun, W. J. (2014). Enhanced Photovoltaic Performance of Polymer Hybrid Nanostructure Heterojunction Solar Cells Based on Poly(3-hexylthiophene)/ZnS/ZnO/Reduced Graphene Oxide Shell–Core Nanorod Arrays. *Industrial & Engineering Chemistry Research, 53(37), 14301-14309.*

Sookhakian, M., Amin, Y. M., Zakaria, R., Basirun, W. J., Mahmoudian, M. R., Nasiri-Tabrizi, B., Azarang, M. (2015). Significantly improved photocurrent response of ZnS-reduced graphene oxide composites. *Journal of Alloys and Compounds, 632(0), 201-207.*

Stankovich, S., Dikin, D. A., Piner, R. D., Kohlhaas, K. A., Kleinhammes, A., Jia, Y. Ruoff, R. S. (2007). Synthesis of graphene-based nanosheets via chemical reduction of exfoliated graphite oxide. *Carbon, 45(7), 1558-1565.*

Su, P.-G., & Peng, S.-L. (2015). Fabrication and NO2 gas-sensing properties of reduced graphene oxide/WO3 nanocomposite films. *Talanta, 132, 398-405.*

Sun, H., She, P., Xu, K., Shang, Y., Yin, S., & Liu, Z. (2015). A self-standing nanocomposite foam of polyaniline@reduced graphene oxide for flexible super-capacitors. *Synthetic Metals, 209, 68-73.*

Sun, L., Wang, G., Hao, R., Han, D., & Cao, S. (2015). Solvothermal fabrication and enhanced visible light photocatalytic activity of Cu2O-reduced graphene oxide

composite microspheres for photodegradation of Rhodamine B. *Applied Surface Science, 358, Part A, 91-99.*

Tachikawa, T., Fujitsuka, M., & Majima, T. (2007). Mechanistic insight into the TiO2 photocatalytic reactions: design of new photocatalysts. *The Journal of Physical Chemistry C, 111(14), 5259-5275.*

Tan, J., Liu, L., Guo, S., Hu, H., Yan, Z., Zhou, Q., Wang, X. (2015). The electrochemical performance and mechanism of cobalt (II) fluoride as anode material for lithium and sodium ion batteries. *Electrochimica Acta, 168, 225-233.*

Tang, L., Nguyen, V. H., Lee, Y. R., Kim, J., & Shim, J.-J. (2015). Photocatalytic activity of reduced graphene oxide/SnO2 nanocomposites prepared in ionic liquid. *Synthetic Metals, 201, 54-60.*

Thakur, S., & Karak, N. (2015). Tuning of sunlight-induced self-cleaning and self-healing attributes of an elastomeric nanocomposite by judicious compositional variation of the TiO2-reduced graphene oxide nanohybrid. *Journal of Materials Chemistry A, 3(23), 12334-12342.*

Tian, J. Q., Liu, S., Li, H. Y., Wang, L., Zhang, Y. W., Luo, Y. L., Sun, X. P. (2012). One-step preparation of ZnO nanoparticle-decorated reduced graphene oxide composites and their application to photocurrent generation. *RSC Advances, 2(4), 1318-1321.*

Tiwari, D. C., Atri, P., & Sharma, R. (2015). Sensitive detection of ammonia by reduced graphene oxide/polypyrrole nanocomposites. *Synthetic Metals, 203, 228-234.*

Usachov, D., Vilkov, O., Grüneis, A., Haberer, D., Fedorov, A., Adamchuk, V. K., . . . Vyalikh, D. V. (2011). Nitrogen-Doped Graphene: Efficient Growth, Structure, and Electronic Properties. *Nano Letters, 11(12), 5401-5407.*

Vasilaki, E., Georgaki, I., Vernardou, D., Vamvakaki, M., & Katsarakis, N. (2015). Ag-loaded TiO2/reduced graphene oxide nanocomposites for enhanced visible-light photocatalytic activity. *Applied Surface Science, 353, 865-872.*

Vinodgopal, K., Neppolian, B., Lightcap, I. V., Grieser, F., Ashokkumar, M., & Kamat, P. V. (2010). Sonolytic design of graphene− Au nanocomposites. simultaneous and sequential reduction of graphene oxide and Au (III). *The Journal of Physical Chemistry Letters, 1(13), 1987-1993.*

Wang, H., Hao, Q., Yang, X., Lu, L., & Wang, X. (2009). Graphene oxide doped polyaniline for supercapacitors. *Electrochemistry Communications, 11(6), 1158-1161.*

Wang, H., Yuan, X., Wu, Y., Chen, X., Leng, L., Wang, H., Zeng, G. (2015). Facile synthesis of polypyrrole decorated reduced graphene oxide–Fe3O4 magnetic composites and its application for the Cr(VI) removal. *Chemical Engineering Journal, 262, 597-606.*

Wang, L., Wang, D., Dong, Z., Zhang, F., & Jin, J. (2013). Interface Chemistry Engineering for Stable Cycling of Reduced GO/SnO2 Nanocomposites for Lithium Ion Battery. *Nano Letters, 13(4), 1711-1716.*

Wang, T., Li, C., Ji, J., Wei, Y., Zhang, P., Wang, S., Gong, J. (2014). Reduced Graphene Oxide (rGO)/BiVO4 Composites with Maximized Interfacial Coupling for Visible Lght Photocatalysis. *ACS Sustainable Chemistry & Engineering, 2(10), 2253-2258.*

Wang, X., Yin, L., & Liu, G. (2014). Light irradiation-assisted synthesis of ZnO-CdS/reduced graphene oxide heterostructured sheets for efficient photocatalytic H2 evolution. *Chemical Communications, 50(26), 3460-3463.*

Wang, Y., Li, Z., Hu, D., Lin, C.-T., Li, J., & Lin, Y. (2010). Aptamer/Graphene Oxide Nanocomplex for in Situ Molecular Probing in Living Cells. *Journal of the American Chemical Society, 132(27), 9274-9276.*

Wang, Y., Shi, Z., Huang, Y., Ma, Y., Wang, C., Chen, M., & Chen, Y. (2009). Supercapacitor Devices Based on Graphene Materials. *The Journal of Physical Chemistry C, 113(30), 13103-13107.*

Weng, B., Yang, M. Q., Zhang, N., & Xu, Y. J. (2014). Toward the enhanced photoactivity and photostability of ZnO nanospheres via intimate surface coating with reduced graphene oxide. *Journal of Materials Chemistry A, 2(24), 9380-9389.*

Wengeler, L., Schmitt, M., Peters, K., Scharfer, P., & Schabel, W. (2013). Comparison of large scale coating techniques for organic and hybrid films in polymer based solar cells. *Chemical Engineering and Processing: Process Intensification, 68, 38-44.*

Wu, J., Shen, X., Jiang, L., Wang, K., & Chen, K. (2010). Solvothermal synthesis and characterization of sandwich-like graphene/ZnO nanocomposites. *Applied Surface Science, 256(9), 2826-2830.*

Wu, S., Han, T., Guo, J., & Cheng, Y. (2015). Poly(3-aminophenylboronic acid)-reduced graphene oxide nanocomposite modified electrode for ultrasensitive electrochemical detection of fluoride with a wide response range. *Sensors and Actuators B: Chemical, 220, 1305-1310.*

Xiang, Q., Yu, J., & Wong, P. K. (2011). Quantitative characterization of hydroxyl radicals produced by various photocatalysts. *Journal of Colloid and Interface Science, 357(1), 163-167.*

Xu, G., Jiang, F., Ren, Z.-a., & Yang, L.-w. (2015). Polyhedral MnO nanocrystals anchored on reduced graphene oxide as an anode material with superior lithium storage capability. *Ceramics International, 41(9, Part A), 10680-10688.*

Xu, T. G., Zhang, L. W., Cheng, H. Y., & Zhu, Y. F. (2011). Significantly enhanced photocatalytic performance of ZnO via graphene hybridization and the mechanism study. *Applied Catalysis B-Environmental, 101(3-4), 382-387.*

Xu, X., Shen, J., Li, N., & Ye, M. (2014). Facile synthesis of reduced graphene oxide/CoWO4 nanocomposites with enhanced electrochemical performances for supercapacitors. *Electrochimica Acta, 150, 23-34.*

Xu, Y.-T., Guo, Y., Jiang, H., Xie, X.-B., Zhao, B., Zhu, P.-L., Wong, C.-P. (2015). Enhanced Performance of Lithium-Ion Batteries with Copper Oxide Microspheres @ Graphene Oxide Micro/Nanocomposite Electrodes. *Energy Technology, 3(5), 488-495.*

Xue, Y., Chen, H., Yu, D., Wang, S., Yardeni, M., Dai, Q., Dai, L. (2011). Oxidizing metal ions with graphene oxide: the in situ formation of magnetic nanoparticles on self-reduced graphene sheets for multifunctional applications. *Chemical Communications (Camb), 47(42), 11689-11691.*

Yan, X., Zhang, X., Liu, H., Liu, Y., Ding, J., Liu, Y., Zhang, J. (2014). Fabrication of SDBS intercalated-reduced graphene oxide/polypyrrole nanocomposites for supercapacitors. *Synthetic Metals, 196, 1-7.*

Yan, Y., Zhang, X., Mao, H., Huang, Y., Ding, Q., & Pang, X. (2015). Hydroxyapatite/gelatin functionalized graphene oxide composite coatings deposited on TiO2 nanotube by electrochemical deposition for biomedical applications. *Applied Surface Science, 329, 76-82.*

Yang, H., Li, H., Zhai, J., Sun, L., & Yu, H. (2014). Simple Synthesis of Graphene Oxide Using Ultrasonic Cleaner from Expanded Graphite. *Industrial & Engineering Chemistry Research, 53(46), 17878-17883.*

Yang, P., Yan, H., Mao, S., Russo, R., Johnson, J., Saykally, R., Choi, H.-J. (2002). Controlled growth of ZnO nanowires and their optical properties. *Advanced Functional Materials, 12(5), 323.*

Yang, X., Zhang, X., Ma, Y., Huang, Y., Wang, Y., & Chen, Y. (2009). Superparamagnetic graphene oxide-Fe3O4nanoparticles hybrid for controlled targeted drug carriers. *Journal of Materials Chemistry, 19(18), 2710-2714.*

Yang, Y., Kang, M., Fang, S., Wang, M., He, L., Zhao, J., Zhang, Z. (2015). Electrochemical biosensor based on three-dimensional reduced graphene oxide and polyaniline nanocomposite for selective detection of mercury ions. *Sensors and Actuators B: Chemical, 214, 63-69.*

Yang, Y. J. (2015). One-pot synthesis of reduced graphene oxide/zinc sulfide nanocomposite at room temperature for simultaneous determination of ascorbic acid, dopamine and uric acid. *Sensors and Actuators B: Chemical, 221, 750-759.*

Yang, Z.-H., Zhuo, Y., Yuan, R., & Chai, Y.-Q. (2015). An amplified electrochemical immunosensor based on in situ-produced 1-naphthol as electroactive substance and graphene oxide and Pt nanoparticles functionalized CeO2 nanocomposites as signal enhancer. *Biosensors and Bioelectronics, 69, 321-327.*

Yao, Y., & Xue, Y. (2015). Impedance analysis of quartz crystal microbalance humidity sensors based on nanodiamond/graphene oxide nanocomposite film. *Sensors and Actuators B: Chemical, 211, 52-58.*

Yeh, C.-C., Wu, P.-R., & Chen, D.-H. (2014). Fabrication and near infrared photothermally-enhanced catalytic activity of Cu nanoparticles/reduced graphene oxide nanocomposite. *Materials Letters, 136, 274-277.*

Yola, M. L., Eren, T., & Atar, N. (2015). A sensitive molecular imprinted electrochemical sensor based on gold nanoparticles decorated graphene oxide: Application to selective determination of tyrosine in milk. *Sensors and Actuators B: Chemical, 210, 149-157.*

Yousefi, R., Jamali-Sheini, F., Cheraghizade, M., Khosravi-Gandomani, S., Sáaedi, A., Huang, N. M., Azarang, M. (2015). Enhanced visible-light photocatalytic activity of strontium-doped zinc oxide nanoparticles. *Materials Science in Semiconductor Processing, 32(0), 152-159.*

Yu, G., Hu, L., Liu, N., Wang, H., Vosgueritchian, M., Yang, Y., Bao, Z. (2011). Enhancing the Supercapacitor Performance of Graphene/MnO2 Nanostructured Electrodes by Conductive Wrapping. *Nano Letters, 11(10), 4438-4442.*

Yu, H., Yu, J., Cheng, B., & Zhou, M. (2006). Effects of hydrothermal post-treatment on microstructures and morphology of titanate nanoribbons. *Journal of Solid State Chemistry, 179(2), 349-354.*

Yu, J. C., Yu, J., Ho, W., Jiang, Z., & Zhang, L. (2002). Effects of F-doping on the photocatalytic activity and microstructures of nanocrystalline TiO2 powders. *Chemistry of Materials, 14(9), 3808-3816.*

Yun, H., Nguyen-Phan, T.-D., Pham, V. H., Kweon, H., Chung, J. S., Lee, B., & Shin, E. W. (2012). Influence of TiO2 dimension and graphene oxide content on the self-cleaning activity of methylene blue-stained photocatalytic films. *Materials Research Bulletin, 47(10), 2988-2993.*

Zahed, B., & Hosseini-Monfared, H. (2015). A comparative study of silver-graphene oxide nanocomposites as a recyclable catalyst for the aerobic oxidation of benzyl alcohol: Support effect. *Applied Surface Science, 328, 536-547.*

Zak, A. K., Abd Majid, W. H., Darroudi, M., & Yousefi, R. (2011). Synthesis and characterization of ZnO nanoparticles prepared in gelatin media. *Materials Letters, 65(1), 70-73.*

Zak, A. K., Razali, R., Majid, W. H., & Darroudi, M. (2011). Synthesis and characterization of a narrow size distribution of zinc oxide nanoparticles. *International Journal of Nanomedicine, 6, 1399-1403.*

Zhang, D., Tong, J., Xia, B., & Xue, Q. (2014). Ultrahigh performance humidity sensor based on layer-by-layer self-assembly of graphene oxide/polyelectrolyte nanocomposite film. *Sensors and Actuators B: Chemical, 203, 263-270.*

Zhang, J., Pan, J., Shao, L., Shu, J., Zhou, M., & Pan, J. (2014). Micro-sized cadmium tungstate as a high-performance anode material for lithium-ion batteries. *Journal of Alloys and Compounds, 614, 249-252.*

Zhang, J., Yu, J., Jaroniec, M., & Gong, J. R. (2012). Noble Metal-Free Reduced Graphene Oxide-Zn x Cd1–x S Nanocomposite with Enhanced Solar Photocatalytic H2-Production Performance. *Nano Letters, 12(9), 4584-4589.*

Zhang, L., Xia, J., Zhao, Q., Liu, L., & Zhang, Z. (2010). Functional Graphene Oxide as a Nanocarrier for Controlled Loading and Targeted Delivery of Mixed Anticancer Drugs. *Small, 6(4), 537-544.*

Zhang, Y., Chen, Z., Liu, S., & Xu, Y.-J. (2013). Size effect induced activity enhancement and anti-photocorrosion of reduced graphene oxide/ZnO composites for degradation of organic dyes and reduction of Cr(VI) in water. *Applied Catalysis B: Environmental, 140-141(0), 598-607.*

Zhang, Y., Zhang, N., Tang, Z.-R., & Xu, Y.-J. (2012). Graphene transforms wide band gap ZnS to a visible light photocatalyst. The new role of graphene as a macromolecular photosensitizer. *ACS Nano, 6(11), 9777-9789.*

Zheng, C., He, C., Zhang, H., Wang, W., & Lei, X. (2015). TiO2-reduced graphene oxide nanocomposite for high-rate application of lithium ion batteries. *Ionics, 21(1), 51-58.*

Zheng, C., Zheng, Y., Chen, W., & Wei, L. (2015). Encapsulation of graphene oxide/metal hybrids in nanostructured sol–gel silica ORMOSIL matrices and its applications in optical limiting. *Optics & Laser Technology, 68, 52-59.*

Zheng, W. T., Ho, Y. M., Tian, H. W., Wen, M., Qi, J. L., & Li, Y. A. (2009). Field emission from a composite of graphene sheets and ZnO nanowires. *The Journal of Physical Chemistry C, 113(21), 9164-9168.*

Zhou, Y., Bao, Q., Tang, L. A. L., Zhong, Y., & Loh, K. P. (2009). Hydrothermal Dehydration for the "Green" Reduction of Exfoliated Graphene Oxide to Graphene and Demonstration of Tunable Optical Limiting Properties. *Chemistry of Materials, 21(13), 2950-2956.*

Zhu, C., Guo, S., Fang, Y., & Dong, S. (2010). Reducing Sugar: New Functional Molecules for the Green Synthesis of Graphene Nanosheets. *ACS Nano, 4(4), 2429-2437.*

Zhu, Y., Murali, S., Stoller, M. D., Ganesh, K. J., Cai, W., Ferreira, P. J., Ruoff, R. S. (2011). Carbon-Based Supercapacitors Produced by Activation of Graphene. *Science, 332(6037), 1537-1541.*

Zou, W., Zhu, J., Sun, Y., & Wang, X. (2011). Depositing ZnO nanoparticles onto graphene in a polyol system. *Materials Chemistry and Physics, 125(3), 617-620.*

Zou, W. B., Zhu, J. W., Sun, Y. X., & Wang, X. (2011). Depositing ZnO nanoparticles onto graphene in a polyol system. *Materials Chemistry and Physics, 125(3), 617-620.*

LIST OF PUBLICATIONS AND PAPERS PRESENTED

1. Azarang, M., Shuhaimi, A., Yousefi, R., Moradi Golsheikh, A., & Sookhakian, M. (2014). Synthesis and characterization of ZnO NPs/reduced graphene oxide nanocomposite prepared in gelatin medium as highly efficient photo-degradation of MB. *Ceramics International, 40(7), 10217-10221.*

2. Azarang, M., Shuhaimi, A., Yousefi, R., & Sookhakian, M. (2014). Effects of graphene oxide concentration on optical properties of ZnO/RGO nanocomposites and their application to photocurrent generation. *Journal of Applied Physics, 116(8), 084307.*

3. Azarang, M., Shuhaimi, A., & Sookhakian, M. (2015). Crystalline quality assessment, photocurrent response and optical properties of reduced graphene oxide uniformly decorated zinc oxide nanoparticles based on the graphene oxide concentration. *RSC Advances., 5(65), 53117-53128.*

4. Azarang, M., Shuhaimi, A., Yousefi, R., & Jahromi, S. P. (2015). One-pot sol–gel synthesis of reduced graphene oxide uniformly decorated zinc oxide nanoparticles in starch environment for highly efficient photodegradation of Methylene Blue. *RSC Advances., 5(28), 21888-21896.*